EPFL

Parametric Wavelength Conversion in Waveguiding Structures: Efficiency, Bandwidth and Polarization

Arman AYAN

■ École
polytechnique
fédérale
de Lausanne

2024

To my beloved family. . .

Acknowledgements

Acknowledgements

Abstract

Photonics integrated circuits are a promising solution for the growing demands of data transmission and future system-on-chip technologies. Within this context, nonlinear optical interactions offer unique opportunities for all-optical signal processing, sampling, and sensing on-chip.

This thesis focused on the study of silicon nitride Si_3N_4 waveguides for nonlinear frequency conversion, specifically continuous-wave four-wave mixing (FWM), due to their ultra-low propagation loss, amenability to high-quality fabrication, broad transparency window, and ability to operate efficiently with watt-level pump powers. These features make them an attractive choice for on-chip FWM applications.

In addition to conversion efficiency (CE), the conversion bandwidth and spectral reach of FWM also play a crucial role in determining the limits of the applications. Therefore, this work focuses on efficient broadband on-chip wavelength conversion. The analysis starts with the polarization-selective dispersion engineering in Si_3N_4 waveguides enabling broadband wavelength conversion around 1.6 μm and 2.0 μm wavelength. Two-sided 3 dB conversion bandwidths of 160 nm and 120 nm are observed by leveraging polarization-dependent dispersion between TM to TE polarizations, respectively. The dispersion of the waveguides can be also utilized to satisfy the phase-matching at far-detuned wavelengths through higher-order dispersion terms. Such polarization-leveraged distant phase-matching has been observed in the waveguides reaching up to 2.6 μm wavelengths and 1.3 μm wavelengths utilizing common erbium and thulium-band.

Recent record high CW CE are obtained thanks to the use of low-loss long waveguides. However, increasing the effective length typically comes at the expense of bandwidth. Efficient-broadband conversion is investigated in various waveguides, which are engineered to maintain the broadest bandwidth at different lengths that can enhance the CE up to 2.9 dB. The obtained CE and bandwidth of the wavelength conversion schemes shown in this thesis are compared with state-of-the-art wavelength converters, proving their potential.

Yet, several challenges were observed during this analysis: strong dispersion sensitivity to the waveguide dimensions reduced CE due to higher-order mode excitation, and optical power fluctuations with mode-mixing. The origin of higher-order modes is identified as the transition

Abstract

---

of the different segments of the curvature. Temperature tuning is also analyzed to characterize and partially mitigate mode-mixing.

Finally, while polarization-sensitivity can be leveraged, it can also be a hurdle for applications requiring polarization-insensitivity. Polarization-insensitive wavelength conversion can be obtained by employing a depolarized pump at the cost of CE. The CE drop is analyzed on the depolarization scheme. The theoretical calculations are experimentally tested in chalcogenide photonic crystal fibers, selected due to their large nonlinearity.

In conclusion, Si_3N_4 waveguides show huge potential for on-chip optical processing and integrated photonics. While challenges persist, there is ample room for enhancing CE and bandwidth. While the unique polarization-selective nature can serve specific applications, depolarized FWM provides a pathway for on-chip PI parametric conversion.

Keywords: Nonlinear integrated optics, broadband conversion, parametric amplification, mode-mixing, depolarization

Résumé

Les circuits intégrés photoniques forment une solution prometteuse pour répondre aux exigences croissantes de la transmission de données et des futures technologies sur puce. Dans ce contexte, les effets optiques non linéaires offrent des opportunités uniques pour le traitement, l'échantillonnage et la détection tout-optique sur puce.

Cette thèse se concentre sur l'étude des guides d'onde en nitrure de silicium Si_3N_4 pour la conversion de fréquence non linéaire, en particulier le mélange à quatre ondes (MQO) en régime continu, du fait de leur faible perte de propagation, leur aptitude à une fabrication de haute qualité, leur large fenêtre de transparence et leur capacité à fonctionner avec des puissances de l'ordre du watt. Ces caractéristiques en font un choix intéressant pour les applications MQO sur puce.

Outre l'efficacité de conversion (EC), la largeur de bande de conversion et la portée spectrale du MQO jouent également un rôle crucial sur les limitations des applications. Ainsi ce travail se concentre sur la conversion efficace de longueur d'onde (LO) à large bande sur puce. L'analyse débute par l'ingénierie de la dispersion dans les guides Si_3N_4 permettant une conversion à large bande autour de 1.6 μm et 2.0 μm. Des largeurs de bande de conversion bilatérales de 3 dB de 160 nm et 120 nm sont observées en exploitant la dispersion des modes TM et TE, respectivement. La dispersion des guides peut également être utilisée pour satisfaire l'accord de phase à des longueurs d'onde éloignées grâce à des termes d'ordre supérieur. Un tel accord de phase fut observé jusqu'à 2.6 μm et 1.3 μm.

L'utilisation de longs guides à faible perte permet d'obtenir des niveaux records d'EC, mais l'augmentation de la longueur effective dégrade la bande passante. La conversion efficace à large bande est étudiée dans divers guides, conçus pour maintenir la largeur de bande pour différentes longueurs, et pouvant améliorer l'EC jusqu'à 2.9 dB. L'EC et la largeur de bande obtenus par les schémas de conversion présentés ici sont comparés aux convertisseurs les plus récents, prouvant leur potentiel.

Cependant, plusieurs défis furent rencontrés au cours de cette analyse : la forte sensibilité de la dispersion aux dimensions du guide d'onde, la réduction de l'EC due à l'excitation de modes d'ordre supérieur et des fluctuations de la puissance optique avec le mélange de modes. La cause de l'excitation des modes d'ordre supérieur est identifiée comme étant la

Résumé

transition des différents segments de la courbure. L'accord de température est aussi analysé pour caractériser et atténuer partiellement le mélange de modes.

Enfin, si la sensibilité à la polarisation peut être exploitée, elle peut également être un obstacle pour les applications requérant une insensibilité à la polarisation. La conversion insensible à la polarisation peut être obtenue en employant une pompe dépolarisée au prix de l'EC. La chute de l'EC est analysée en fonction du schéma de dépolarisation. Les calculs théoriques sont testés expérimentalement dans des fibres à cristaux photoniques de chalcogénure.

En conclusion, les guides Si_3N_4 présentent un énorme potentiel pour le traitement optique sur puce et la photonique intégrée. Les propriétés de polarisation du MQO permettent de satisfaire les besoins d'une application donnée.

Mots-clés : Optique intégrée non linéaire, conversion à large bande, amplification paramétrique, mélange de modes, dépolarisation.

Contents

Contents

Body 1 Part I

1 Introduction

1.1 All-optical processing and four-wave mixing applications

The ever-increasing demand for data transmission and processing has surged over the past decades. Progress in electronic technologies has managed to sustain this demand thanks to the miniaturization of electrical components, which has boosted processor speeds. However, the exponential growth projected by Moore's Law, where processing power is expected to double every two years [1], [2], is showing signs of slowing down. Advances in fabrication techniques have enabled the scaling down of components to the extraordinary scale of just a few nanometers [3], [4], and the adoption of multi-core processor architectures has met the demands of data processing and telecommunications thus far. Nevertheless, challenges persist, such as the deceleration of clock speed due to excessive heat dissipation [5]. Furthermore, electrical network-on-chip designs, which interconnect the various blocks, face limitations in scalability and bandwidth when dealing with architectures of 100 cores or more [6], [7]. One promising solution to address these limitations is the replacement of electrical network-on-chip systems with optical alternatives [8].

Long-range optical information transmission has been a widely recognized technique for decades. The emergence of optical communication led to high-speed global communication by offering a broad bandwidth and minimal electromagnetic interference during transmission. Efforts have been made to scale down part of the optical communication architectures to on-chip sizes, with significant advancements in photonic integrated circuits since 1984, when the first on-chip silicon photonics demonstration took place [9]. Modern on-chip optical networks are now capable of transmitting multiple terabits per second within a few millimeters, featuring over 10,000 links per chip and costing just a few cents per gigabit per second of data transmitted [10], [11]. Optical networks integrated at the motherboard level have also become commercially available [11] along with dual-core SiGe-based processors with fiberized optical interconnects [12]. However, the monolithic integration of optical and electrical components is required to achieve the desired performance and scalability and to unlock system-on-a-chip designs [13].

Chapter 1. Introduction

The monolithic integration of electrical and optical systems necessitates efficient and high-speed transitions between the electrical and optical domains. To achieve efficient monolithic integration, the medium should be capable of realizing the following functionalities: efficient coherent light generation, data encoding in the optical domain, and a high-speed low-noise transfer of the optical data to the electrical domain [14]. Advancements in silicon photonics have provided solutions to meet these requirements. Various CMOS-compatible photodetectors have been demonstrated [15] up to 100 GHz of bandwidth [16], [17] with dark currents densities which can get as low as 0.04 mA/cm^2 [18]–[20]. Additionally, different CMOS-compatible optical modulators have been implemented based on Mach-Zehnder interferometry [21], [22], quantum confined Stark effect [23], or Franz-Keldysh effect [24], [25] reaching 100 Gbps bit rates with optical losses in the order of few dBs. However, efficient light emission in Si-based platforms remains a challenge due to silicon's indirect bandgap semiconductor nature. Methods for on-chip light emission have been investigated [26]–[31] leading to the demonstration of lasing on Si [32]–[38]. Ongoing studies aim to realize monolithically integrated, room-temperature, low-threshold electrically-pumped lasers.

An alternative approach to address the challenges associated with the integration of optical and electrical systems is to transition towards an all-optical design that eliminates the need for a conversion between the two domains. This design requires the inclusion of optical interconnects, on-chip optical processing, and memory units, thus fundamentally transforming our understanding of digital architecture. Embracing an all-optical design brings numerous benefits, including the potential for higher data transfer speeds surpassing 1 Tb/s and reduced power consumption by eliminating inefficient electrical-optical domain interchange [39].

The development of all-optical memories poses challenges as the non-stationary nature of the photons hinders mimicking capacitor-like electronic memories for optical designs. Many alternative designs to provide optical memory functionality have been offered in the literature [40]. The volatile designs either in the form of static random access memory (RAM) [41], [42] or dynamic RAM[43], [44] as well as non-volatile memories exploiting phase-change materials [45], [46] have been implemented. Advancements in optical memories managed to reduce the footprints and access time to competitive levels. While achieving high-speed, low-power, and high-capacity scaling in optical memories remains a challenge, these optical memory solutions hold significant promise as potential alternatives for future technologies [40].

For an all-optical integrated computer system, the inclusion of an optical processing unit, along with interconnects and memory units, is essential. In addition, optical signal processing not only offers a processing data rate speed of more than 500 Gbps [39], but also implementation of quantum computing and optical neural networks [47], [48]. Considering that the discovery of nonlinear on-chip electronic elements enabled the implementation of boolean logic for processing, similar nonlinear interactions can be harnessed for optical on-chip processing. Moreover, compared to electronic signals, the ultra-fast angular carrier frequency of the optical signals also unveils enhanced interaction through wave interference.

With the advent of the laser, significant advancements have been made in the field of nonlinear optical interactions, stemming back to the early 1960s [49]. Over time, a multitude of nonlinear interactions have been explored, resulting in the development of several crucial functionalities necessary for optical processing. These functionalities include switching, routing, format conversion, phase conjugation, signal regeneration, optical Fourier transform, and phase-sensitive amplification [50]–[58]. Nonlinear optical interactions have served as the foundation for the demonstration of all fundamental optical gates, whether in semiconductor optical amplifiers or in nonlinear media. Currently, numerous studies are underway to achieve on-chip integration of these functionalities [59]–[64].

Although optical processing can function across a wide range of wavelengths, there are distinct advantages to operating within the telecommunication band, typically around 1550 nm wavelength. This choice aligns with the compatibility of fiber optical telecommunication systems and the ready availability of optical components and sources. Four-wave mixing (FWM) is a third-order nonlinear interaction that can provide wavelength conversion and parametric amplification. In addition, its group velocity mismatch independent conversion efficiency enables the broadband operation to cover the desired wavelength span in the telecommunication band.

FWM is a nonlinear interaction where two pump photons are converted to a signal and an idler photon. While this process can begin as a spontaneous interaction due to quantum effects [65], the classical model requires stimulation with a signal photon. A degenerate FWM process in a waveguide is illustrated along with an FWM energy diagram in Figure 1.1. The energy of two photons is transferred to the amplification of the signal photon and to the generation of the idler photon, enabling its application in parametric amplification and wavelength conversion.

The wavelength conversion capability of FWM extends beyond operating within the same wavelength ranges, known as spectral bands, as such photon-mixing processes are not limited to specific bands given a transparent nonlinear medium with an adequate dispersion landscape. As a result, FWM enables wavelength conversion to shorter wavelengths, encompassing the S-band, E-band, and O-band (up to a 1300 nm wavelength), as well as longer wavelengths within the extended L-band. Such broadband wavelength conversion via FWM opens up a larger communication window, which is increasingly important given the skyrocketing demand for data transfer. Moreover, distant phase-matching by dispersion engineering or by exploiting intermodal matching [66] allows the efficient generation of coherent sources in various spectra, including the visible, ultraviolet, and mid-infrared. Visible light generation from infrared sources has applications in infrared light sensing for security and defense [67] while ultraviolet light can be harnessed for photochemistry and photolithography [68]–[70]. Mid-infrared coherent source generation is particularly important for molecular sensing and spectroscopy. Molecular absorptions in the mid-infrared portion of the spectra are typically distinct, making it possible to detect individual molecules. Furthermore, the generated light can be used as a reference for quantum cascade lasers [71].

(a) **(b)** **(c)**
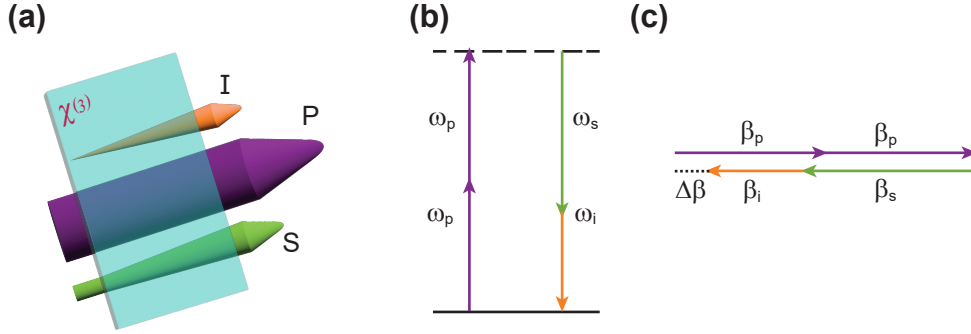
Figure 1.1: (a) Representation of stimulated degenerate four-wave-mixing in an nonlinear optical medium. P, depicted by the purple shape, represents the injected pump light to the nonlinear medium. S, depicted by the green shape, is the stimulating signal light whose intensity increases as a result of parametric amplification, which is depicted by the increase in the diameter of the shape. I, depicted by the orange shape, is the idler formed thanks to the nonlinear interaction in the nonlinear media. It should be noted that pump, signal, and idler actually overlap in the FWM process, which are drawn separately in the Figure to provide a better visuality. (b) Energy diagram of four-wave-mixing. ω_p, ω_s, and ω_i represent angular frequency of pump, signal, and idler, respectively. (c) Phase diagram of four-wave-mixing where $\Delta\beta$ represents phase mismatch and β_p, β_s, and β_i represent propagation constant of pump, signal, and idler, respectively.

In this thesis, I investigate the potential and limitations of FWM in integrated silicon nitride waveguides to realize such aforementioned applications on-chip. The thesis will focus specifically on improving the conversion efficiency and conversion bandwidth of dispersion-engineered waveguides as well as investigating higher-order dispersion phase-matching at distant wavelengths. Moreover, performance limitations encountered in such waveguides are studied, such as strong fluctuations in conversion efficiency. Their underlying causes are experimentally investigated and identified in order to provide possible routes to overcome and mitigate them. Lastly, depolarized FWM used to convert wavelength independent of signal state-of-polarization (SOP) is analyzed for applications that cannot control the signal SOP. A theory is developed and experimentally investigated, showing the conversion efficiency compromise caused by using a depolarized pump scheme as well as the comparison of different depolarization schemes.

1.2 Thesis organization

The remainder of this thesis is organized as follows:

In Chapter 2, the equations governing light confinement and excitation of optical modes are derived initially together with the definition of linear coefficients affecting FWM. Nonlinear propagation in a media will be derived as well as scalar FWM theory introducing the funda-

mental concepts such as conversion efficiency, phase-mismatch, and bandwidth. After that, a brief summary of vectorial FWM theory is presented showing the effect of SOPs on FWM conversion efficiency. The chapter finalizes with the literature review of FWM in various platforms and media showing the strengths and weaknesses of silicon nitride Si_3N_4 waveguides compared to others.

In Chapter 3, the dispersion engineering of Si_3N_4 waveguides to improve conversion bandwidth is investigated first through simulations and by experiments in meter-long waveguides fabricated by the Damascene process. The polarization-leveraged broadband operation around 2 µm in transverse electric (TE) polarization and 1.6 µm in transverse magnetic (TM) polarization is shown for specifically designed dimensions. The broadband operation in the telecommunication band in TE is also demonstrated for efficient broadband FWM. The efficiency bandwidth trade-off in the studied waveguides is also numerically and experimentally demonstrated together with the possibility to reach parametric gain. Lastly, higher-order dispersion distant phase-matching, i.e. the phase matching satisfied at a wavelength far detuned from the pump, is demonstrated for wavelength conversion to the mid-infrared in TE and to the O-band in TM, driven by standard erbium and thulium band sources.

In Chapter 4, the factors affecting conversion efficiency are theoretically analyzed and compared with the experimental results. The chapter continues with identifying the source of observed idler power fluctuations as mode-mixing and gives a model for the excitation of higher-order modes in the waveguides. The effect of the number of straight-to-bend transitions is investigated with another set of waveguides. The chapter is finalized with the effect of temperature on the mode-mixing and how it can be used to mitigate fluctuations.

Chapter 5 focuses on how polarization-insensitive four-wave-mixing can be obtained for applications where signal SOPs cannot be controlled. The chapter starts with the definition of the usage of depolarization together with a brief summary of common depolarization schemes, A theory is developed quantifying the conversion efficiency difference between different depolarization states as well as the compromise in the efficiency by utilizing a depolarized pump light. Two Chalcogenide photonic crystal fibers are selected to test the developed theory. The dispersion characteristics of the fibers are simulated and characterized with polarized FWM studies. In addition, broadband mid-infrared light generation via FWM in the chalcogenide fibers is tested by exploiting their zero-dispersion wavelength.

Chapter 6 summarizes the main results of the thesis and provides an outlook for the future of efficient broadband FWM in meter-long spiral waveguides. The strengths and limitations of four-wave-mixing in spiral silicon nitride waveguide are discussed together with possible dimensions and design engineering. The enhancement of nonlinearity through incorporating slightly higher silicon in silicon nitrides will be investigated via nonlinear parameter characterization and the discussion will be finalized with an outlook.

2 Theory

The optimization and exploitation of four-wave-mixing-based applications require a background not only in nonlinear propagation in a specific medium but also in linear propagation and optical confinement. In this chapter, the linear propagation in a confined medium will first be introduced together with the key linear parameters. The equations governing the four-wave mixing (FWM) efficiency and bandwidth will then be covered. Last, a literature review of on-chip FWM characterization with a comparison of platforms and dimensions is provided.

2.1 Optical confinement and linear propagation in the waveguides

The scientific interest in the field of optics has a centuries-old journey yet the soar of optical technologies has only been unlocked with the discovery of optical guiding. Optical guiding allows efficient propagation over long distances required for modern optical communication through the use of optical fibers, as well as miniaturization and integration of optical elements through integrated waveguides. Optical guiding has enabled numerous applications beyond telecommunications including enhanced sensing, beam shaping, optical signal processing, and nonlinear applications. In this subchapter, I introduce how the optical field is guided as well as how optical modes interact in a guided meduim. The derivations are simplified from various sources and the following references can be used for further reading[72], [73].

2.1.1 Optical guiding of electromagnetic waves

The confinement of the light in the transverse plane with respect to the propagation direction enables the transmission of light over long distances. The light guiding can be satisfied based on different phenomena such as photonic bandgap, anti-resonance, and total internal reflection. The photonic bandgap fibers, such as hollow core fibers, have a forbidden propagation in the transverse plane in the bandgap [74]. The anti-resonance waveguides are designed based on the destructive interference in the transverse plane. However, the more traditional method
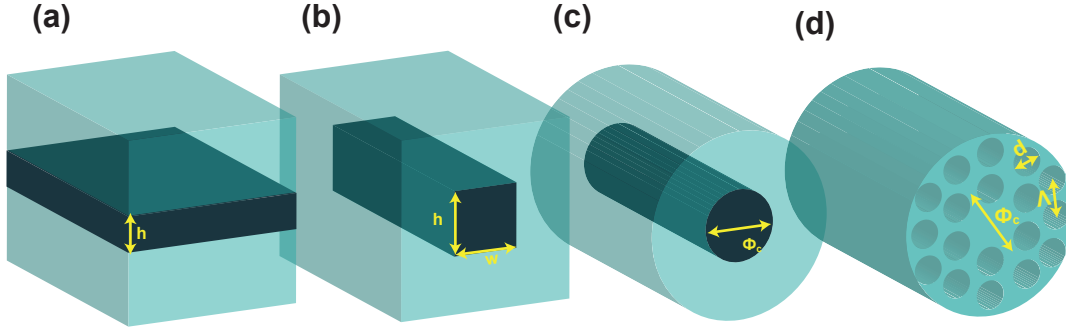
Figure 2.1: The depiction of (a) a slab waveguide (b) a rectangular waveguide (c) a step-index fiber (d) a photonic-crystal fiber. Light blue depicts the low refractive index medium called cladding whereas dark blue represents the high refractive index medium. The black circles represent holes forming the photonic crystals

of light guiding is obtained via total internal reflection that occurs at the transition from the high refractive index medium to the lower one[75]. Such guiding based on refractive index contrast is less sensitive to dimension fluctuations and allows operation in the broadband wavelength span. Therefore, most structures guiding the light, known as waveguides, operating in optical communication are based on the total internal refraction of the light. Hence, in this thesis, I will focus on such waveguide design.

The cross-section of waveguides typically has two regions. The region where the light is confined on the transverse plane is called the core, and the one surrounding the core is called cladding. In Figure 2.1, common waveguide schemes are depicted. The slab waveguides confine the light normal to the core-cladding interface, providing one-dimensional confinement. Two-dimensional confinement can be obtained in the rectangular waveguides where the light is confined along both principal axes of the transverse plane. The slab and rectangular waveguides are commonly used for on-chip applications due to their compatibility with common fabrication techniques. However, for long-distance optical communication, fiber technology provides optical transmittance at kilometers-long distances - that can go up to thousands of kilometers even - with low-cost production techniques. Fibers are a type of circular waveguides typically made out of glass or plastic, yet they are rather distinctively called fibers as they are significantly longer than they are wide. The step-index fibers are commonly doped at the core to create the refractive index contrast with the cladding. However, for certain materials, doping the core might be intricate. One method to satisfy the refractive index contrast is to reduce the effective refractive index of the cladding via air holes. The design of the air holes also allows fine-tuning of the fiber properties and structure is known as photonic crystal.

The confined light propagates through the waveguides with certain dimensions. The analytical solution is relatively simple for the slab waveguides where the light is confined to one axis, let

the axis be named y. From Maxwell's Equations, the wave equation can be obtained as

$$\nabla^2 \vec{E} - \frac{1}{c^2} \frac{\partial^2 \vec{E}}{\partial t^2} = \mu_0 \frac{\partial^2 \vec{P}}{\partial t^2} \tag{2.1}$$

where $\vec{E}$ is the electric field vector, $\vec{P}$ is the polarization vector, c is the speed of light in vacuum and μ_0 is the permeability of the vacuum. The assumption of linear response of the dipoles in a medium to the incident electric field leads to linearly scaling polarization vector to the incident electric field vector, i.e.

$$\vec{P} = \varepsilon_0 \chi^{(1)} \vec{E} \tag{2.2}$$

where $\chi^{(1)}$ is the linear susceptibility of the medium, also named first-order susceptibility, and ε_0 the permittivity of vacuum. For a monochromatic electric field having a single propagation constant and polarized along one axis, a scalar electric field can be written as

$$E = \frac{1}{2} B(z) \psi(x, y) e^{i\beta z - i\omega t} + c.c. \tag{2.3}$$

where B is the complex field changing along the propagation axis, ψ is the mode-shape function, β is the propagation constant, ω is the angular frequency and c.c. denotes the complex conjugate of the previous term. Assuming that the y derivative dominates over the x derivative due to the strong confinement of the slab waveguide in y-axis, the wave equation becomes

$$\left[-\frac{\partial^2}{\partial y^2} - \frac{\omega^2}{c^2} n^2(y) \right] \psi(y) = -\beta^2 \psi(y) \tag{2.4}$$

where n is the refractive index of the medium. Such differential equation yields decaying exponential for $\beta > \omega n/c$ and sinusoidal functions for $\beta < \omega n/c$. Then confinement is satisfied for $n_{core} > n_{eff} > n_{clad}$ where n_{core} is the core refractive index, n_{clad} is the cladding refractive index and the effective refractive index is defined as $n_{eff} = \beta c/\omega$. For a slab waveguide, the waveguide has a refractive index of n_{core} for the thickness h, as shown in Figure 2.1 and n_{clad} elsewhere. Then, the mode-shape function of the electric field would be

$$\begin{aligned}
\psi(y) &= C_1 e^{-\sigma(y-h/2)} & y &\geq h/2 \\
\psi(y) &= C_2 \cos(k_y y) + C_3 \sin(k_y y) & |y| &\leq h/2 \\
\psi(y) &= C_1 e^{\sigma(y+h/2)} & y &\leq -h/2
\end{aligned} \tag{2.5}$$

where $C_{1,2,3}$ are constants satisfying the boundary conditions depending on the polarization of the field, σ is the decay constant and k_y is the transverse wave vector amplitude, satisfying

$$\beta^2 + k_y^2 = \frac{\omega^2}{c^2} n_{core}^2, \quad \beta^2 - \sigma^2 = \frac{\omega^2}{c^2} n_{clad}^2 \tag{2.6}$$

Together with boundary conditions, only an integer number of k_x values can satisfy Equations (2.4) and (2.6), named modes. The number of modes depends on the dimensions of the

Figure 2.2: The depiction of the light coupling to the tapered via lensed fiber. The circular mode field diameter is approximately matched with the lensed fiber whereas the inverse tapers in the waveguides slightly expand the mode field in one axis for low-loss matching to the waveguide [76]

structure, refractive indices and operating frequency.

In rectangular waveguides and step-index fibers, the calculation of the field is more intricate. In fibers, utilizing the cylindrical symmetry of the system a solution in the form of Bessel functions can be obtained[73]. The depiction of LP_{01}, LP_{11}, LP_{02} and LP_{21} optical modes are shown in Figure 2.2 with possible mode degeneracy. However, in both structures, the fundamental mode is confined at the very center of the structure and decays as the field gets further from the center. Therefore, it is common to make a Gaussian approximation to the fundamental modes in both rectangular waveguides and step-index fibers.

The dimensions and refractive indices of the waveguides not only change the number of modes but also the propagation constant of the modes. In many applications, engineering of the group velocity $v_g = \beta_1^{-1} = (d\beta/d\omega)^{-1}$ and second-order dispersion, also called group velocity dispersion, $\beta_2 = (d^2\beta/d\omega^2)$, has an important role. The cladding material, structure or core dimensions can be engineered to fine-tune the dispersion characteristics of the waveguides. In fibers, on the other hand, such dispersion engineering is often satisfied by altering the doping profile or introducing photonic crystal structure into the cladding. The refractive index of the cladding is effectively tuned by adjusting the holes patterned in certain geometrical

shapes with their diameter (d) and pitch (Λ), which are shown in Figure 2.1. Engineering of chalcogenide glass photonic-crystal fibers (PCF) will be investigated in detail in Chapter 5.

2.1.2   Mode-overlap and mode-mixing

As explained in the previous subchapter, the waveguides can support a number of optical modes having their own mode-shape, n_{eff} and dispersion characteristics. Various applications can target different modes or their combination depending on the desired properties[77]. However, optical communication operating at multiple optical modes gives rise to modal dispersion limiting the communication speed of the system. Although various studies are working on overcoming the modal dispersion [78]–[80], data transfer with a single mode, which is the fundamental mode, is traditionally more common in optical communication. Similarly, the nonlinear applications benefit from increased photon-photon interaction as a result of higher confinement, which is typically obtained in the fundamental mode. Therefore, exciting the fundamental mode in the waveguide is desired for nonlinear applications.

Another important point is how modes evolve as they propagate through the waveguide. The solutions for the transverse component of the electric field found for waveguides and fibers form an orthonormal set, similar to the one found in Equation 2.5. Therefore, the modes normally do not interact with each other while propagating through the waveguide as they are orthogonal. However, scattering in a waveguide or transition to different media or dimensions can cause excitation of the higher-order modes. The scattering can be reduced by improving material quality and reducing defects. However, transitions between different sets of orthonormal modes require careful engineering for the control of light excited in each mode. The mode mismatch between standard 9 μm-diameter silica fibers and integrated sub-micron waveguides had also been a significant bottleneck for the progress of photonic integrated circuits.

The mismatch between two modes with the mode-shape function $\psi_k(x, y)$ and $\psi_l(x, y)$ can be calculated by the intensity mode-overlap integral (Γ).

$$\Gamma_{kl} = \frac{\left| \iint_S \psi_k(x, y) \cdot \psi_l^*(x, y) dx dy \right|^2}{\iint_S \left| \psi_k(x, y) \right|^2 dx dy \iint_S \left| \psi_l(x, y) \right|^2 dx dy} \tag{2.7}$$

where S represents the surface area where the light is confined. As the mode shapes and sizes get closer to each other, overlap integral approaches to 1. For $\Gamma < 1$, the remaining energy is coupled to the other modes and scatters at the transition. The strong scattering due to the transition between optical fibers and photonic integrated circuits has been overcome by engineering the fiber and/or the waveguide. Silica fibers tapered at the end, also called lensed fibers, can be used to couple the light into the waveguide. The taper serves as a lens and focuses the light into a small mode diameter at the focal length in order to match the mode sizes in the waveguides for an efficient coupling[81]. However, light can still excite
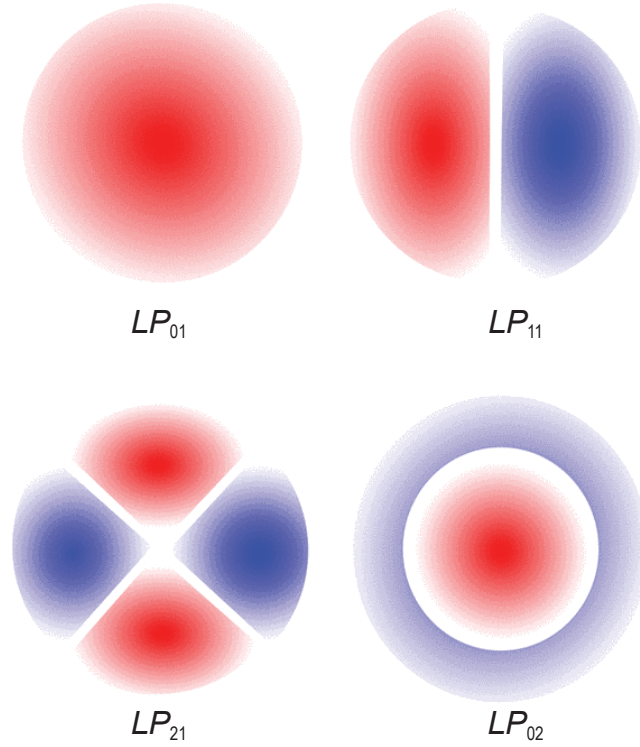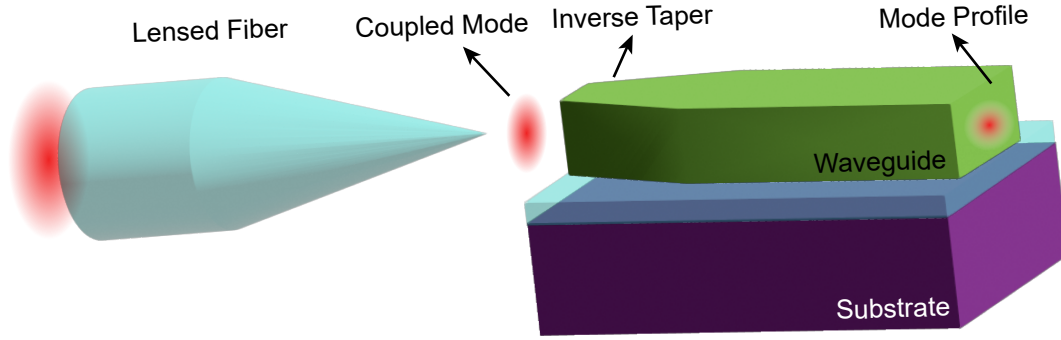
Figure 2.3: The depiction of the light coupling to the tapered via lensed fiber. The circular mode field diameter is approximately matched with the lensed fiber whereas the inverse tapers in the waveguides slightly expand the mode field in one axis for low-loss matching to the waveguide

higher-order modes of the waveguide or scatter. To avoid this, the waveguides are typically tapered to match the mode shape of the lensed fiber in order to overcome such an issue[82]. The state-of-the-art tapers can match the incident optical light to the waveguide mode with less than 1 dB optical loss [83], [84]. A depiction of coupling to the inverse tapers has been shown in Figure 2.3.

Although the transition from a single-mode waveguide to a multi-mode waveguide can be understood just by mode shapes, the transitions between two multi-mode waveguides require the phase of each mode as well. When more than one mode at the input side overlaps significantly with a mode at the output side, the light generated by each mode can interact constructively or destructively. Therefore, such interaction not only increases the coupling loss but also introduces phase sensitivity. The phase-sensitivity causes responsiveness to the optical power through nonlinear phase-modulation and temperature through the change in the effective refractive indices. Such an effect will be investigated in Chapter 4.

2.2   Nonlinear propagation and Four-wave-mixing

The optical response in a medium can be understood through the scattering response of the dipoles in the media [85]. Typically, the electric field of the dipole is much stronger than the incident electric field of the light at low incident optical powers causing a response that can be approximated by a linear perturbation of the dipole moment yielding a linear response. However, the response deviates from the linear regime to the nonlinear as the incident optical power becomes comparable with the electric field in the dipole and/or the incident electric field frequency approaches the resonance frequency. In this part, the nonlinear propagation and the origin of FWM will be derived, going through similar derivation steps as the following references[86]–[88].

2.2.1   Nonlinear Propagation

The origin of the nonlinear optical effects is the nonlinear response of the dipoles in the media to the incident field. Therefore, the polarization field formed by the dipole response no longer scales linearly with the incident electric field but it is a nonlinear function of it. We can write such polarization vector as a sum of the linear and nonlinear polarization vector. Therefore, the Equation 2.1 can be written as

$$\nabla^2 \vec{E} - \frac{1}{c^2} \frac{\partial^2 \vec{E}}{\partial t^2} = \mu_0 \frac{\partial^2 \left(\vec{P_l} + \vec{P_{nl}} \right)}{\partial t^2} \tag{2.8}$$

where $\vec{P_l}$ is the polarization vector same as Equation (2.2) and $\vec{P_{nl}}$ is the nonlinear polarization vector. Although wave equation could be quite intricate for a dominant nonlinear polarization vector, the linear response usually dominates for non-resonant electric fields. Therefore, the first three terms of the Taylor expansion are generally sufficient to include in the equations.

$$\vec{P} \approx \varepsilon_0 \left(\chi^{(1)} \vec{E} + \chi^{(2)} \vec{E}^2 + \chi^{(3)} \vec{E}^3 \right) \tag{2.9}$$

where the first term dominates the polarization vector and gives rise to linear effects in the waveguide. The second term introduces second-order nonlinearities such as second-harmonic generation, difference-frequency generation, or electro-optic effect. Although second-order nonlinearity for on-chip applications has been demonstrated in platforms that inherently embody non-zero $\chi^{(2)}$ such as thin film lithium niobate (TFLN)[89]–[91], silicon carbide (SiC)[92]–[94] and gallium nitride (GaN) [95], $\chi^{(2)}$ is inherently zero in centrosymmetric media including various common CMOS-compatible amorphous materials and single-element semiconductors used for optical applications such as silicon (Si), silicon nitride (Si_3N_4) and silicon dioxide (SiO_2).

The only active nonlinearity in the centrosymmetric platforms is the third-order nonlinearity which derives from the last term in the equation 2.9. In the most general form, $\chi^{(3)}$ is a tensor

containing 81 elements. However, in this section, we assume every electric field contributing to the nonlinear process is polarized along the same axis so that we can convert the $\chi^{(3)}$ tensor into a single scalar value. Then, to solve the equation 2.8 The electric field is written as the superposition of single-mode monochromatic fields in the form of:

$$E = \frac{1}{2} \sum_{k=1}^{m} B_k(z) \psi_k(x, y) e^{i\beta_k z - i\omega_k t} + c.c. \tag{2.10}$$

In the equation 2.10 we assumed the following: first, the electric field has a complex amplitude B changing along the propagation axis, z, which is not coupled to the mode shape function, $\psi(x, y)$. Although such an assumption does not take into account nonlinear changes in the mode, it is generally valid for continuous-wave (CW) signals as the change in the mode shape is usually small. Second, the propagation constant of each mode of monochromatic light stays constant over the waveguide length. As the nonlinear changes in the mode shape are neglected, the transverse derivatives in the ∇^2 are dropped in equation 2.8. Hence, the longitudinal wave equation becomes:

$$\left(\frac{d^2 B_k}{dz^2} - 2i\beta_k \frac{dB_k}{dz} - \beta_k^2 B_k + \frac{\omega^2}{c^2} B_k(z) \right) \psi_k(x, y) e^{i\beta_k z - i\omega_k t} + c.c. = -\frac{\omega^2 \chi^{(1)} E}{c^2} + \frac{1}{c^2} \frac{\partial^2 \chi^{(3)} E^3}{\partial t^2} \tag{2.11}$$

The next step is to apply the slowly varying envelope approximation where

$$\frac{d^2 B_k}{dz^2} << 2i\beta_k \frac{dB_k}{dz} \tag{2.12}$$

As $\left(1 + \chi^{(1)}\right) \frac{\omega^2}{c^2} = \beta_k^2$, the left-hand side in the Equation (2.11) drops to only the first derivative of complex amplitude function in z:

$$2i\beta_1 \frac{dB_1}{dz} \psi_k(x, y) e^{i\beta_k z - i\omega_k t} + c.c. = \frac{1}{c^2} \frac{\partial^2 \chi^{(3)} E^3}{\partial t^2} \tag{2.13}$$

On the right-hand side, the E^3 term causes the interaction of 3 different fields to affect the fourth one as long as the frequencies exactly match so that a time average would be nonzero. Therefore, as only 4 of the frequency components interact for a $\chi^{(3)}$ effect the m number in equation 2.10 will be set to 4. Such interaction gives rise to various nonlinear effects such as third-harmonic generation, self-phase modulation (SPM), cross-phase modulation (XPM), and FWM.

2.2.2 Scalar FWM Theory

Among all $\chi^{(3)}$ processes, the nonlinear interaction occurring at $\omega_1 = \omega_4 + \omega_3 - \omega_2$ is specifically important as it makes it possible to group velocity mismatch independent wavelength

conversion, parametric amplification and phase conjugation, unlocking numerous possible applications. Although such conversion is also referred to as four-wave difference-frequency mixing to differentiate from nonlinear mixing at $\omega_1 = \omega_4 + \omega_3 + \omega_2$ [96], it will be simply named as four-wave-mixing throughout this thesis.

In this part, among other $\chi^{(3)}$ effects, FWM equations will be investigated specifically at the frequency $\omega_1 = \omega_4 + \omega_3 - \omega_2$. Therefore, equation 2.13 becomes

$$-i\psi_1 \frac{dB_1}{dz} = \frac{3\chi^{(3)}\omega_1}{4cn_{\text{eff},1}} \psi_2^* \psi_3 \psi_4 B_2^* B_3 B_4 e^{i(\beta_3 + \beta_4 - \beta_1 - \beta_2)z} \tag{2.14}$$

In nonlinear applications, the efficiency of the process is generally understood by the coupled power to the waveguide. Therefore, it is common to utilize scaled mode field amplitudes such that

$$P_k = \frac{1}{2}c\varepsilon_0 n_{\text{eff,k}} B_k B_k^* \iint \psi_k \psi_k^* dx dy = A_k A_k^* \tag{2.15}$$

Therefore, equation 2.14 becomes

$$-i\frac{dA_1}{dz}\psi_1(x,y) = 2\gamma_{1234}A_2^* A_3 A_4 e^{i(\beta_3 + \beta_4 - \beta_1 - \beta_2)z} \tag{2.16}$$

where

$$\gamma_{1234} = \frac{3\mu_0\omega_1 \iint \chi^{(3)}(\omega_1,\omega_2,\omega_3,\omega_4)\psi_1^* \psi_2^* \psi_3 \psi_4 dx dy}{4\sqrt{n_{\text{eff},1}n_{\text{eff},2}n_{\text{eff},3}n_{\text{eff},4} \iint \psi_1^*\psi_1 dx dy \iint \psi_2^*\psi_2 dx dy \iint \psi_3^*\psi_3 dx dy \iint \psi_4^*\psi_4 dx dy}} \tag{2.17}$$

which is defined as the nonlinear parameter. A couple of assumptions will be made to simplify the nonlinear parameter. First, the $\chi^{(3)}$ will be assumed to be invariant of frequency and uniform throughout the waveguide. Second, the frequency detuning between the sources is small so that the mode profiles are essentially identical, denoted as ψ, for the same mode number. Last, the effective refractive indices are assumed to be close to each other. Then, the nonlinear parameter becomes

$$\gamma = \frac{3\mu_0\omega\chi^{(3)}}{4n_{\text{eff}}^2 A_{\text{eff}}} \tag{2.18}$$

where

$$A_{\text{eff}} = \frac{(\iint \psi^*\psi dx dy)^2}{\iint (\psi^*\psi)^2 dx dy} \tag{2.19}$$

The equation 2.16 is derived for a generalized case where any four waves interact at the frequency $\omega_1 = \omega_4 + \omega_3 - \omega_2$. However, in the most part of the thesis, stimulated one-pump configuration will be investigated (called degenerate FWM). Such configuration includes a pump having a dominantly high mode field amplitude A_p, with propagation constant β_p, at the angular frequency ω_p, an initially non-zero signal, A_s, with propagation constant β_s, at the angular frequency ω_S, and an idler, A_i, with propagation constant β_i, forming at $\omega_i = 2\omega_p - \omega_s$.

So far, only the FWM terms, i.e. the terms with $\chi^{(3)}(A_k A_k)A_{k'}^*$ factors, have been interested in the derivation of the set of differential equations. However, the existence of such high optical powers leads to other $\chi^{(3)}$ processes at the same time. Even though most of such processes yield a generation of light outside of the interested frequencies, that is pump, signal and idler frequencies, SPM and XPM would still affect the phase of the generated light. SPM modifies the phase of the light scaling with its amplitude $\Delta\beta_k z \propto \chi^{(3)}(A_k A_k^*)A_k$ whereas XPM is the interaction between two waves modifying the phase of each other, $\Delta\beta_k z \propto \chi^{(3)}(A_{k'}A_{k'}^*)A_k$ where $k' \neq k$. The derivation of SPM and XPM is omitted from this part for the sake of simplicity although the derivation would include similar steps. As pump power is assumed to be much larger than signal and idler power, $|A_p| >> |A_{s,i}|$, the only dominant effects in stimulated one-pump FWM process are SPM of the pump and XPM of the pump on the signal and idler. Then if the Equation (2.16) is rewritten for the pump, signal and idler, following equations are obtained:

$$\frac{dA_p}{dz} = i\gamma|A_p|^2 A_p + 2i\gamma A_p^* A_s A_i e^{i(\beta_s + \beta_i - 2\beta_p)z} \tag{2.20}$$

$$\frac{dA_s}{dz} = 2i\gamma|A_p|^2 A_s + i\gamma A_p^2 A_i^* e^{i(2\beta_p - \beta_s - \beta_i)z} \tag{2.21}$$

$$\frac{dA_i}{dz} = 2i\gamma|A_p|^2 A_i + i\gamma A_p^2 A_s^* e^{i(2\beta_p - \beta_s - \beta_i)z} \tag{2.22}$$

Although such a set of differential equations can be solved through the Jacobian elliptic functions [86], more straightforward solutions can be obtained under certain assumptions on the pump. To begin with, the depletion of the pump is neglected as pump power is much higher than the generated signal and idler. Therefore, the pump power is assumed to be constant throughout the propagation with a phase change of $\gamma P_p z$ induced by SPM. As a result, the coupled set of differential equations drops to two coupled equations coupling signal and idler which yields a second-order ordinary complex differential equation. Setting the initial phase of the pump to 0, such equations lead to a solution of idler and signal in the following form

$$A_s(z) = \left(\cosh(gz) + \frac{i\kappa}{2g}\sinh(gz)\right)e^{i(\gamma P_p - \frac{\kappa}{2})z}A_s(0) + \frac{i\gamma P_p}{g}\sinh(gz)e^{i(\gamma P_p - \frac{\kappa}{2})z}A_i^*(0) \tag{2.23}$$

$$A_i(z) = \left(\cosh(gz) + \frac{i\kappa}{2g}\sinh(gz)\right)e^{i(\gamma P_p - \frac{\kappa}{2})z}A_i(0) + \frac{i\gamma P_p}{g}\sinh(gz)e^{i(\gamma P_p - \frac{\kappa}{2})z}A_s^*(0) \tag{2.24}$$

where $\kappa = \beta_i + \beta_s - 2\beta_p + 2\gamma P_p$, $g^2 = (\gamma P_p)^2 - (\kappa/2)^2$ and P_p is the pump power. Thus, if the idler is initially zero, conversion efficiency, $CE = P_i(z)/P_s(0)$, and gain, $G = P_s(z)/P_s(0)$, are found as

$$CE = \left|\frac{\gamma P_p}{g}\sinh(gz)\right|^2 \tag{2.25}$$

$$G = 1 + \left| \frac{\gamma P_p}{g} \sinh(gz) \right|^2 \tag{2.26}$$

When gz multiplication is relatively high, the CE approximates to exponential growth with length if κ is relatively small, which is defined as phase-matched CE. As κ surpasses $2\gamma P_p$, g becomes imaginary causing sinusoidal fluctuations in the CE. Hence the CE becomes

$$CE \approx \left| \gamma P_p z \, \mathrm{sinc(gz)} \right|^2 \tag{2.27}$$

Similarly, in the low-CE regime, also called as low-gain regime, $\sinh(gz) \approx gz$ and therefore, phase-matched CE approximates to $CE_{pm} \approx (\gamma P_p z)^2$.

The inclusion of the propagation loss α in the differential equations is quite straightforward. The pump power is replaced by $P_p(0)e^{-\alpha z}$ and the phase mismatch κ has an extra $i\alpha/2$ term. However, the solution of the differential equation leads to a Bessel function with a complex order. Under low-gain approximation, a CE in the following form is obtained [97].

$$CE = \eta \gamma^2 P_p^2(0) L_{eff}^2, \tag{2.28}$$

$$\eta = \frac{\alpha^2}{\alpha^2 + \kappa^2} \left[1 + \frac{4\exp(-\alpha z)\sin^2(\kappa z/2)}{\left(1 - \exp(-\alpha z)\right)^2} \right]. \tag{2.29}$$

where $L_{eff} = \frac{1 - e^{-\alpha z}}{\alpha}$. The η function converges to a $\mathrm{sinc}^2(\kappa z/2)$ function as shown in Equation 2.27 under low-loss assumption.

2.2.3   Phase-matching and conversion bandwidth

As the idler is generated throughout the length of nonlinear media, the phase difference between the newly generated idler and the idler that was generated in the previous segments of the waveguide can interfere destructively, which can cause a drop in power. Ensuring the generated idler has the same phase as the previously generated idler is defined as phase-matching and holds a crucial role in numerous nonlinear interactions.

As the effect of phase difference at the output of a waveguide is investigated in this part, the position z will be replaced by L representing the total length of the waveguide. The phase-matching changes the low gain CE through the η function as Equation 2.28 implies. How the η function evolves with phase-mismatch, κL, is shown in Figure 2.4 for different αL terms. As the phase mismatch increases, the CE decreases until the first minimum and then oscillates in a decaying fashion. The amplitude of the oscillation decreases with increasing αL as the idler generated in the further portions of the waveguide cannot extinguish the previously generated idler field due to lower field amplitude. However, the phase mismatch at which the first minimum occurs does not change with the absorption. For a known length of the waveguide,
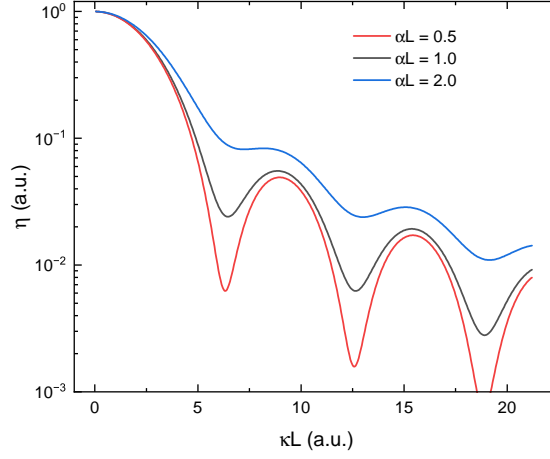
Figure 2.4: The η function vs phase-mismatch for various αL.

the location of the minima depends on the dispersion, the phase-matched CE depends on the pump power and the nonlinear parameter, and the contrast between the maxima and minima depends on the propagation loss provided that the waveguide is sufficiently uniform. Therefore, FWM experiments are widely used techniques to characterize the waveguides.

To understand how CE bandwidth depends on the dispersion characteristics of the waveguide and the signal and idler frequencies, the linear part of κ, denoted as $\Delta\beta_l$, will be investigated. The angular frequency of the idler will be defined as, $\omega_i = \omega_p + \Omega$, where Ω is the frequency detuning between the idler and the pump. Consequently, the angular frequency of the signal is $\omega_s = \omega_p - \Omega$. Therefore,

$$\Delta\beta_l = \beta_i + \beta_s - 2\beta_p = \beta(\omega_p + \Omega) + \beta(\omega_p - \Omega) - 2\beta(\omega_p) \tag{2.30}$$

If the propagation are expanded as a power series around ω_p, all odd terms cancel each other and only the terms with even derivatives remain. Therefore, the CE spectra will be symmetric with respect to the pump frequency.

$$\Delta\beta_l = \beta(\omega_p) + \beta(\omega_p) - 2\beta(\omega_p) + \beta_1(\Omega) - \beta_1(\Omega) + \frac{\beta_2}{2}\Omega^2 + \frac{\beta_2}{2}\Omega^2 + ... \tag{2.31}$$

For a small detuning, the terms with second-order derivative and fourth-order derivative are typically much larger than the other terms resulting in an approximate linear phase mismatch of

$$\Delta\beta_l L \approx \left(\beta_2\Omega^2 + \frac{\beta_4}{12}\Omega^4\right)L \tag{2.32}$$

The phase mismatch is zero at a zero frequency detuning and it increases gradually with frequency detuning in the vicinity of the pump. As the CE drops with increasing phase-mismatch there is a certain bandwidth over which we can obtain efficient wavelength conversion. There are various different definitions of bandwidth such as the difference between the frequencies where the efficiency drops to half, tenth or hundredth of the maximum efficiency defined as

3-dB bandwidth, 10-dB bandwidth and 20-dB bandwidth, respectively. For all definitions of bandwidth, the bandwidth scales with the phase-mismatch at which the first minima occur. Typically, $\beta_2 >> \beta_4 \Omega^2$; and hence, the first term dominates the phase-mismatch in Equation 2.32. Therefore, the bandwidth scales with

$$\Delta\Omega \propto \sqrt{\frac{4\pi}{|\beta_2|L}} \tag{2.33}$$

However, if the pump frequency is set to around ZDW, the fourth-order dispersion term dominates the bandwidth, and the bandwidth scales by

$$\Delta\Omega \propto 2\sqrt[4]{\frac{12\pi}{|\beta_4|L}} \tag{2.34}$$

which typically yields a much larger bandwidth than the case where the β_2 term dominates. Although the sign of dispersion does not affect the bandwidth according to Equations 2.33 and 2.34, a larger bandwidth can be obtained when β_2 and β_4 have opposite signs.

If the nonlinear phase mismatch is included in the calculations, i.e.

$$\kappa L \approx (\Delta\beta_l + 2\gamma P_p)L \tag{2.35}$$

the bandwidth can broaden or shrink depending on the sign of the linear mismatch. In anomalous dispersion region ($\beta_2 < 0$), the nonlinear phase mismatch, $\Delta\beta_{nl}$, reduces the linear phase mismatch resulting in a broader bandwidth for a small nonlinear phase mismatch contribution, i.e. $2\gamma PL << 2\pi$ as shown in Figure 2.5. However, as the nonlinear phase mismatch exceeds 2π, the phase matching cannot be satisfied around the pump and the conversion band shifts further from the pump frequency. According to the Equation (2.35), the angular frequency detuning at which frequency detuning, Ω_{pm}, occurs at

$$\Omega_{pm} = \sqrt{\frac{2\gamma P_p}{|\beta_2|}} \tag{2.36}$$

Under the large nonlinear phase-mismatch assumption the bandwidth is found to be proportional to

$$\Delta\Omega \approx \frac{\pi}{L}\sqrt{\frac{1}{2\gamma|\beta_2|P_p}} \tag{2.37}$$

Unlike the small nonlinear phase-mismatch case, increasing the pump power leads to a narrower bandwidth. On the other hand, the bandwidth shrinks with the nonlinear phase mismatch for normal dispersion ($\beta_2 > 0$). In this regime, for a large nonlinear phase mismatch, the efficient conversion band can vanish completely.
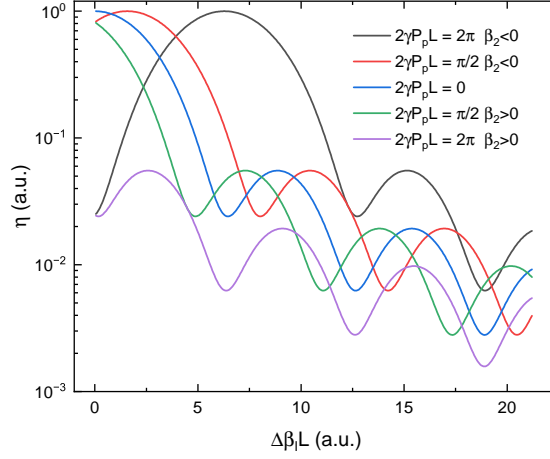
Figure 2.5: The η function vs linear phase-mismatch for various nonlinear phase-mismatch.

2.2.4 Vector FWM Theory in Isotropic Platforms

In the previous subchapter, FWM equations were derived for the scalar case where the effect of polarization was neglected. However, polarization plays a crucial role in most nonlinear interactions including FWM. Polarization refers to the orientation of the oscillations of electric and magnetic fields that make up the electromagnetic wave. Polarization is a fundamental property of light, which can lead to a change in not only the nonlinear interactions but also in waveguide and mode properties. The state of polarization (SOP) of the light can be linear, circular or elliptical. In the context of linear polarization, the electric field undergoes oscillations confined to a singular plane. This plane may either be oriented horizontally or vertically, or at varying angles encompassing the full range in between. The phase shift between the horizontal and vertical components of the light gives rise to an elliptically rotating electric field. The rotation becomes circular when the magnitude of the horizontal and vertical electric field components are equal and the phase shift between them is precisely $\pi/2$. The SOP is named right-hand circular polarization or left-hand circular polarization if the vertical component of the light is leading or lagging, respectively. The derivation in this subchapter is taken from the following reference [86].

To include the polarization effects, the nonlinear third-order polarization field is rewritten as

$$\vec{P_{nl}} = \varepsilon_0 \bar{\chi}^{(3)} : \vec{E}\vec{E}\vec{E} \tag{2.38}$$

where $\chi^{\bar{(3)}}$ is a tensor containing 81 elements and $\vec{P_{nl}}$ is the nonlinear third-order polarization vector. For various crystal structures, the symmetry conditions can be applied to simplify the equation and reduce the number of terms. As the materials of interest in this thesis are isotropic, the $\bar{\chi}^{(3)}$ tensor simplifies such that Equation 2.38 reduces to [98]

$$\vec{P_{nl}} = \varepsilon_0 \chi^{(3)} (\vec{E}.\vec{E})\vec{E} \tag{2.39}$$

where $\chi^{(3)}$ is a single effective scalar value. If the set of differential equations for the signal and idler are derived starting from Equation 2.38, similar to Equations 2.20, 2.21 and 2.22, it yields

$$\frac{d\vec{A}_p}{dz} = \frac{i}{3}\gamma[\vec{A}_p, \vec{A}_p^*, \vec{A}_p] \tag{2.40}$$

$$\frac{d\vec{A}_s}{dz} = \frac{2i}{3}\gamma[\vec{A}_p, \vec{A}_p^*, \vec{A}_s] + \frac{i}{3}\gamma[\vec{A}_p, \vec{A}_p, \vec{A}_i^*]e^{i(2\beta_p-\beta_s-\beta_i)z} \tag{2.41}$$

$$\frac{d\vec{A}_i}{dz} = \frac{2i}{3}\gamma[\vec{A}_p, \vec{A}_p^*, \vec{A}_i] + \frac{i}{3}\gamma[\vec{A}_p, \vec{A}_p, \vec{A}_s^*]e^{i(2\beta_p-\beta_s-\beta_i)z} \tag{2.42}$$

where

$$[\vec{A}_j, \vec{A}_k, \vec{A}_l] \triangleq (\vec{A}_j.\vec{A}_k)\vec{A}_l + (\vec{A}_k.\vec{A}_l)\vec{A}_j + (\vec{A}_l.\vec{A}_j)\vec{A}_k \tag{2.43}$$

If we use Jones vector notations where

$$\vec{A}_p = A_p \begin{bmatrix} a_{p,x} \\ a_{p,y} \end{bmatrix}, \vec{A}_s = A_s \begin{bmatrix} a_{s,x} \\ a_{s,y} \end{bmatrix}, \vec{A}_i = A_i \begin{bmatrix} a_{i,x} \\ a_{i,y} \end{bmatrix} \tag{2.44}$$

where all Jones elements are normalized and x components are set to real numbers.

$$[\vec{A}_p, \vec{A}_p, \vec{A}_s^*] = A_p^2 A_s((a_{p,x}a_{p,x} + a_{p,y}a_{p,y})\begin{bmatrix} a_{s,x} \\ a_{s,y}^* \end{bmatrix} + 2(a_{p,x}a_{s,x} + a_{p,y}a_{s,y}^*)\begin{bmatrix} a_{p,x} \\ a_{p,y} \end{bmatrix}) \tag{2.45}$$

Therefore, the ratio between the FWM coefficients of the scalar case and the vector case is defined by the b number

$$b = \frac{[\vec{A}_p, \vec{A}_p, \vec{A}_s^*]}{3A_p^2 A_s^*} = \frac{g_{max}}{3\gamma P_p} \tag{2.46}$$

where g_{max} is the maximum g value for given polarization states. and the ratio between the nonlinear phase mismatch of the scalar case and the vector case is defined by u number

$$u = \frac{2[\vec{A}_p, \vec{A}_p^*, \vec{A}_s]}{6|A_p|^2 A_s} + \frac{2[\vec{A}_p, \vec{A}_p^*, \vec{A}_i]}{6|A_p|^2 A_i} - 2\frac{[\vec{A}_p, \vec{A}_p^*, \vec{A}_p]}{6|A_p|^2 A_p} = \frac{\Delta\beta_{nl}}{2\gamma P_p} \tag{2.47}$$

Table 2.1: b and u numbers for given pump and signal/idler polarizations. X and Y denote the horizontal and vertical linear polarization. R and L denote right-hand and left-hand circular polarization respectively.

Pump polarization	Signal/idler polarization	$b = \frac{g_{max}}{\gamma P_p}$	$u = \frac{\Delta\beta_{nl}}{2\gamma P_p}$
X	X	1	1
X	Y	1/3	-1/3
R	R	2/3	2/3
R	L	0	2/3

To quantify the effect of the SOPs of the pump and the signal, four cases will be investigated: where the pump and signal have parallel linear polarization, perpendicular linear polarization, identical circular polarization and orthogonal circular polarization. For these cases, idler SOP is found to be identical to the signal SOP. The Jones vector representation of linearly polarized in the x-axis, in the y-axis, right-hand circularly polarized and left-hand circularly polarized are

$$J_x = \begin{bmatrix} 1 \\ 0 \end{bmatrix}, J_y = \begin{bmatrix} 0 \\ 1 \end{bmatrix}, J_{RCP} = \frac{1}{\sqrt{2}} \begin{bmatrix} 1 \\ -i \end{bmatrix} J_{LCP} = \frac{1}{\sqrt{2}} \begin{bmatrix} 1 \\ i \end{bmatrix} \tag{2.48}$$

respectively. The resulting b and u numbers calculated by the Equations 2.45, 2.46 and 2.47 are presented in Table 2.1. For parallel linear polarization, the same g_{max} and $\Delta\beta_{nl}$ are obtained as the scalar case. However, the g_{max} drops to 1/3 of the scalar case for perpendicular linear polarization. The nonlinear phase mismatch, on the other hand, changes the sign which enables phase-matching in all-normal dispersion platforms. For the circular polarization cases, the same nonlinear phase mismatch is obtained for both identical and orthogonal signal polarization, although no idler can be obtained for orthogonal circular signal and pump SOPs. Moreover, even if the signal and pump SOPs are identical, a lower CE is obtained for circularly polarized SOPs in comparison to linear polarization.

The SOP also has a significant impact on the effective refractive index of the medium. This is mainly due to factors such as the material's anisotropy, asymmetry of the waveguide along its principal axes, and external influences like variations in stress, pressure, and temperature. Consequently, the refractive index can vary depending on the SOP. Such variation in refractive index is known as birefringence. Birefringent medium causes a phase delay between the electric field components polarized along two principal axes. For an electric field having non-zero horizontal and vertical components, the light undergoes a constant change in the SOP. Therefore, it is common to align the SOP along the principal axes to maintain the SOP and maximize the CE for efficient wavelength conversion.

In integrated waveguides, the asymmetry in the height and width of the waveguide introduces significant birefringence and also impacts the mode shape and dispersion characteristics. As per convention, we classify modes as either quasi-transverse electric (referred to as TE) or quasi-transverse magnetic (referred to as TM), depending on whether most electric field or most magnetic field is polarized along the axis that is transverse to the propagation direction and the substrate surface normal, respectively. The change in the waveguide properties will later be investigated in detail in Chapter 3.

Certain applications may present limitations in controlling the input SOP, resulting in a dynamically changing polarization as the light travels through the birefringent medium. Moreover, the change in the birefringence axis can cause unpredictable variations in the state of polarization (SOP) of the transmitted light. To evaluate the impact of birefringence, we assume that the SOP becomes completely randomized during propagation, allowing it to cover all possible states on the Poincaré sphere. Additionally, we consider the frequency difference between the pump, signal, and idler to be negligible, ensuring that they all experience the same

Table 2.2: b and u number for totally randomized polarization due to birefringence

Pump and signal SOPs	$b = \frac{g_{max}}{\gamma P_p}$	$u = \frac{\Delta \beta_{nl}}{2\gamma P_p}$
Parallel	8/9	8/9
Orthogonal	2/9	0

polarization shift as they traverse the waveguide, with a constant angle difference between them. Lastly, the nonlinear polarization rotation effects are disregarded in our calculations assuming a small $\gamma P_p z$ factor.

To solve the Equations 2.46 and 2.47 for a randomized SOP, the pump, signal and idler are represented as the superposition of circularly polarized lights, whose Jones vectors are J_p, J_s and J_i, respectively. In the equations, the terms with $\vec{A}_k . \vec{A}_l^* / (A_k A_l^*)$ always yield 1 for identical SOPs and 0 for orthogonal SOPs. Therefore,

$$b = 2+ <J_p.J_p>, u = 2+ <J_p.J_p> +2+ <J_p.J_p> -2- <J_p.J_p> \tag{2.49}$$

for the identical pump, signal and idler SOPs, where <> represents the average over Poincaré sphere, and

$$b = <J_p.J_p>, u = 1+ <J_p.J_s> +1+ <J_p.J_s> -2- <J_p.J_p> \tag{2.50}$$

for the identical signal and idler SOPs but orthogonal pump SOP.

The calculation steps of the $<J_p.J_p>$ and $<J_p.J_s>$ terms for identical and orthogonal SOPs can be found in [86] and omitted here for the sake of simplicity. The $<J_p.J_p>$ term yields 2/3 and $<J_p.J_s>$ term yields 1/3 for orthogonal pump and signal SOPs. The b and u numbers calculated for random birefringence are tabulated in Table 2.2. The birefringence is an important aspect of a waveguide that can reduce efficiency and that can cancel the effect of nonlinear phase shifts.

2.3 Materials and Platforms

Depending on the intended applications of FWM, certain constraints are introduced to the overall system. Specific applications might require high CE (or parametric gain on the signal), need to be compatible with low pump powers, or demand for ultra-broad operation, for example. A lot of work has been already done in optical fibers such as highly nonlinear fibers (HNLFs), with great success. Fiber optical parametric amplifiers (FOPA) have indeed been widely studied for communication applications and are able to provide high phase sensitive and phases-insensitive gains. Chalcogenide fibers have also been investigated for mid-IR operation. On the other hand, there is a strong push for the integration of nonlinear functionalities, including FWM and parametric amplification. Integration also offers the possibility to exploit a wide range of optical materials beyond standard silica, that can open

less conventional spectral ranges beyond the telecom band. Thus overall numerous platforms and diverse materials have been and are still being investigated for FWM.

The most common platforms to study FWM are fibers, integrated waveguides and microresonators. The maturity of standard silica fiber technologies allows for km-long fibers with dB/km level of optical losses. It is possible to expand the geometrical space, and hence dispersion engineering capabilities by leveraging the photonic crystal technology. Specifically, chalcogenide glass photonic crystal fibers provide strong nonlinearity and dispersion engineer capability enabling nonlinear operation in the mid-infrared which will be covered in Chapter 5.

In the past, various studies have demonstrated methods to enhance parametric gain, engineer dispersion, or exploit intermodal phase-matching in fibers [99]–[108]. However, miniaturizing the dimensions requires on-chip solutions such as integrated waveguides or microresonators. Microresonators are particularly interested in nonlinear interactions thanks to the strong field enhancement effect as well as temporal confinement. Microresonators are routinely used for the generation of frequency combs covering more than an octave [109]–[113]. FWM has also been investigated in microresonators but the operation is limited to discrete transmission frequencies separated by their free spectral range and thermal effects can complicate the control and scaling of the desired conversion. Nevertheless, several demonstrations have shown high efficiency wavelength conversions [114]–[116].

Waveguides have the potential to provide broad bandwidth and high efficiency in an integrated platform, granted that the platforms offer sufficiently low loss and can provide a high $\gamma P L_{\text{eff}}$ product. The maturity of silica technology in the photonics field and its CMOS fabrication quality leads SiO_2 to stand out among other candidate materials in terms of loss. Although SiO_2 fibers provide very low nonlinearity $\gamma \approx 0.001 \text{W}^{-1}\text{m}^{-1}$, the efforts of increasing the nonlinearity blossomed through the development of high index contrast silica glass waveguides, also called Hydex glass waveguides [117]. The Hydex glass provides nonlinear parameters up to $\gamma \approx 0.2 \text{W}^{-1}\text{m}^{-1}$ while still offering a few dB/m loss [118]–[121]. In addition, the dispersion can be further engineered at 1550 nm wavelength with $\beta_2 < 10\text{ps}^2/\text{km}$ [122]. Although there have been further efforts to increase the nonlinearity with silica nanowires up to $\gamma \approx 0.6 \text{W}^{-1}\text{m}^{-1}$ [123], the higher optical propagation loss prevented achieving long effective lengths. The relatively low nonlinearity limited the use of silica-based waveguides for nonlinear applications requiring high efficiency.

In the last decades, silicon (Si) photonics has emerged as a promising field due to its compatibility with existing electronics technology. Furthermore, silicon offers greater nonlinearity compared to silica or hydex, making it a captivating option for efficient FWM. Additionally, the high refractive index contrast between silicon (n = 3.47) and silica (n = 1.47) at 1550 nm wavelength enables Si waveguides to provide strong confinement, thereby enhancing efficiency by confining light within nanometer-scale structures. The nonlinear parameter measured in Si is approximately $\gamma \approx 200 \text{W}^{-1}\text{m}^{-1}$ [124] for standard waveguide width and height of 0.5 μm ×

0.3 μm. The dispersion of the waveguide can be also engineered by tuning the dimensions and the shape of the waveguide so that inherently high material dispersion of Si in the optical communication band can be overcome [125]–[127]. However, the bandgap of Si is around 1.1 eV and therefore exhibits two-photon absorption (TPA) around 1550 nm, limiting the amount of pump power that can be coupled to the devices and hence the achievable FWM CE. Although the engineering of the waveguide structure and implementation of reverse biased p-i-n structure managed to further increase the CE [128], [129], reaching positive CEs in dB scale in CW regime in Si remained a challenge.

Other Si-compatible platforms have been investigated as well. SiGe-based waveguides provide parameter tunability with Ge concentration while providing similar CEs [130], [131]. Amorphous Si-based waveguides offer low-temperature epitaxy-free fabrication without wafer-bonding providing a monolithic integration possibility at the backend of a standard CMOS fabrication [132]. However, both Si-Ge and amorphous-Si still suffer from TPA. SiC has also been investigated with the aim of suppressing TPA thanks to its larger bandgap and wider transparency window extending down to the visible range. Although the nonlinear parameter can reach up to $\gamma \approx 40\,W^{-1}m^{-1}$, the propagation loss is still high ($\approx 300\,\text{dB/m}$) and SiC waveguides still experience three-photon absorption [133]–[135].

To circumvent the need for high power or long length, materials that provide strong nonlinearity are also studied for FWM applications. Chalcogenide glass (ChG) is one such material formed by a certain compound of Ge, As, In and Sb together with a cation of group VI element such as S, Se and Te, providing parameter tunability with the relative concentrations. The bandgap of ChG can be increased to 2 eV significantly reducing TPA Nonlinear experiments in ChG waveguides yielded tunable nonlinear parameters from $1.7\,W^{-1}m^{-1}$ to $136\,W^{-1}m^{-1}$ with a propagation loss in the range of $5\,\text{dB/m}$ and $80\,\text{dB/m}$ [136]–[140]. Nevertheless, the photodarkening of the waveguides and low threshold photocrystallisation limit the use of ChG waveguides for nonlinear applications [141], [142]. Furthermore, the high material dispersion of ChG in the short-wave infrared spectrum presents a challenge for achieving broadband wavelength conversion, despite its promising potential for mid-infrared applications [143], [144].

III-V compound semiconductors provide a well-known tunability of the bandgap with the ratio of elements [145], [146]. The trade-off between the nonlinearity, which scales with the fourth power of inverse bandgap, E_g^{-4}, [147] and TPA, which increases with decreasing bandgap, can be fined tuned with the compound percentage. Thanks to such capability and mature fabrication, AlGaAs semiconductor waveguides yielded nonlinear parameters around $\gamma \approx 500\,W^{-1}m^{-1}$ [148]–[151], which can even go up to $\gamma \approx 2900\,W^{-1}m^{-1}$ [152]. However, linear losses in the order of $1000\,\text{dB/m}$ hindered obtaining highly efficient on-chip FWM [152], [153]. Recent works managed to reduce the linear optical loss lower than $100\,\text{dB/m}$ while maintaining a strong nonlinearity and managed to achieve CW CE up to -4 dB [154], [155]. In addition, by engineering the dispersion with dimensions, a two-sided bandwidth as large as 720 nm has been obtained. Although InGaAs-based or AlGaAs-based waveguides provide

stronger nonlinearity, there are still efforts to reduce the propagation loss by utilizing AlN or GaN with a compromise on nonlinearity [113], [156].

Silicon nitride has attracted attention from the beginning of the search for a nonlinear platform thanks to its CMOS fabrication compatibility, wide bandgap and higher nonlinear coefficient than silica. However, the stress building up in more than 250 nm-thick waveguides significantly increased the propagation loss [157]–[160]. Such propagation losses and their moderate nonlinearity, $\gamma \approx 1\,\mathrm{W}^{-1}\mathrm{m}^{-1}$ [161], hindered high CE in stoichiometric silicon nitride (Si_3N_4) waveguides. Various efforts to reduce the propagation losses below $100\,\mathrm{dB/m}$ have been proven to be fruitful reaching conversion efficiencies up to -26 dB [162], [163]. Other efforts focused on enhancing the nonlinearity through utilizing silicon-rich silicon nitride at the expense of higher propagation loss [164]–[172]. Conversion efficiencies up to -25 dB have been obtained in 7 mm long waveguides in silicon-rich silicon nitride waveguides despite the high propagation loss [173].

Recent developments in the fabrication of stoichiometric Si_3N_4 waveguides and microresonators managed to reduce the propagation loss gradually below 1 dB/m, tremendously increasing the potential of efficiency in the stoichiometric Si_3N_4 waveguide [174]–[185]. Moreover, advanced subtractive process [186], [187] and Damascene process [188] managed to keep the loss around few dB/m range in the waveguides longer than a meter. Thanks to these advances, Ye et al. managed to reach the CW phase-sensitive gain of 9.5 dB in a 1.42-meter long waveguide at 2.8 W of pump power and phase-insensitive CE of 5.3 dB [189] and Riemensberger et al. managed to obtain phase-insensitive CE over 9 dB in a 2-meter long waveguide at 6 W of pump power [190]. The theoretical limit of propagation loss in stoichiometric Si_3N_4 is around 0.2 dB/m [188] and even higher efficiencies can be obtained theoretically by increasing the length [191].

The inversion symmetry of Si and Si_3N_4 based waveguides prevented obtaining on-chip $\chi^{(2)}$ processes in the past whereas compound III-V and II-VI semiconductors manage to host various $\chi^{(2)}$ processes as an efficient platform [192]–[194]. However, the photoinduced techniques and quasi-phase matching grating inscriptions through optical poling nominated Si_3N_4 as a competitive candidate and various $\chi^{(2)}$ effects are also demonstrated in Si_3N_4 such as second-harmonic generation [195]–[198], sum-frequency generation [199], difference frequency generation [200] and spontaneous parametric-down conversion [201].

2.4   Silicon Nitride Waveguide Engineering

In optical waveguides, dispersion is a critical factor that can affect the integrity of optical signals. Dispersion occurs due to the wavelength-dependent effective index and can lead to different wavelengths of light traveling at varying speeds, causing pulsed signal spreading. The origin of the dispersion may arise from material dispersion or waveguide dispersion. The material dispersion originates from the change in the refractive index with the wavelength as a result of the dipole response. The waveguide dispersion, on the other hand, results from
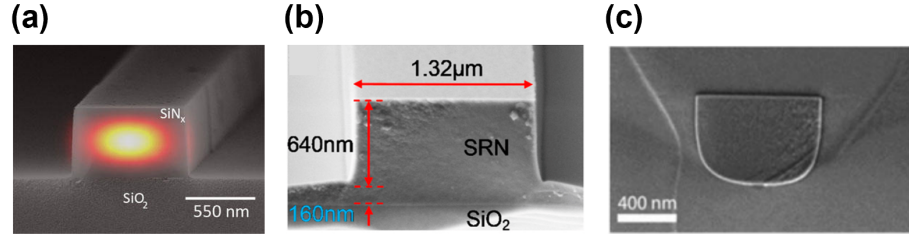
Figure 2.6: The cross-section scanning electron micrograph of silicon nitride (a) ridge waveguides[202] (b) rib waveguide[203] (c) buried channel waveguide[204].

variations in the effective refractive index for different guided modes within the waveguide. Therefore, waveguide dispersion depends on the waveguide's geometric and refractive index properties. To mitigate the effects of dispersion in waveguides, waveguide dispersion can be adjusted to counteract material dispersion. In addition to these intramodal effects, different optical modes and polarizations yield distinct dispersion characteristics, known as modal dispersion and polarization dispersion, respectively. By harnessing them, the material dispersion can be compensated as well or the compensated dispersion can be extended to cover various wavelength spans. Engineering material and waveguide dispersion is critical for optimizing the performance of optical waveguide-based networks and enabling broadband nonlinear applications.

The selection of waveguide type is a critical factor in determining waveguide parameters. In Figure 2.6, scanning electron micrographs illustrate various waveguide types, including ridge waveguide [202], rib waveguide [203], and buried channel waveguide [204], made of silicon nitride. Both channel waveguides and rib waveguides offer convenient fabrication processes and the possibility of being coated with 2-D layers such as WS_2 [205], graphene [206], and graphene oxide [207], which can potentially enhance the nonlinearity of the waveguide. However, rib waveguides, while providing greater design flexibility due to having more dimension parameters, can suffer from scattering loss due to the rib edge [208]. On the other hand, buried channel waveguides require a more intricate fabrication process to ensure coating conformity, high-quality core-cladding interfaces, and minimal stress-related defects in the material. Nonetheless, these waveguides have advantages such as lower surface scattering and a more symmetrical mode, resulting in reduced optical loss and improved coupling efficiency [209].

The recent advancements in fabrication processes for silicon nitride buried waveguides have successfully addressed the challenges associated with low-loss waveguides. One particularly effective fabrication process is the Damascene process, which is known for producing high-quality silicon nitride waveguides (see Figure 2.7). Through the optimization of annealing
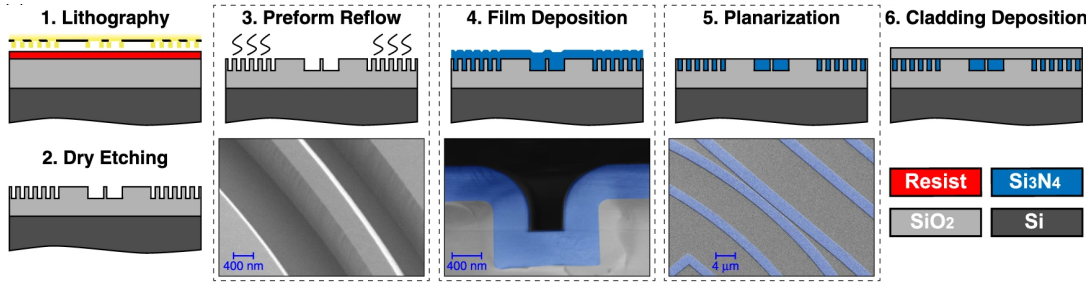
Figure 2.7: The fabrication steps of Damascene process depicting the conformity of the of the deposition and stress removal structures [188].

and planarization processes, the surface roughness of silica and silicon nitride layers has been improved, resulting in enhanced interface quality [210]. Additionally, the use of optimal dry-etching techniques on the substrate has minimized underetching and ensured better verticality, leading to improved layer conformity. However, achieving low-defect silicon nitride growth necessitates low-pressure chemical vapor deposition, which typically requires high operating temperatures. The disparate thermal expansion coefficients of silicon nitride and silica can introduce significant stress, potentially causing stress cracks in thicker waveguides. Furthermore, smaller waveguide cross-sections contribute to increased bending loss, thereby limiting the fabrication of longer spirals. To address these issues, stress-removal layers have been incorporated into the waveguide design, resulting in a significant reduction in stress cracks. Consequently, the optical propagation loss has been successfully reduced to below 4 dB/m [188].

Exploring longer effective lengths in integrated Si_3N_4 waveguides has emerged as a potential solution to address its moderate nonlinearity. Nevertheless, the extension of these waveguides to meter-scale lengths presents us with a significant challenge. To fit them into a compact space, we often need to fold them into spiral or meandering shapes. These bends in the waveguide introduce another concern: bending loss, signifying the loss of optical power due to the curves. Until recently, bending loss has been a limiting factor, preventing us from fully utilizing the entire length of the waveguide. Fortunately, in recent demonstrations, researchers have successfully reduced bending loss to levels below 0.01 dB per meter in waveguides with thicker cores (where the core height exceeds 0.6 µm) and waveguide widths around 2 µm [211]–[213].

Ensuring high optical confinement to the core is essential for enhancing nonlinear interactions, along with the loss of waveguides. The degree of optical confinement relies on the contrast between the core and cladding refractive index, as well as the dimensions of waveguides. The buried channel silicon nitride waveguides are typically cladded by silica which is not only compatible with the CMOS process but also demonstrates low optical loss and transparency. Consequently, the refractive index contrast of stoichiometric Si_3N_4 waveguides remains consistent. The dimensions can still be optimized to enhance the nonlinear interactions. The simulations show that the optical confinement in the core reaches its maximum
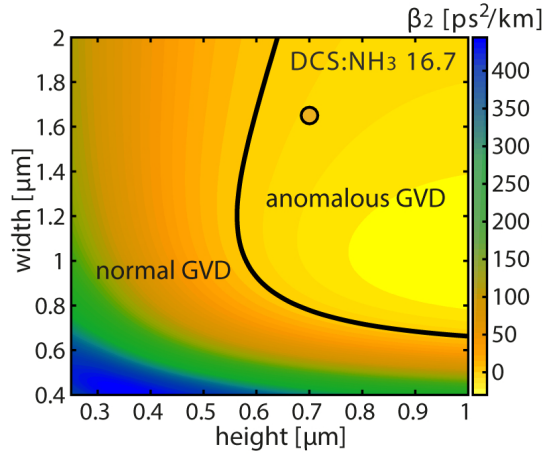
Figure 2.8: β_2 as a function of waveguide width and height of the silicon nitride waveguide at 1550 nm wavelength in TE polarization [215].

at specific dimensions. While the mode diameter decreases until reaching an optimal point with smaller dimensions, further shrinkage in the dimensions extends the mode field into the cladding, leading to a decrease in nonlinear interactions. [214].

The dispersion characteristics of the waveguides can be tuned under the previous conditions so as to broaden the operation bandwidth. The dispersion engineering via engineering the dimensions of the waveguide for TE polarization has been shown in various platforms [155], [162], [215]. In Figure 2.8, Kruckel et al. [215] simulated the dispersion characteristics of silicon nitride waveguides and confirmed them with experimental samples. The simulations indicate a strong change in dispersion with the smaller dimension. As one of the dimensions gets much larger than the other dimension the waveguide approaches a slab waveguide and the governing equations become dominated by the small dimension similar to Equation 2.5.

In addition to material selection, waveguide engineering plays a vital role in fine-tuning the waveguide properties for specific applications. The waveguide design significantly influences the coupling efficiency, mode shape and number, dispersion, nonlinearity, and loss. Our upcoming study in Chapter 3 will delve into the waveguide engineering aspects of stochiometric Si_3N_4 waveguides for experimental demonstration of efficient broadband wavelength conversion.

3 Efficient-Broadband Four-Wave-Mixing

In this chapter, efficient FWM in dispersion-engineered meter-long waveguides will be investigated in order to obtain efficient and broadband FWM. The dispersion engineering in ultra-low loss Si_3N_4 waveguides not only paves the way for broadband FWM but also unlocks distant phase-matching, that is the phase-matching satisfied at a far-detuned wavelength beyond the fundamental band, for efficient coherent light generation.

3.1   Dispersion Engineering in Silicon Nitride Waveguides

In order to obtain efficient broadband FWM in Si_3N_4 waveguides, determining the adequate waveguide cross-section dimensions has the utmost importance. In order to investigate the effect of the dimensions and possible fluctutations, the dispersion characteristics are simulated by COMSOL Multiphysics with the finite-element method. The refractive index data for the Si_3N_4 is provided by Dr. Junqiu Liu measured by spectral ellipsometry. Simulated effective indices of different modes Si_3N_4 waveguides are presented in Figure 3.1 for the heights of 0.6 and 0.8 µm and various widths between 0.6 µm and 1.6 µm at 1.55 µm wavelength. Depending on the waveguide dimensions, the waveguides support a few TE and TM modes at 1550 nm wavelength. The waveguides only support single TE and TM modes at 1.55 µm wavelength for waveguide width below 1 µm and 0.9 µm for the heights 0.6 µm and 0.8 µm, respectively. The number of modes increases with the width for both heights although 4 modes are supported in 0.6 µm height whereas 8 modes are supported for a height of 0.8 µm. For the widths beyond 1.6 µm, the same trend continues with more supported optical modes.

For nonlinear optics, the multimode operation has its advantages and drawbacks. The optical modes in at the same frequency are orthogonal to each other, resulting in a small nonlinear overlap integral, such as the one in FWM (Equation (2.17)). However, as the interacting waves have a higher frequency difference, the nonlinear overlap becomes notable. Moreover, the phase difference between the modes can compensate for the strong phase mismatch, such as that of far-detuned FWM in the same modes. This technique is known as intermodal phase-matching and has been demonstrated both in the fiber and waveguide domains [216], [217].
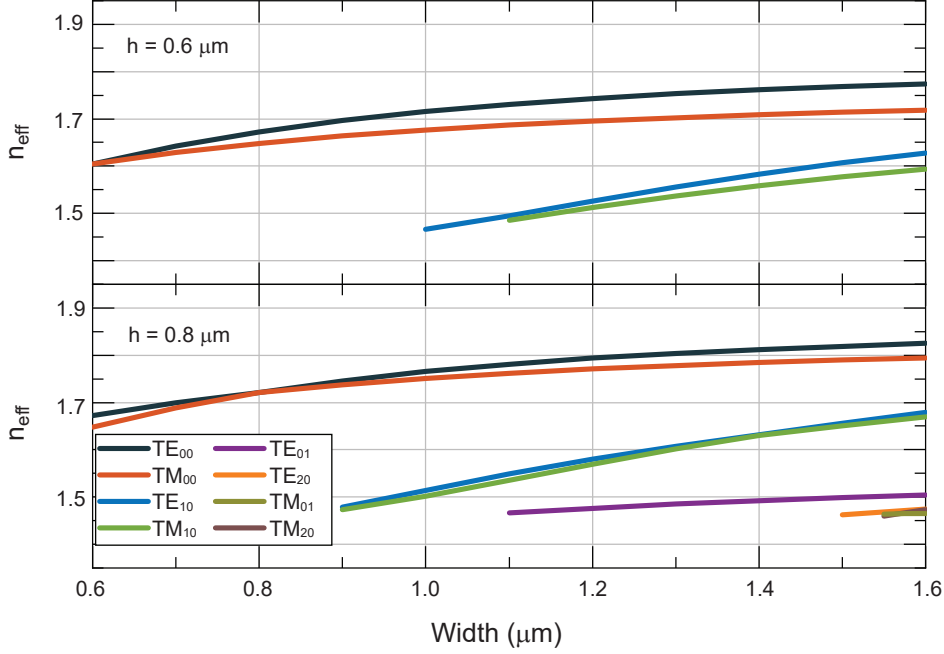
Figure 3.1: The effective refractive indices (n_{eff}) of the modes in the waveguides with various widths between 0.6 to 1.6 µm and the heights of 0.6 µm and 0.8 µm a 1550 nm wavelength. The graph also shows the number of modes excited in the waveguide for the given cross-sections

Nevertheless, for small frequency detunings, the intermodal FWM typically results in non-efficient conversion. Furthermore, in the case where all pump, signal, and idler are coupled to the same higher-order mode, the lower confinement results in a higher effective area and hence, lower CE. Therefore, the waveguides in this chapter will be engineered according to the fundamental TE and TM mode characteristics.

Single-mode waveguides offer operational simplicity by allowing only fundamental modes to be excited, ensuring fundamental mode operation. Furthermore, their compact dimensions result in superior light confinement and enhanced nonlinear properties. However, it's essential to acknowledge that these reduced dimensions often come at the cost of additional bending loss in Si_3N_4 waveguides as discussed in the preceding chapter. Consequently, until the development of low-loss single-mode waveguides, leveraging the substantial effective length of meter-long waveguides requires multimode operation.

The fundamental mode operation can still be obtained in multimode waveguides by ensuring fundamental mode coupling at the input of the waveguide. As optical modes are orthogonal, light coupled into the fundamental mode typically remains within that mode and does not couple into higher-order modes or other polarizations unless scattered. Various methods of waveguide coupling have been investigated such as grating couplers [218], prism couplers

Figure 3.2: For the fundamental TE mode, simulated (a) second-order dispersion at 1550 nm of wavelength, (b) the ZDW between 1350 and 2500 nm. Zero dispersion at 1550 nm is shown with a black straight line.

[219], graded index couplers[220], and inverse taper couplers [221], [222]. Moreover, the couplers can be engineered to selectively couple the desired mode [223]–[225]. The state-of-the-art grating couplers and inverse taper couplers in Si_3N_4 waveguides offer coupling efficiencies better than -1.5 dB [226], [227]. Specifically, the inverse tapers can operate in a larger bandwidth and they can be engineered to operate in a polarization-insensitive manner [228]. Such functionality can potentially overcome the disadvantages of multimode waveguides. Therefore, this subchapter will focus on 2 fundamental modes providing the highest confinement, namely, TE_{00} and TM_{00}, for waveguide width between 1.4 µm to 3.2 µm and height between 0.6 µm and 0.8 µm.

The analysis in this section commences with the fundamental TE mode, as the height of the waveguide is smaller than the width, resulting in superior light confinement in TE mode. Simulations were conducted to evaluate the waveguides' effective index, for wavelengths ranging from 1000 nm to 2500 nm. Additionally, calculations were performed to determine the group velocity dispersion (GVD) values of the waveguides and identify the zero-dispersion wavelength (ZDW) for the different waveguide cross-section dimensions. One such set of data of GVD at 1550 nm and location of the ZDW is presented in Fig, 3.2.

The findings reveal that the zero GVD condition at 1550 nm wavelength is met within a height range of 645 nm to 710 nm, depending on the waveguide's width. Notably, the dispersion characteristics exhibit a significant sensitivity to height variations, consistent with previous research indicating that smaller dimensions exert a more pronounced influence on GVD. It is worth noting that in Figure 3.2(a), the GVD experiences a substantial increase in the upper left or lower right corner, implying a narrower bandwidth for CE at 1550 nm.

The dispersion at 1550 nm might be too high for broadband wavelength conversion for certain dimensions. However, it does not preclude the waveguides from offering broadband wavelength conversion at different operating wavelengths, which can find utility in various applications. By optimizing both the width and height of the waveguide, it becomes feasible
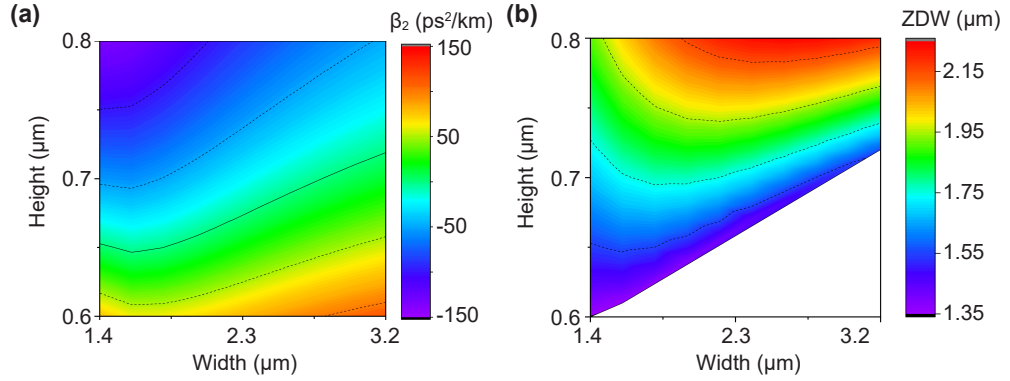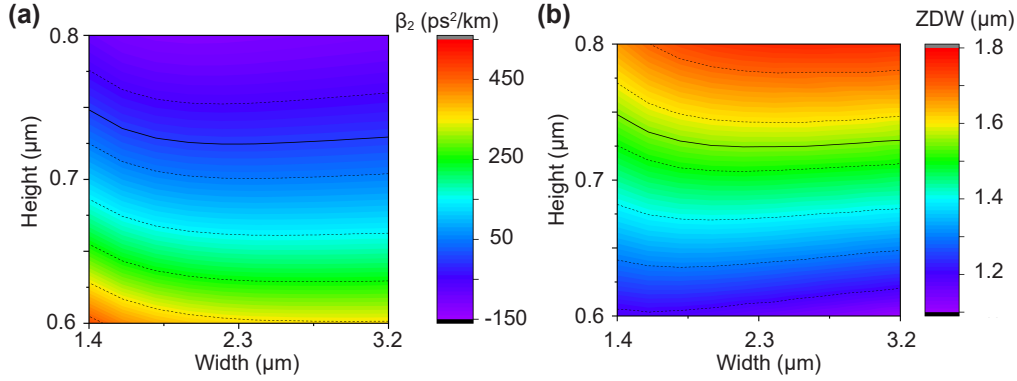
Figure 3.3: For the fundamental TM mode, simulated (a) second-order dispersion at 1550 nm of wavelength, (b) ZDW between 1200 and 2500 nm. Zero dispersion at 1550 nm is shown with a black straight line.

to tune the zero-dispersion wavelength (ZDW) within the range of 1350 nm to 2150 nm (as illustrated in Figure 3.2 (b)). When we compare the right side (wide waveguides) to the left side (narrow waveguides) of the graph, it can be seen that the ZDW exhibits significant variation for both cases although the sensitivity to the height is more dominant for wide waveguides. A 50 nm change in height can shift the ZDW by more than 400 nm at 3.2 μm waveguide width. However, the stronger dependence of wider waveguides on height is not observed for GVD. Therefore, wide waveguides can provide a low GVD despite the ZDW being detuned to longer wavelengths. For applications that demand broadband conversion at both 1550 nm and 2000 nm pump wavelengths in TE polarization, wide waveguides can offer distinct advantages in that sense. On the other hand, the narrower waveguides have the ability to tune the ZDW to shorter wavelengths which is not possible with the wide waveguides. The simulations observed no ZDW on the lower left corner within the simulated wavelength span. Additionally, it is important to note that some of the waveguides were observed to have multiple ZDWs at shorter wavelengths in the simulations, although this is not depicted in the current graph.

The dispersion characteristics are also simulated for fundamental TM mode. The corresponding GVD at 1.5 μm and ZDW are presented in Figure 3.3 for various widths and heights. Similar to the TE case, the influence of waveguide height on dispersion characteristics was observed. Notably, for the TM polarization, the effect of height was even more pronounced than for TE polarization. The zero-dispersion wavelength appears at 1550 nm for waveguides within a height range of 725 nm to 750 nm, depending on the waveguide width. Additionally, it was noted that the ZDW tends to shift to shorter values compared to the TE polarization case. Engineering the dimensions hence enables tuning the ZDW across a wide spectrum when using TM polarization, ranging from 1100 nm to 1800 nm.

The Si_3N_4 waveguides studied exhibit the potential for providing broadband operation in different spectral regions by leveraging polarization according to the simulation results. The GVD for both fundamental TE and TM modes in Si_3N_4 waveguides with various widths and
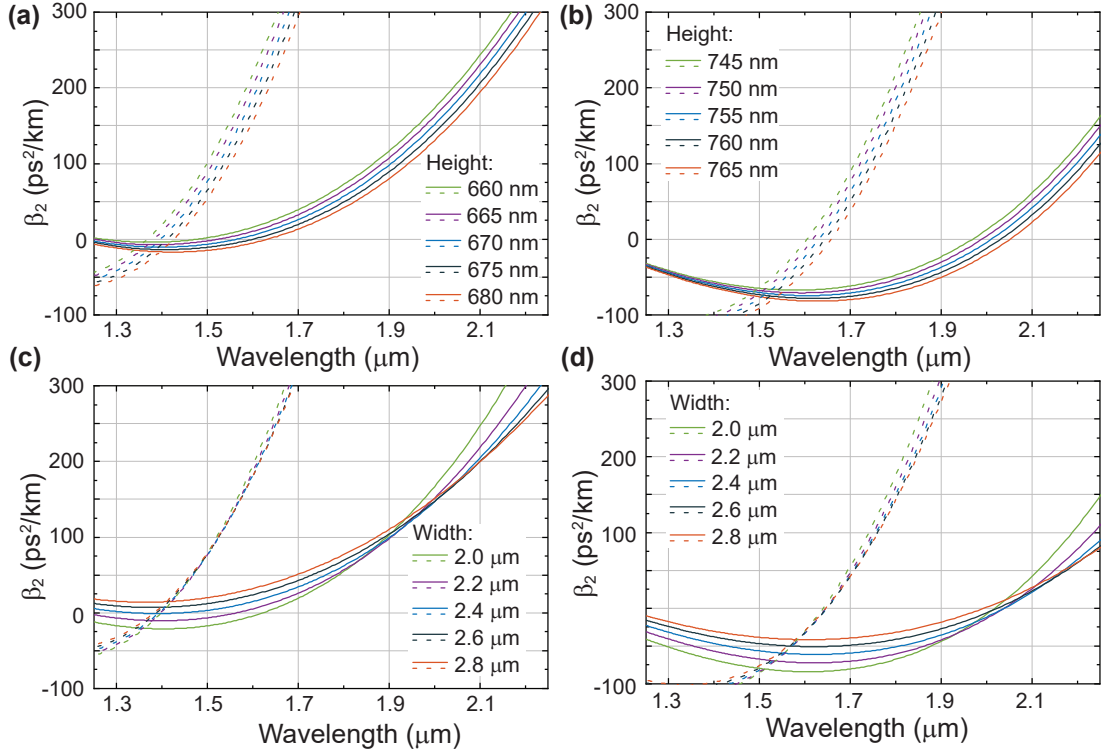
Figure 3.4: Theoretical GVD vs wavelength for 2.2 μm width and heights of (a) 660 nm, 665nm 670 nm, 675 nm, and 680 nm (b) 745 nm, 750 nm 755 nm, 760 nm, and 765 nm. Theoretical GVD vs wavelength for 2.0 μm, 2.2 μm, 2.4 μm, 2.6 μm, and 2.8 μm widths and height of (c) 670 nm (d) 760 nm. Dashed lines represent the fundamental TM mode and solid lines represent the fundamental TE mode.

heights are presented in Figure 3.4(a)-(d). As broadband conversion requires low GVD values, a switchable broadband operation can be observed at different wavelength ranges by changing the polarization. For instance, waveguides with heights around 750 nm enabled broadband operation around 1600 nm for the fundamental TM polarization and approximately 2000 nm for the fundamental TE polarization. Similarly, when heights are set to approximately 670 nm, broadband operation appears feasible at 1550 nm for TE polarization and within the range of 1300 nm to 1400 nm for TM polarization. Such polarization-leveraged broadband conversion and far-detuned phase-matching, as it will be explained later on, unlock numerous possibilities for diverse operations and facilitate light generation across a broad spectrum.

3.2 Polarization-leveraged broadband FWM

The potential of polarization-leveraged broadband FWM estimated by the simulations is experimentally tested in Si_3N_4 buried-channel waveguides fabricated by the Damascene process [188]. The waveguides are designed in the form of spirals having straight segments and circular turns connecting them (referred to as bend segments). The radii of curvature
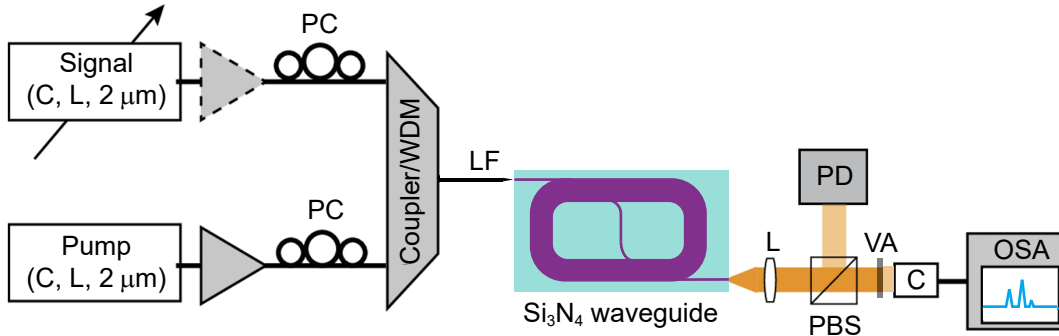
Figure 3.5: Experimental setup. PC: polarization controller, WDM: wavelength division multiplexer, LF: lensed fiber, PBS: polarization beam splitter, PD: photodetector, VA: variable attenuator and OSA: optical spectrum analyzer.

of the bend segments are set to 230 μm. Inverse taper couplers are employed for efficient fundamental mode coupling to the waveguide. The waveguides have a length of 0.5 meters and nominal width × height dimensions of 2.1 μm × 0.745 μm, 2.0 μm × 0.760 μm, and 2.3 μm × 0.755 μm.

The fabricated waveguides underwent testing using a traveling wave pump-probe architecture. The experimental setup, as depicted in Figure 3.5, employs different source sets. These sources include tunable continuous-wave (CW) telecommunication lasers covering the C/L bands and 2 μm lasers, comprising a fixed-wavelength semiconductor source and a custom-built tunable thulium fiber laser (TDFL). Besides the TDFL, the pump and signal seeds are amplified before being combined, either through a wavelength-division multiplexer (WDM) or a fiber power coupler, and then coupled into the waveguide using a lensed fiber. The estimated input coupling loss is approximately 6 dB for telecom wavelengths and 5 dB for 2 μm wavelengths. The output light is collected using a lens and collimated back into a fiber, allowing the spectrum to be measured on an optical spectrum analyzer (OSA). Depending on the wavelength range being monitored, we employ either the Yokogawa AQ6376 (covering 1500 to 3400 nm) or AQ6375B (covering 1200 to 2400 nm). The polarization states of both beams are actively controlled and monitored at the output of the waveguide using a polarization beam splitter.

3.2.1 Theoretical FWM CE calculations

As introduced in the previous chapter, theoretical CE calculation in a given waveguiding structure requires the nonlinear parameter, γ, pump power, P_p, length of the waveguide, L, absorption coefficient, α, and the phase mismatch κ of the process. The nonlinear parameter is calculated with the refractive index $n_2 = 2.4 \times 10^{-19} \mathrm{m}^2/\mathrm{W}$ [158] and effective area retrieved from the mode simulations on COMSOL with finite-element method. The propagation constants of the pump, signal, and idler, β_p, β_s, and β_i, are also retrieved from the same simulations in order to calculate the phase mismatch. The absorption coefficients are

measured with transmission experiments where the coupling loss is assumed to be constant in different waveguides identically fabricated inverse tapers on the same fabrication run.

For calculation of FWM efficiency and gain, Equations (2.23) and (2.24) are derived according to the no pump depletion and no loss assumption. Although no pump depletion assumption is valid throughout the FWM characterizations in this thesis, no loss assumption is not as the αL factor is significantly high. Thus, to include the effect of the loss the Equations are modified to include the idler and signal generation in the infinitesimal length, and the loss is introduced afterward. The idler and signal generation equations in the infinitesimal length are

$$A_s'(\Delta z) = \left(\cosh(g\Delta z) + \frac{i\kappa}{2g}\sinh(g\Delta z)\right)e^{i(\gamma P_p - \frac{\kappa}{2})\Delta z}A_s(0) + \frac{i\gamma P_p}{g}\sinh(g\Delta z)e^{i(\gamma P_p - \frac{\kappa}{2})\Delta z}A_i^*(0)$$
(3.1)

$$A_i'(\Delta z) = \left(\cosh(g\Delta z) + \frac{i\kappa}{2g}\sinh(g\Delta z)\right)e^{i(\gamma P_p - \frac{\kappa}{2})\Delta z}A_i(0) + \frac{i\gamma P_p}{g}\sinh(g\Delta z)e^{i(\gamma P_p - \frac{\kappa}{2})\Delta z}A_s^*(0)$$
(3.2)

$$A_p'(\Delta z) = A_p(0)$$
(3.3)

where A_p', A_s', and A_i' represent the pump, signal and idler mode are scaled mode field amplitudes of pump, signal, and idler before the loss acting on them. After the generation the loss is introduced, that is

$$A_s(\Delta z) = A_s'(\Delta z)\sqrt{e^{-\alpha\Delta z}}$$
(3.4)

$$A_i(\Delta z) = A_i'(\Delta z)\sqrt{e^{-\alpha\Delta z}}$$
(3.5)

$$A_p(\Delta z) = A_p'(\Delta z)\sqrt{e^{-\alpha\Delta z}}$$
(3.6)

The process is repeated iteratively m times where m = L/Δz. The infinitesimal length is chosen as $\alpha\Delta z < 0.05$ dB.

3.2.2 Broadband parametric wavelength conversion around 1.6 µm

The measurement of CE holds paramount importance in the characterization of wavelength conversion systems. For practical applications, CE defined as how much idler power is generated at the output of the system per unit of injected signal power at the input side, serves as a critical metric for evaluating the performance of a wavelength conversion system. However, from a physical standpoint, such CE definition encompasses not only the nonlinear interactions but also the linear losses within the system, such as propagation loss and coupling loss. While optimizing a wavelength conversion system ultimately necessitates addressing these optical losses, this thesis focuses on assessing the efficiency of nonlinear interactions. Therefore, CE will be defined as the generated idler power at the output divided by the signal power at the output. This definition allows the effects of optical losses on signal and idler
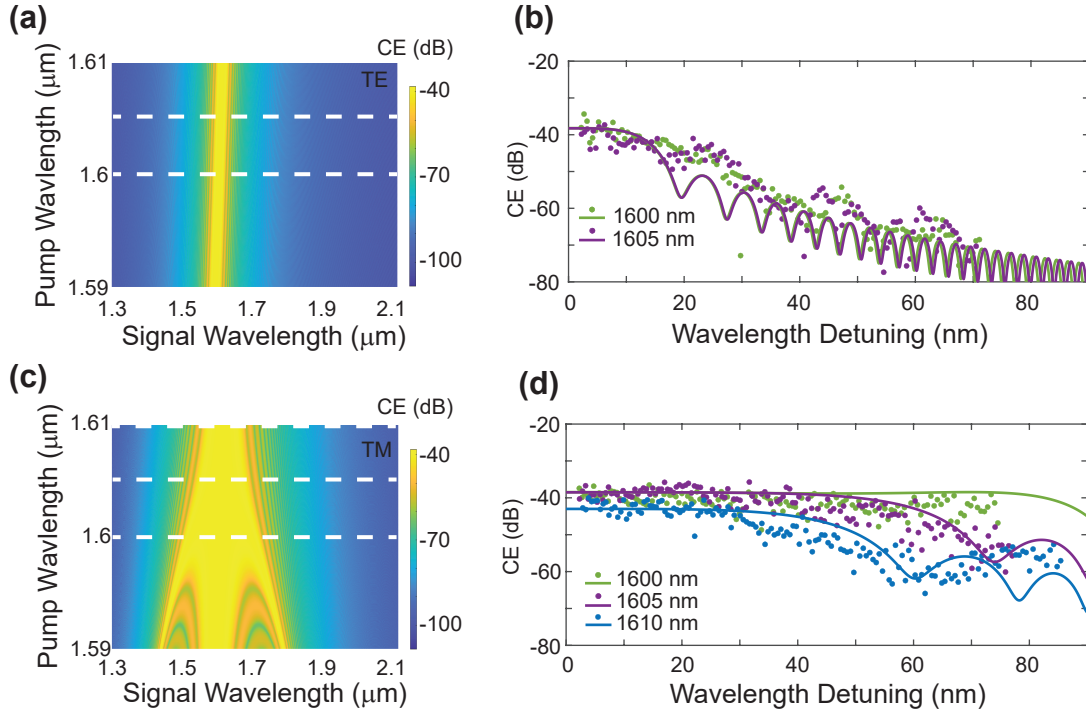
Figure 3.6: (a) Simulated contour graph of CE (dB) of the 2.1 µm × 0.745 µm waveguide for TE polarization and telecom band pumping; (b) Experimental CE (dots) and theoretical CE (lines) for TE pumping at 1600 nm and 1605 nm with 75 mW of coupled pump power; (c) Theoretical contour graph of CE (dB) of the 2.1 µm × 0.745 µm waveguide for TM polarization and telecom band pumping; (d) Experimental CE (dots) and theoretical CE (lines) for TM pumping at 1600, 1605 and 1610 nm with 50 mW of coupled pump power.

to cancel each other, which are expected to be similar for small wavelength detuning, thus focusing the evaluation on nonlinear interaction efficiency. Hence, with such a definition, the CE can be compared to the Equations (2.25), (2.27) and (2.28).

Another crucial factor to consider when evaluating the CE potential of the system is the duty cycle of the input light. For FWM, which is a nonlinear interaction, the efficiency of the process is influenced more by the instantaneous power rather than the average power. Since the efficiency increases with the square of the pump power, compressing the optical energy of the pump into shorter pulses can significantly enhance efficiency. However, operating in a pulsed mode necessitates careful optimization of the temporal walk-off between the pump and signal. Furthermore, using short pulses comes with a drawback – they often have a wide linewidth in the frequency domain. This wider linewidth might be a liability for applications requiring narrow linewidth light, such as spectroscopy. Therefore, the characterization of the platform in the CW domain is common to anticipate the potential of the system and to provide a figure of merit that can be enhanced via modulation of the light tailored for specific applications.

The CEs in the 0.5 m long waveguides are first calculated by Equations (2.23) and (2.24) using the simulated propagation constant for different pump and signal wavelengths. The A_{eff} extracted from COMSOL simulations to calculate the nonlinear parameter, γ, taking n_2 = 2.4x10^{-19} m^2/W [158]. The propagation loss of the waveguide is taken according to the measurement of constant 5.5 dB/m at 1550 nm. In Figure 3.6(a), a contour map of CE is presented for the 2.1 μm × 0.745 μm waveguide pumped in the telecommunication band and for a 50 mW of coupled pump power in TE polarzation. The y-axis shows the pump wavelength and the x-axis shows the signal wavelength. Note that signal idler wavelengths are interchangeable and correspond to the same frequency due to the inherent symmetry of the FWM process. The color scale represents the simulated CE, expecting an almost constant narrow-band wavelength conversion bandwidth. The relatively lower change in the GVD with the pump wavelength compared to the absolute value of GVD causes no significant bandwidth variations over the probed wavelength band. The experimental characterization of the waveguide with the cross-section of 2.1 μm × 0.745 μm in 1600 and 1605 nm pump wavelengths confirms the simulated trend. In Figure3.6(b), the TE experimental CEs for two pumping wavelengths are plotted together with the simulated curves. The coupled pump power is estimated to be 75 mW. The CE quickly drops as the wavelength detuning increases. No significant difference in the CE plot is observed between 1600 nm and 1605 nm pump wavelength.

For TM polarization, Figure 3.6(c) illustrates a distinct behavior in the same waveguide. Pumping around the theoretical 1603 nm ZDW can yield a considerably broader bandwidth. However, an even broader bandwidth can be achieved by slightly detuning the pump wavelength, taking advantage of the merging of the main phase-matched band around the pump with the higher-order phase-matching, facilitated by the opposite signs of β_2 and β_4. In Figure 3.6(d), we present the experimentally obtained CEs for TM polarization with varying idler wavelength detuning. At the 1600 nm pump wavelength, a broadband and flat CE can be achieved. As anticipated by the simulations, the bandwidth begins to decrease as the pump wavelength increases. A slightly lower CE is observed at a 1610 nm pump wavelength, attributed to a reduction in coupled pump power from 50 mW to 40 mW. Figure 3.6(b) indicates that pump wavelengths below 1600 nm would lead to a separation between the primary and high-order phase-matched lobes, potentially reducing the bandwidth. At the 1600 nm pump wavelength, we observe a two-sided 3 dB bandwidth of 150 nm, constrained by the tuning range of the signal wavelength. Simulations suggest that a two-sided 3 dB bandwidth as wide as 160 nm can be achieved at the same wavelength.

The FWM experiment is repeated in the waveguide with a cross-section of 2.3 μm × 0.755 μm to confirm the predicted effects of the dimensions. The simulation results anticipate the ZDW to shift to 1630 nm (as can be seen in Figures 3.3 and 3.4). However, the available L-band erbium-doped fiber amplifiers only extend up to 1615 nm on the long-wavelength side. Consequently, the waveguide underwent characterization at pump wavelengths of 1604 nm, 1609 nm, and 1614 nm to test the change in the bandwidth. The normalized CE values for both TE and TM polarizations are presented in Figure 3.7 (a) and (b). In TE polarization,
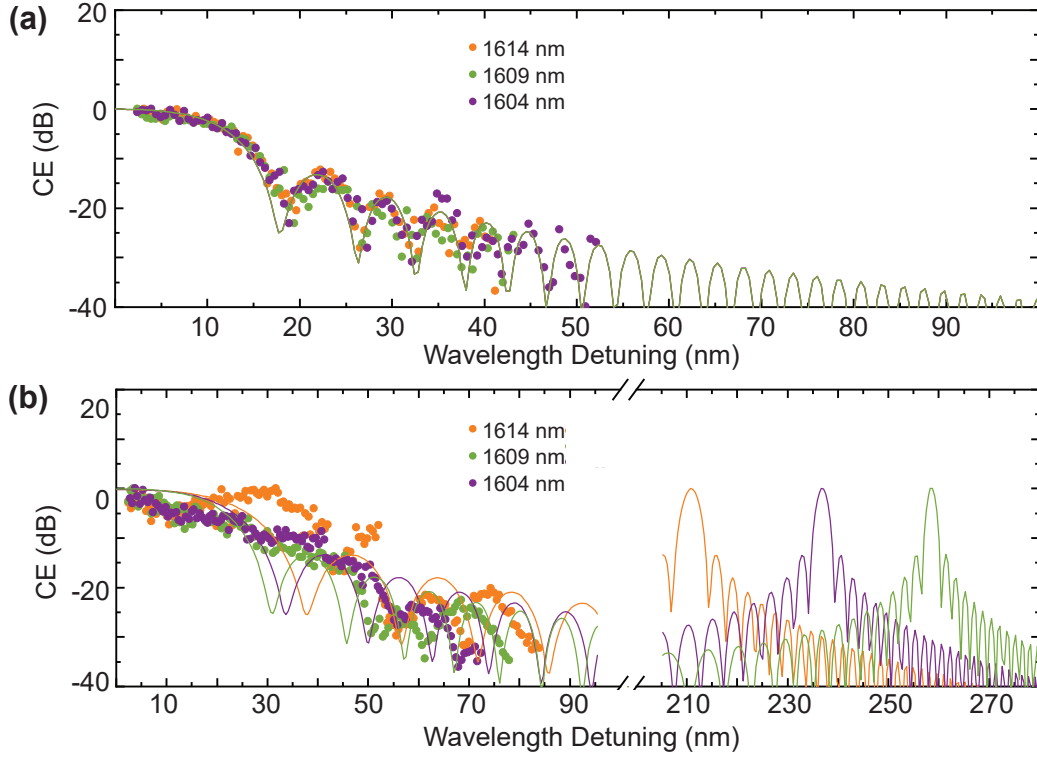
Figure 3.7: (a) Normalized experimental CE (dots) and theoretical CE (lines) for TE pumping at 1604, 1609 and 1614 nm in the waveguide with 2.3 µm × 0.755 µm cross-section; (b) Normalized experimental CE (dots) and theoretical CE (lines) for TM pumping at 1604, 1609 and 1614 nm

the observed trend closely resembles the measured CE in the 2.1 µm × 0.745 µm cross-section waveguide. The relatively higher and flat dispersion resulted in an almost identical CE across wavelength detuning, exhibiting a two-sided 3 dB bandwidth of 22 nm for the tested pump wavelengths. The maximum CEs, reaching around -29 dB, were recorded at an estimated coupled power of 100 mW.

For TM polarization, the disparity in GVD in comparison to the waveguide with dimensions of 2.1 µm × 0.745 µm becomes notably more pronounced. According to simulations, the bandwidth is considerably narrower than that of the 2.1 µm × 0.745 µm waveguide. Theoretically, a two-sided 3 dB bandwidth of 37 nm, 40 nm, and 45 nm is anticipated at pump wavelengths of 1604 nm, 1609 nm, and 1614 nm, respectively. However, experimental measurements indicate a broader bandwidth compared to the theoretical expectations. The two-sided 3 dB bandwidth can extend as broad as 80 nm, although accurately measuring the bandwidth is challenging due to fluctuations. The highest CEs, reaching around -39 dB, are observed at an estimated 40 mW coupled pump power.

Theoretical calculations also suggest that phase-matching can be achieved at significantly far-detuned wavelengths, exceeding 200 nm from the pump wavelength, given the specific pump power levels. When the phase mismatch terms with β_2 and β_4 counteract, it results in efficient
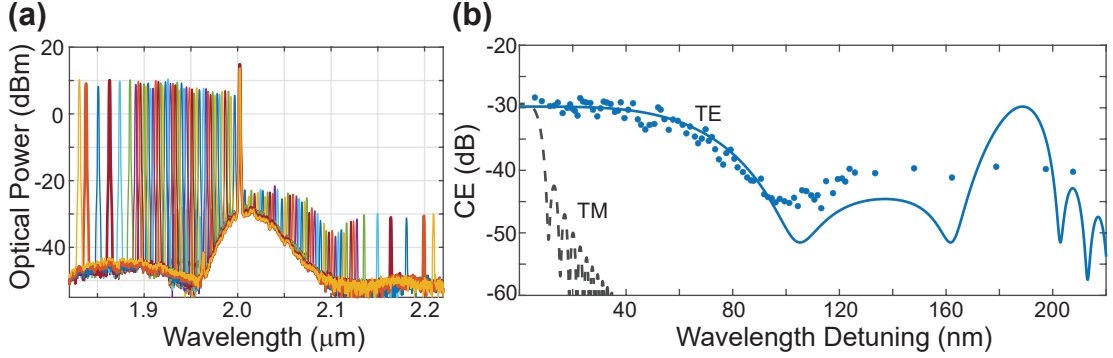
Figure 3.8: (a) Superimposed experimental FWM spectra in the 2.0 µm × 0.760 µm waveguide for a 2.004 µm pump and tunable TDFL for TE polarization; (b) Experimental CE (dots) and theoretical CE (lines) for TE pumping at 2004 nm with 200 mW of coupled pump power. Theoretical TM CE is plotted in dashed line.

wavelength conversion at certain detuned wavelengths, which will be referred to as distant phase-matching. Furthermore, the change in dispersion with varying pump wavelengths can be utilized to tune the distant phase-matched wavelength, thereby providing control over the generated idler wavelength. Such distant phase-matched FWM will be investigated in the upcoming sections.

3.2.3 Broadband FWM around 2 µm in TE polarization

Broadband wavelength conversion around 2 µm can be achieved by exploiting TE pump polarization. In this experiment, an available laser diode source emitting at a wavelength of 2004 nm is amplified using a thulium-doped fiber amplifier to serve as the pump. A custom-made TDFL pumped at 1565 nm is employed as the signal source, which is tunable in the range of 1820 nm to 2000 nm. Based on contour CE maps presented in Figure 3.2, the waveguide with dimensions of 2.0 µm × 0.760 µm is identified as having the highest potential for flat and broadband conversion when using this fixed pump wavelength, as predicted by simulations.

The measured spectra at the output of the waveguide, with a 200 mW coupled pump power, for various signal wavelengths ranging from 1820 nm to 2000 nm are superimposed and presented in Figure 3.8(a). The retrieved CE vs. idler wavelength detuning is plotted in Figure 3.8(b). The data aligns well with the theoretically expected CE, revealing a two-sided 3 dB bandwidth of 120 nm. Efficient idler generation extending up to 2200 nm is achievable, which could open up possibilities for employing such Si_3N_4 waveguides in specific sensing and spectroscopy applications. The bandwidth is, once again, limited by the tuning range of the TDFL.

A discrepancy is observed in the further detuned band. Higher-order dispersion terms are more sensitive to waveguide dimension fluctuations and the increased optical loss of the waveguide. A potential change in optical loss could account for the flattening of the curve
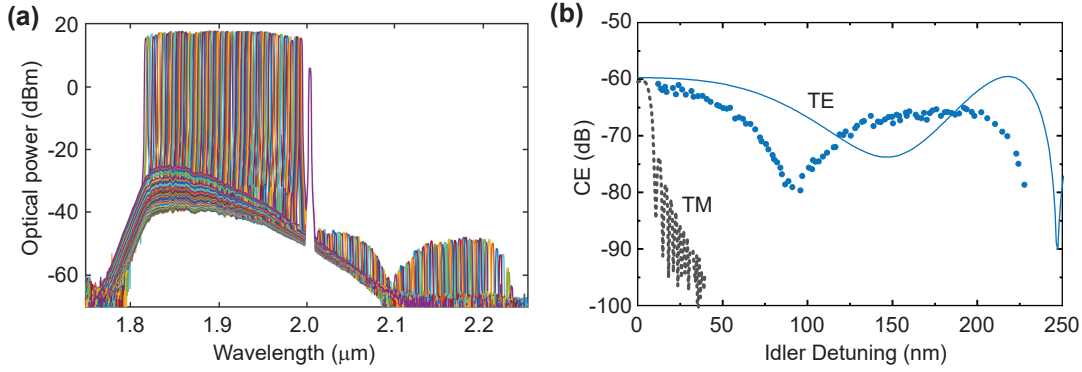
Figure 3.9: (a) Superimposed experimental FWM spectra in the 2.3 μm × 0.755 μm waveguide for a 2.004 μm pump and tunable TDFL for TE polarization; (b) Experimental CE (dots) and theoretical CE (lines) for TE pumping at 2004 nm with 10 mW of coupled pump power. Theoretical TM CE is plotted with a dashed line.

and the relative drop in CE at the higher-order matching. Dimensional fluctuations along the 0.5 m long waveguide tend to flatten the peak, similar to observations in optical fibers [229]. According to simulations, an even broader bandwidth can be achieved by slightly red-detuning the pump wavelength; however, this is constrained by the capabilities of the laser diode used in our setup.

When the pump and signal are set to TM polarization, no idler power can be distinguished from the strong optical noise coming from the amplified spontaneous emission of the thulium-doped fiber amplifier. Such a low idler power indicates that CE < -35 dB in TM polarization. Moreover, the rapid drop in the CE with the wavelength detuning also prevented the measurement of idler in the relatively far-detuned region, as expected from the simulations.

The FWM experiment, conducted at a 2004 nm pump wavelength, is repeated in the waveguide with a cross-section of 2.3 μm × 0.755 μm. The simulations suggest an even larger bandwidth due to the merging of the distant phase-matching lobe with the fundamental one. For experimental measurement, a bandpass filter is introduced into the system to suppress the amplified spontaneous emission emanating from the thulium-doped amplifier. Although the filtering enables the measurement of the minimum CE accurately, it should be noted that the filter incurs a high injection loss (approximately 10 dB). Consequently, the coupled power drops to 20 mW, leading to a significant reduction in CE. The limits of increasing the CE will be investigated in the upcoming chapters.

The measured spectra at the waveguide output encompass 98 distinct signal wavelengths ranging from 1821 nm to 1997 nm. These spectra are superimposed and visually depicted in Figure 3.9(a). To minimize power fluctuations, a meticulous optimization process for the custom-built laser is performed at each wavelength, resulting in lower fluctuations of 2 dB. The measured CE vs. idler wavelength detuning is plotted in Figure 3.9(b). In the case of TE polarization, the measured two-sided 3 dB bandwidth appears to be approximately

90 nm, deviating from the expected 160 nm. Nevertheless, the measured two-sided 20 dB bandwidth can remarkably extend to as much as 420 nm. This broad bandwidth can be attributed to the counteracting effects of higher-order dispersion terms against GVD. The minor variations in the dimensions of the waveguide may account for the observed differences between simulations and measurements.

In these waveguides, polarization-leveraging opens up the possibility of achieving broadband operation. Specifically, it enables operation around 1600 nm for TM polarization and 2000 nm for TE polarization. The merger of the higher-order phase matching allows the broadening of the conversion bandwidth in the waveguides. In addition, such phase-matching can be exploited to efficiently generate the wavelengths beyond the bandwidth. In the upcoming section, distant FWM will be investigated theoretically and experimentally.

3.3   Distant wavelength conversion

The FWM process typically has higher phase-mismatch with the frequency detuning. Although such a condition can be overcome via intermodal phase-matching, it comes with a drawback of lower efficiency due to the lower overlap of the modes. For the FWM process with the pump, signal and idler all in the same mode, the phase mismatch approximates the Equation (2.32). However, although both β_2 and β_4 terms increase separately in the absolute value with frequency detuning, at a certain frequency, they can counteract to satisfy the phase matching. In addition, for normal dispersion with strong nonlinear phase mismatch, higher-order phase matching, i.e. phase matching with higher than second-order dispersion, is a way to obtain phase-matched conversion. Moreover, the frequency detuning at which the higher-order phase-matching is satisfied can be engineered with waveguide dimensions via tuning the β_2/β_4 ratio. In this section, distant phase-matched wavelength conversion will be investigated as shown in Figure 3.7. In this section, the distant FWM in the Si_3N_4 waveguide with the 2.3 µm × 0.755 µm cross-section will be analyzed theoretically and experimentally.

3.3.1   Simulations

Pump Wavelengths around 2 µm

In Figure 3.10(a) and (b), the theoretical CE contour plots are presented for pump powers between 1.87 µm to 2.03 µm and signal/idler wavelength between 1.4 µm to 2.8 µm are illustrated for TE and TM polarizations, respectively. It should be noted that the process is symmetric, i.e. exchanging signal and idler wavelength results in the same efficiency. The distant phase-matching is usually satisfied at a pump wavelength around ZDW as the second-order dispersion becomes comparable with the fourth-order dispersion term in the interested wavelength span.

For TE polarization, when the pump wavelengths exceed 2.012 µm, distant phase-matching

Figure 3.10: Theoretical contour graph of CE (dB) for (a) TE polarization and (b) TM polarization for pumping in the thulium band with 100 mW pump power.

becomes unattainable due to the same signs of second and fourth-order dispersion. Nevertheless, with shorter pump wavelengths, two distinct bands emerge symmetrically in the frequency domain. The central band provides the broadest bandwidth, representing wavelength conversion around the pump wavelength, as previously discussed. The contour map shown in Figure 3.10(a) also assists in identifying the idler wavelength for a given signal wavelength that satisfies the phase-matching criteria. If the signal wavelength is positioned within the short-wavelength distant phase-matching band, it generates an idler within the long-wavelength distant phase-matching band, and vice versa. Consequently, phase-matched idler generation can be achieved within the wavelength range of 2 μm to 2.8 μm, provided that the system is excited with a signal wavelength between 1.4 μm and 2 μm. For TM polarization, however, as the process occurs significantly far from the ZDW, distant phase-matching remains unachievable.

Pump Wavelengths around 1.6 μm

In the L band, around 1.6 μm, a different trend is observed. Figure 3.11 (a) and b) illustrates the theoretical CE contour plots for TE and TM polarizations, respectively. In the case of TE polarization, there is no anticipated distant phase-matching within the waveguides' transparency window. For TM polarization, on the other hand, a distant phase-matching band can be obtained. Although wavelengths exceeding 1.63 μm in the waveguide do not yield any distant phase-matching bands, these bands do begin to manifest at shorter wavelengths. Under this configuration, launching a signal within the distant phase-matched range spanning from 1.63 μm to 2.2 μm leads to phase-matched wavelength conversion, occurring between 1.2 μm and 1.63 μm at specific pump wavelengths.
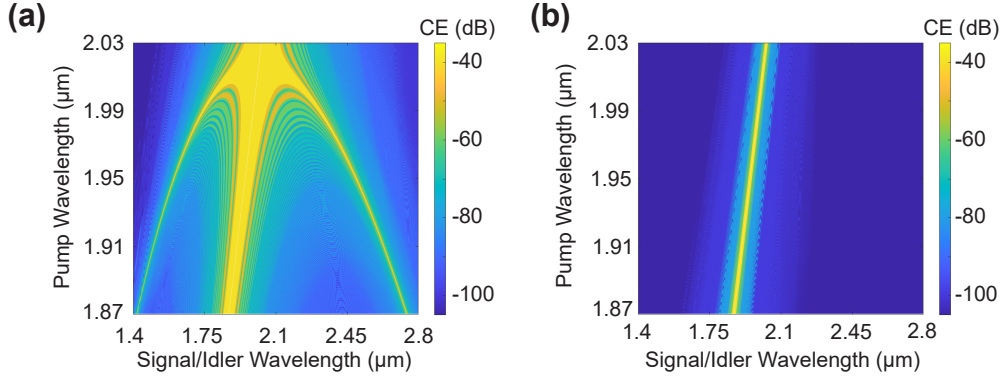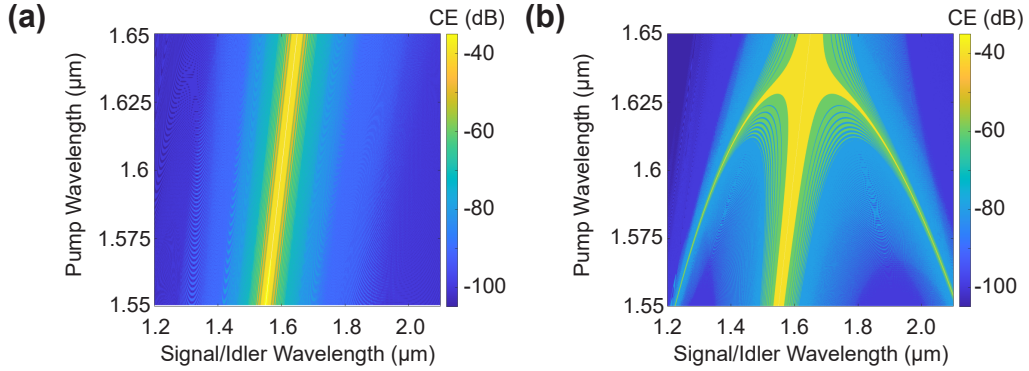
Figure 3.11: Theoretical contour graph of CE (dB) for (a) TE polarization and (b) TM polarization for pumping in the telecom band with 100 mW pump power

3.3.2 Experimental Results

After the theoretical calculations, distant phase-matching is experimentally investigated using the waveguide with 2.3 μm × 0.755 μm cross-section. A similar pump-probe setup including a WDM that combines the L band light with the thulium band one. The custom-built TDFL used in the previous section serves as the pump and the C/L-band sources are amplified by EDFAs to serve as the signal. The light is then collected with the chalcogenide lenses.

Pump Wavelengths around 2 μm in TE

The measured spectra for TE polarization and for a 1930 nm pump are shown in Figure 3.12 (a). The idler can be generated between 2400 m to 2600 m as the signal wavelength is swept from 1615 nm to 1537 nm. The idler reaches the highest power around 2550 nm, which is in agreement with the simulation results. The same experiment was repeated for 1910, 1935, 1940, 1945, 1950, and 1970 nm pump wavelengths. In all cases, the coupled pump power is estimated to be approximately 20 dBm. The experimentally measured values of CE are plotted in Figure 3.12 (b) for the different pump wavelengths and as a function of the generated idler wavelength. A phase-matched conversion between 2450 to 2550 nm can be obtained by tuning the pump wavelength between 1930 and 1950 nm, in agreement with the theoretical expectations. The phase-matched generation of the longer wavelengths requires shorter signal wavelengths than 1537 nm, which was limited by the operation range of the EDFA. However, after around 2660 nm, a significant drop in the CE is observed. In the given range, a maximum CE of -40 dB is measured for the estimated 100 mW CW pump.

Pump Wavelengths around 1.6 μm in TM

The same experiment is repeated after the polarizations are set to TM. The idler is now being projected to shorter wavelengths where the L band source is set as the pump. The experimental spectra for a 1600 nm pump are shown in Figure 3.13(a). Idler wavelengths shift from 1430
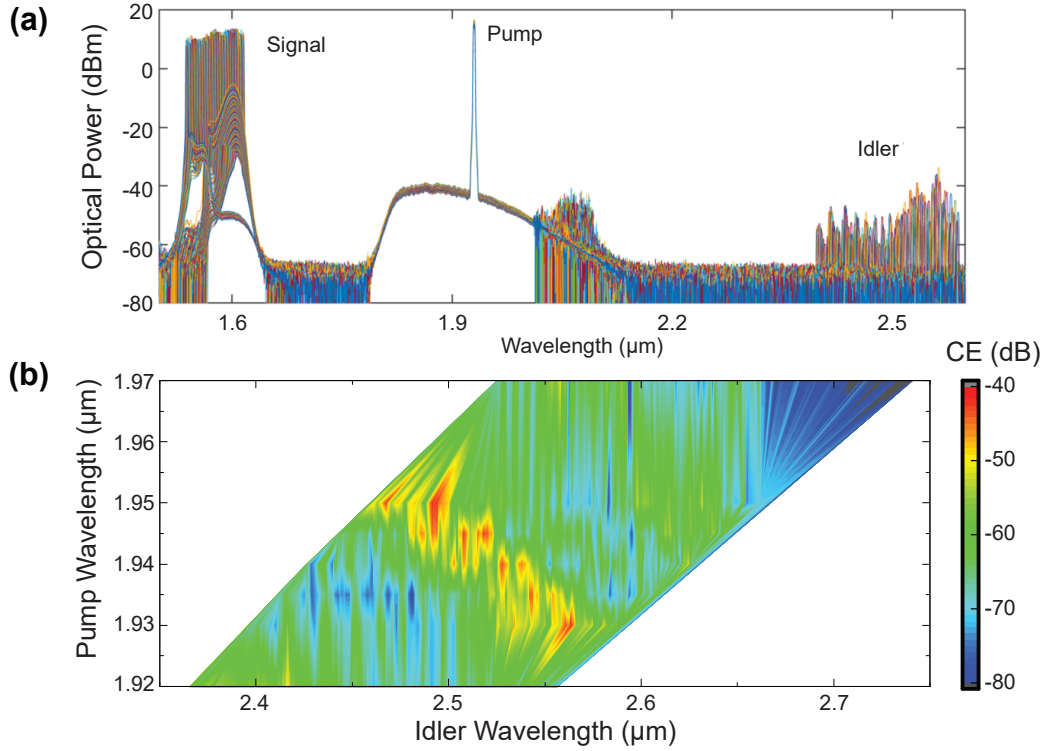
Figure 3.12: Experimental results for TE polarization. (a) Spectra from 1.5 μm to 2.6 μm for a 1930 nm pump and the signal swept from 1537 nm to 1615 nm. (b) Measured CE values for pump wavelengths of 1920, 1930, 1935, 1940, 1945, 1950, and 1970 nm, and signal swept from 1537 to 1615 presented in contour graph vs pump frequencies and frequency detuning values.

nm to 1330 nm as the signal moves from 1820 nm to 1975 nm. The maximum idler power is obtained around 1360 nm as expected by the theory. Once again, the experimentally measured CE values for pump wavelengths of 1615, 1610, 1607.5, 1605, 1600, 1595 and 1590 nm are presented in Figure Figure 3.13(b). The pump power is estimated at about 17 dBm. The frequency detuning at which phase matching is satisfied moves from 1340 nm to 1425 nm when the pump frequency moves from 1615 nm to 1590 nm, still in agreement with the estimated idlers by theory. The conversion is less efficient for TM polarization due to higher coupling loss compared to the TE polarization, reaching -46 dB for the 50 mW pump.

The measured distant phase-matched spectra are not as narrow or smooth (multiple peaks are observed) as expected from theory and simulations. Distant conversion is more sensitive to dispersion and loss, which can cause a broadening in the distant phase-matched band.

Power scaling measurements are conducted to assess distant wavelength conversion and narrow-band conversion in the L band. An optimized WDM is utilized within our experimental setup, enabling a more efficient coupling for two fixed wavelength seeds at 1600 nm and 1950 nm. For these wavelengths, phase-matched distant conversion can be satisfied for both TE and TM polarization. For TE polarization, the injected light at 1950 nm serves as a pump and
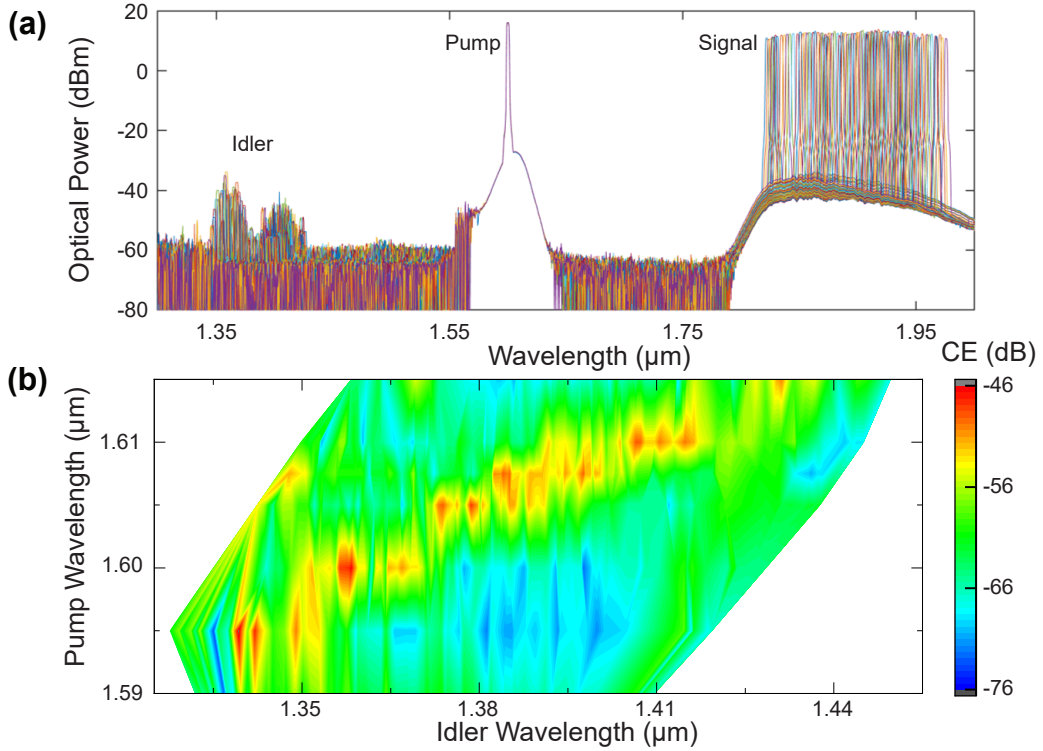
Figure 3.13: Experimental results for TM polarization. (a) Spectra from 1.3 μm to 2.0 μm for the pump wavelength of 1600 nm, for the signal wavelengths swept from 1821 nm to 1975 nm. (b) Measured CE values for pump wavelengths of 1615, 1610, 1607.5, 1605, 1600, 1595, and 1580 nm, and signal swept from 1821 to 1990 nm presented in contour graph vs pump frequencies and frequency detuning values.

the light at 1600 nm serves as the signal. The spectra are presented in Figure 3.14(a) where the generated idler is observed at 2494 nm. The CEs of the process as a function of pump power is presented in Figure 3.14(b). From the linear fit to the square of the pump power, of the graph, the nonlinear parameter of such distant conversion is calculated as 0.2 $W^{-1}m^{-1}$.

To leverage the polarization effect, both seeds at 1600 nm and 1950 nm are set to TM polarization without changing the wavelength. The idler is now efficiently generated at 1356 nm in this configuration as seen in Figure 3.14(c). The CE values for the TM polarization configuration as a function of pump power are shown in Figure 3.14(d). In this case the nonlinear parameter is found to be 0.12 $W^{-1}m^{-1}$. It's important to acknowledge some uncertainties in the measured power levels. Firstly, power fluctuations are observed at the output power of the TDFL. Secondly, given the broad wavelength range covered, there are inherent uncertainties in the actual values of signal and idler powers, as is typical in any platform. Lastly, it's worth noting that the optical loss of the waveguides was not characterized in the O band nor around 2.5 μm due to a lack of available sources. Such errors can account for part of the 10 dB lower CE in distant phase-matching compared to broadband conversion around 2 μm and in L-band.
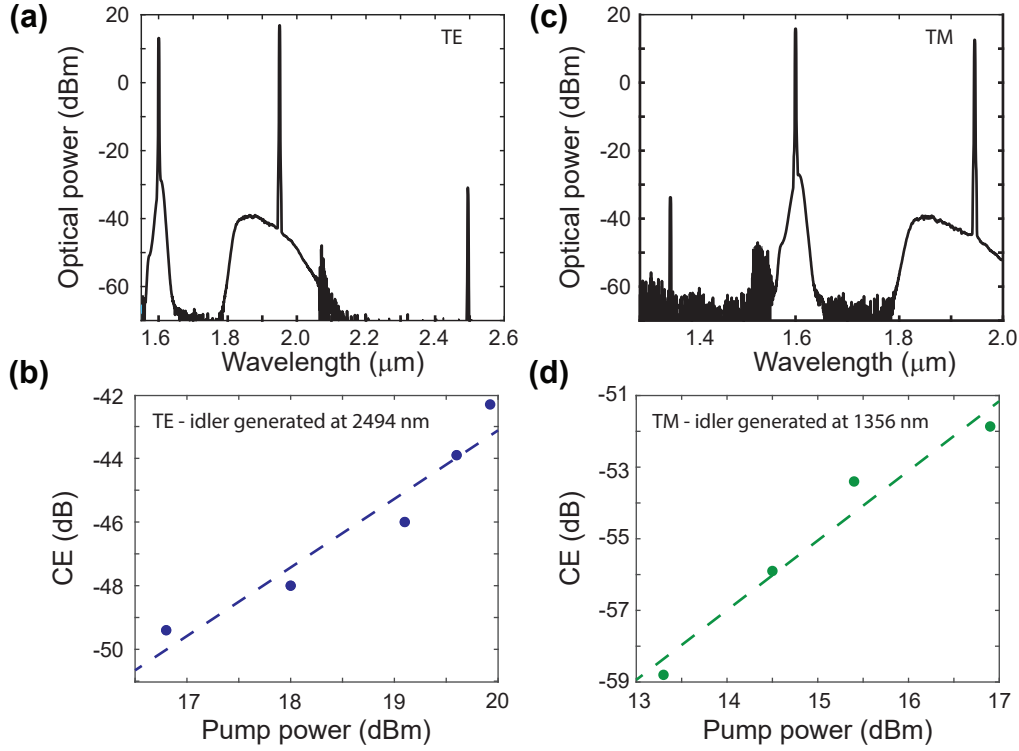
Figure 3.14: For TE polarization (a) optical spectra showing the generated idler at 2494 nm (b) CE vs pump power scaling pumping in the thulium band for various pump powers; for TM polarization (c) optical spectra showing the generated idler at 1356 nm (d) CE vs pump power scaling pumping in the thulium band for various pump powers

It's worth noting that relatively lower power levels were coupled in the experiments of this section as the main goal is to test the dispersion characteristics and phase-matching condition. Wavelength conversion in various bands in an optical range between 1330 nm to 2550 nm is observed proving the potential of the waveguides. However, the question of how much the CE, which has been relatively low, can be improved still persists. To enhance the CE, further experimentation will involve increasing the pump power and/or the effective length of the waveguides. These aspects will be explored in the upcoming section.

3.4 Efficient broadband FWM in telecommunication band

Together with broad bandwidth, numerous on-chip applications require efficient CE in the communication band. The broad bandwidth demonstrated in the previous subchapter comes with efficiencies in the order of -40 dB in the TM mode in L-band and -30 dB in the TE mode around 2 μm. To test the CE scaling with the pump power, a narrow-band FWM experiment is designed where the pump wavelength is set at 1570 nm and the signal wavelength is set at 1568 nm in the waveguide with 2.3 μm × 0.755 μm cross-section. For such a narrow band operation, the effect of dispersion is estimated to be negligible. The fiber couplers are replaced with a

Figure 3.15: CE as a function of pump power for a signal at 1568 nm and a pump at 1570 nm. Dashed lines are linear fits.

low-loss narrowband WDM that can combine efficiently the pump and signal wavelengths. This optimized setup enables coupled pump powers to go up to 500 mW. Consequently, the CEs can reach up to -24 dB for TM polarization and -18 dB in TE as can be seen in Figure 3.15. The CE scales with the square of the pump power, as expected from Equation (2.27), although some fluctuations are observed. The nonlinear parameter, γ, is extracted to be 0.66 $W^{-1}m^{-1}$ for TE and 0.45 $W^{-1}m^{-1}$ for TM. CEs can be enhanced by further increasing the pump power with an EDFA that can amplify the light to higher optical powers. Si_3N_4 waveguides are reported to operate efficiently up to 6 W of coupled pump power without two-photon absorption [190]. As a result, the phase-matched CE can potentially go up to 7 dB, calculated by Equation (2.25).

It's worth noting that the lower CE in TM polarization compared to TE polarization can be attributed to several factors. Firstly, the inverse tapers are optimized for TE polarization, and hence, injecting TM polarization reduces the coupled power. Secondly, the TM mode confines light less to the core compared to the TE mode, resulting in a slightly higher effective area and lower nonlinear parameter.

So far, the waveguides having 0.5 m length have been investigated. However, as the loss of the waveguides is around 6 dB/m the effective length can be increased over 1 m in the longer waveguides. The reduction of the loss below the 4 dB/m range further unlocks exploiting up to 2 m long waveguides providing a huge potential for further CE enhancement.

In this section, a new set of waveguides is designed to provide broadband in TE polarization in the telecommunication band with the lower expected propagation length in pursuit of efficient broadband wavelength conversion. The waveguides are designed to have a height of 670 nm in this section in order to provide broadband wavelength conversion in TE. Four different widths are experimented on to study the possible variation in GVD which might occur due to a fabrication fluctuation in the height of the waveguides. The available widths are 2.2 µm, 2.5 µm, 2.8 µm and 3.1 µm. The length of the waveguides are kept at 0.5 m in this section to provide a comparison with the broadband conversion in TM polarization demonstrated in

the previous chapter.

3.4.1 Wavelength dependence of BW

The analysis starts with measuring the conversion bandwidth at various pump wavelengths at the high coupled pump power in the 2.2 µm wide waveguide. This width is chosen because, at the intended height, the 2.2 µm wide waveguide is expected to provide the widest bandwidth. The simulations show that a ± 5 nm change in the height due to fabrication errors can alter the ZDW within the range of 1525 to 1590 nm. However, such a strong change in ZDW does not translate to a strong change in GVD, and $|\beta_2|$ remains below 5 ps^2/km. Consequently, despite the error in ZDW, it is expected to obtain a two-sided 3 dB bandwidth exceeding 80 nm in this waveguide.

The experimental setup includes a pump-probe architecture similar to the one shown in Figure 3.5 utilizing S/C or L band sources covering 1440 nm to 1660 nm. All sources are set to TE polarization and combined using various wavelength-division multiplexers (WDM) to minimize losses. The output light is then collected with a lens and collimated to the optical spectrum analyzer (OSA) Yokogawa AQ6375B. The polarization states of the pump, signal and idler beams at the output are monitored with the help of a polarization beam splitter (PBS) to ensure stable operation.

The waveguide is then characterized with 6 different pump wavelengths, 1537 nm, 1548 nm, 1550 nm, 1555 nm, 1563 nm, and 1570 nm, to experimentally test the dispersion characteristics. The signal wavelength is swept through the shorter wavelengths of the pump for 1537, 1548, 1550, and 1555 nm pump wavelengths and through the longer wavelengths for 1563 and 1570 nm. The wavelengths are chosen according to the availability of the WDMs.

The CEs, which are calculated by dividing the idler power at the output by the signal power at the output, are presented in Figure 3.17. Between 1537 nm to 1570 nm pump wavelength, two-sided 3-dB conversion bandwidth ranging between 70 to 95 nm can be obtained, indicating a slow change in the GVD as can be seen in Figure 3.17. Such slow change in the dispersion allows waveguides to provide broadband wavelength conversion in different portions of the spectra. The dispersion behavior slightly deviates from the ideal trace with the power fluctuation which will be later discussed in more detail. At 1550 nm pump wavelength, 95 nm of two-sided 3 dB bandwidth at -15 dB phase-matched CE can be obtained.

The phase-matched CEs also show strong variations. In the other waveguides, the coupled power is estimated to be 31 dBm ($\approx$ 1.25 W), assuming a 4.8 dB total coupling loss as reported before [188]. The highest CEs in the phase-matched portion of the graph show variations between -13 dB to -16 dB. The measured CEs are lower than the theoretically expected -9 dB at this power level (31 dBm). Moreover, similar to the previous waveguides, CE fluctuations which can get as high as 10 dB are observed, which will be addressed in the next chapter.
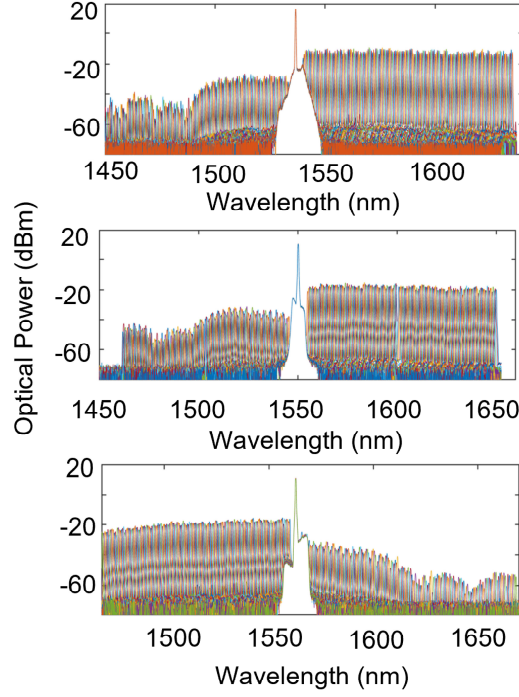
Figure 3.16: Superimposed optical spectra of four-wave-mixing for (a) pump wavelength of 1537 nm and the signal swept through 1540 nm to 1650 nm (b) pump wavelength of 1550 nm and the signal swept through 1554 nm to 1650 nm (c) pump wavelength of 1570 nm and the signal swept through 1450 nm to 1567 nm.

3.4.2   Waveguide width dependence of BW

In order to investigate the dispersion characteristics of the waveguides with different widths, the FWM CE in the waveguides with the widths 2.2, 2.5, 2.8 and 3.1 µm are tested for wavelength detunings up to 45 nm at 1550 nm pump wavelength. The measured CE values are presented in Figure 3.18 at the 31 dBm estimated coupled pump power. The broad bandwidth measured in 2.2 µwide waveguide drops steeply in the wider wavelengths. A similar 3 dB bandwidth of 16 nm has been observed in 2.5 µm and 2.8 µm wide waveguides possibly due to the variations in height. In 3.1 µm, after one data point of -14 dB CE at 4 nm wavelength detuning, the CE shows a slower drop with the increasing wavelength detuning which might be a result of higher-order mode interaction, which will be covered in Chapter 4.

The waveguide with a 2.5 µm cross-section exhibits a higher phase-matched CE due to its lower propagation loss (~ 2dB/m), aligning more closely with theoretical expectations. Lowering the propagation loss in 2.2 µm waveguides holds the potential for achieving -10 dB CE with a 95 nm two-sided 3-dB bandwidth at 1.25 W coupled pump power. In the subsequent section, we will explore the extent of efficiency improvement achievable with increased waveguide length and its impact on the bandwidth.
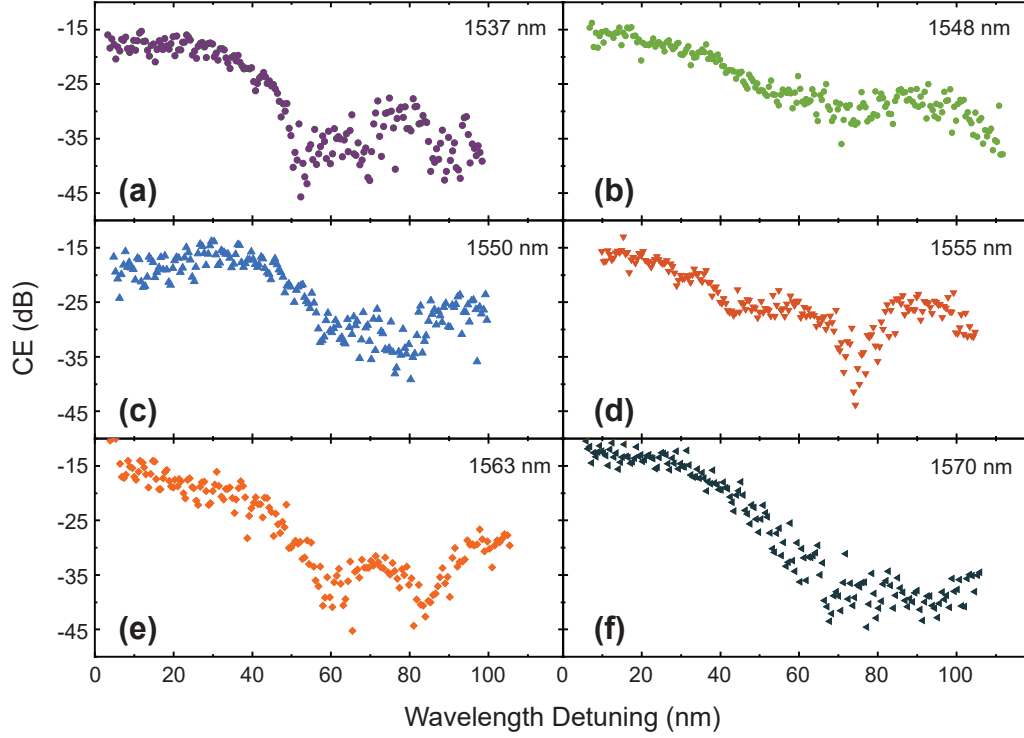
Figure 3.17: The CEs vs wavelength detuning for 2.2 µm width, 0.67 µm height and the wavelengths of (a) 1537, (b) 1548, (c) 1550, (d) 1555, (e) 1563 and (f) 1570 nm.

3.4.3 Length-bandwidth trade-off

Simulations

One possible approach to enhance operational efficiency is to extend the length of the waveguides, as long as the waveguide loss remains sufficiently low, albeit at the cost of reduced bandwidth. Under the low gain assumption, the phase-matched CE increases with the square of the effective length (Equation (2.27)) whereas the bandwidth shrinks with the square root of the effective length at high GVDs (Equation (2.33)) and with quadratic root when GVD is small so that fourth-order dispersion dominates (Equation (2.34)). Therefore, the enhancement in CE with effective length scales with the fourth power of the inverse bandwidth, i.e. $\Delta\Omega^{-4}$, for high GVD and the eighth power of the inverse bandwidth, $\Delta\Omega^{-8}$, in the vicinity of the ZDW.

The bandwidth and phase-matched CE for various lengths and propagation losses are shown in Figure 3.19(a). As the length increases a strong increase in the CE can be observed for the short waveguides as stated in the literature. However, as the length further increases the waveguides will be limited by the effective length of the waveguide, saturating both phase-matched CE and the bandwidth. For low-loss waveguides, higher phase-matched CE can be obtained without narrowing the bandwidth significantly. It should be also noted that as αL increases, the difference between phase-matched CE and the CE at the first minimum
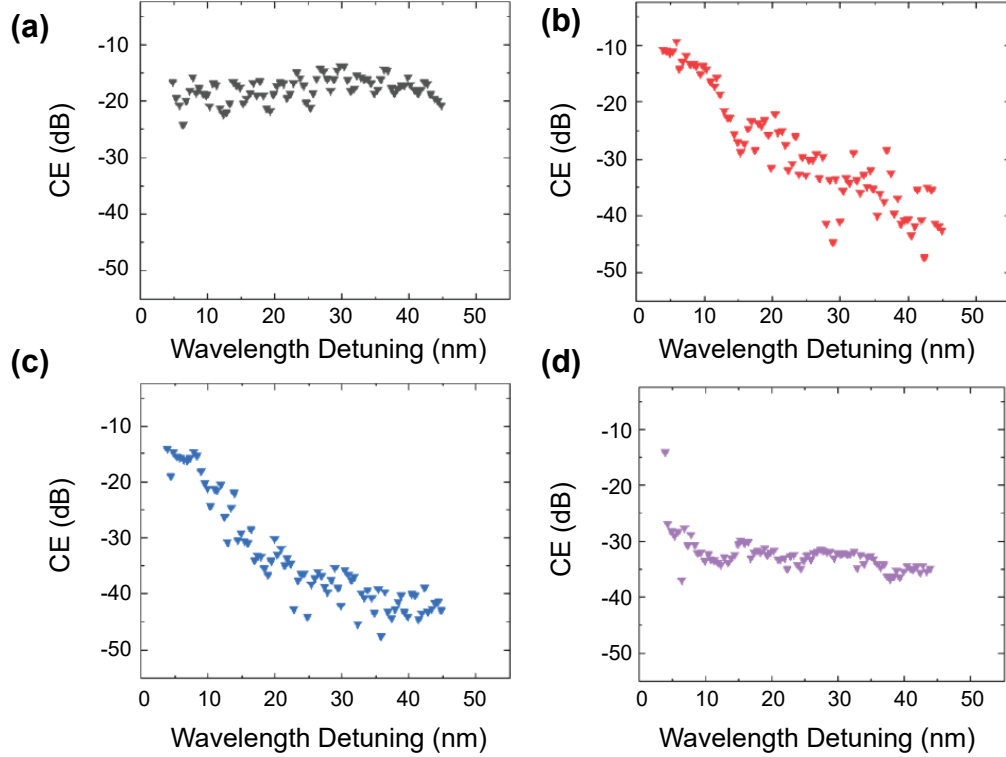
Figure 3.18: CE vs wavelength detuning for the height of 0.67 μm the wavelength of 1550 nm and the width of (a) 2.2 μm, (b) 2.5 μm, (c) 2.8 μm and (d) 3.1 μm.

decreases which can yield a broader 10 dB bandwidth or 20 dB bandwidth but a similar 3 dB bandwidth.

The phase-matched CE for the corresponding inverse bandwidth is shown in Figure 3.19(b). As the phase-matched CE is inversely proportional to the eighth power of bandwidth around ZDW, a slightly sublinear increase in the dB scale is observed. Operating in the waveguides with lower propagation loss can yield a higher CE at the same bandwidth.

In Figure 3.20(a)-(c), the simulated normalized CE development is displayed concerning waveguide length at a 1550 nm pump wavelength for three cross-sectional dimensions: heights of 0.66 μm, 0.67 μm, and 0.68 μm and 2.2 μm width.. It becomes evident that, for shorter waveguide lengths, the conversion bandwidth can be ultrabroad for all waveguides, primarily due to relaxed phase matching requirements. Notably, in the case of a 2.2 μm x 0.68 μm waveguide, the main phase-matched region around the pump merges with the higher-order, far-detuned phase-matched bands. However, as propagation extends beyond a few millimeters, the bandwidth experiences a significant reduction as a result of dispersion (see Figure3.20(a) and (c)). For our theoretical calculations, 4 dB/m loss is assumed, as an average value measured from the experiments.
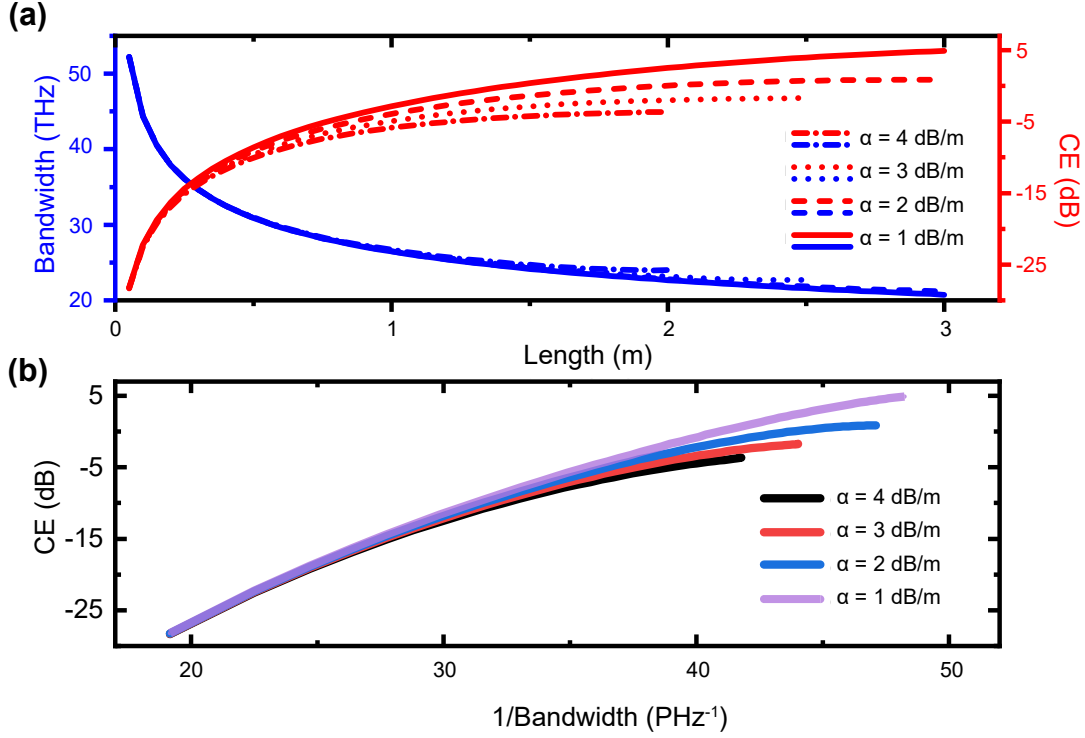
Figure 3.19: (a) The simulated conversion bandwidth (blue) and phase-matched CE in dB scale (red) at 1560 nm wavelength, with the cross-section of 2.2 μm width and 670 nm height for various waveguide lengths and optical loss.

Experimental Analysis

In the experimental investigation, three waveguides with a width of 2.2 μm and lengths of 0.5 m, 1.0 m, and 1.5 m will be examined for efficient broadband FWM. In addition, a set of 2.5 μm wide waveguides are included in the analysis as they are measured to have lower propagation loss. The available lengths in the waveguides with 2.5 μm width were 0.5 m, 1.0 m, 1.5 m and 2.0 m. These waveguides will be specifically investigated to measure the maximum CE that can be harnessed from the waveguides.

The experiment commenced with the loss measurements in the waveguides at various pump powers. TE polarized light with a wavelength of 1550 nm was coupled to the waveguide using a lensed fiber. The light is coupled out by focusing the light onto a powermeter using a lens. To monitor the input optical power, we employed a 99-1 coupler, where 1% of the light was measured and 99% was coupled to the waveguide.

The optical power measured at the output is plotted against the input optical power, as shown in Figure 3.21. In these experiments, the total coupling loss is determined to be 5 dB, in accordance with the 4.8 dB reported by Liu et. al. [188]. For waveguides with a width of 2.2 μm, we measured average losses of 4.10 ± 0.76 dB/m, 3.39 ± 0.86 dB/m, and 4.68 ± 0.73 dB/m for
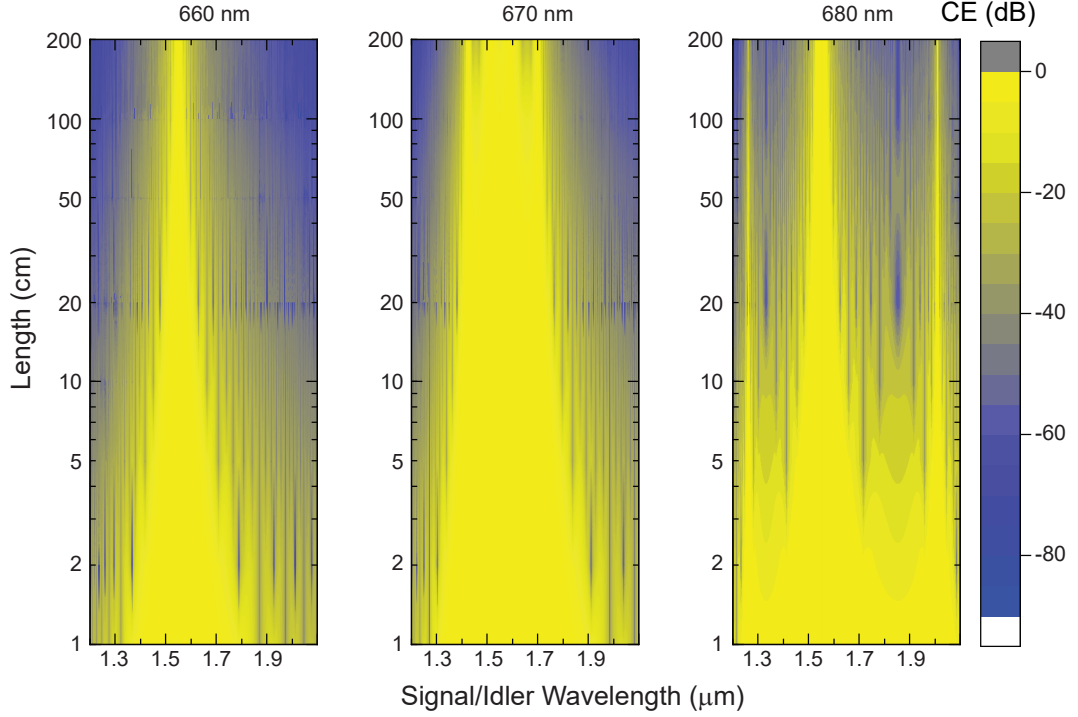
Figure 3.20: (a), (b) and (c) Theoretical normalized CE contour graph for a 1 W of coupled pump power at 1550 nm for various signal wavelengths for various lengths of Si_3N_4 waveguides having the width of 2.2 μm and the heights of 0.66, 0.67 and 0.68 μm, respectively.

waveguide lengths of 0.5 m, 1.0 m, and 1.5 m, respectively. Similarly, for a set of waveguides with a width of 2.5 μm, we measured propagation losses of 1.99 ± 0.32 dB/m, 2.43 ± 0.31 dB/m, 2.95 ± 0.14 dB/m, and 3.99 ± 0.35 dB/m for waveguide lengths of 0.5 m, 1.0 m, 1.5 m, and 2.0 m, respectively.

It should be noted that some large uncertainties and margins of errors are expected from such measurements. Strong fluctuations with the input power are observed, especially in the longer waveguides. It is worth mentioning that the variation in optical loss with the input optical power is not an expected aspect in the Si_3N_4 waveguides. The change in the output power does not form a sublinear trend caused by two-photon absorption. The variation in loss is expected to be due to mode-mixing, which will be covered in the next chapter. Nevertheless, such a strong error in the loss introduces measurement error in the effective length. Another source of error is the constant coupling loss assumption. The performance of the inverse tapers might show a non-ideal response, which can be even input power dependent, and therefore, the coupled pump power might be erroneous as well. Therefore, instead of assuming a constant propagation loss, a loss margin between 2 dB/m and 4.7 dB/m will be investigated in the analysis, as maximum and minimum measured optical loss.

The behavior of waveguides with nominal cross-section 2.2 μm x 0.67 μm and with lengths
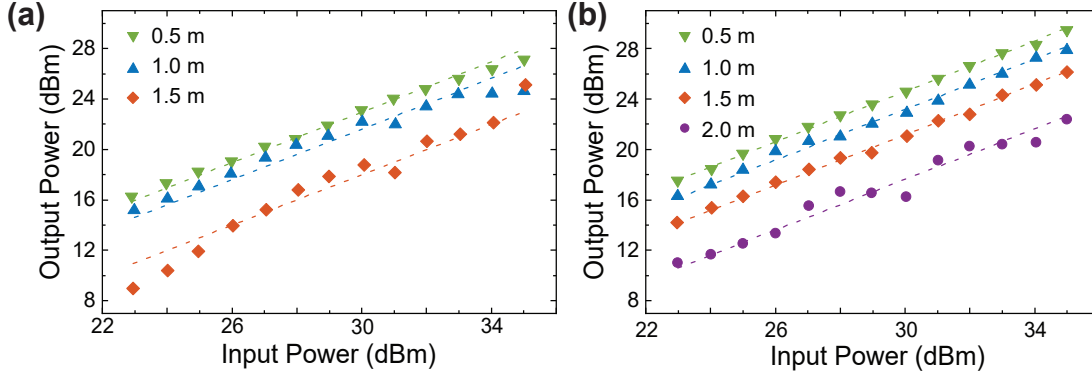
Figure 3.21: Measured output optical power vs input optical power for the loss measurement of silicon nitride waveguides with 2.2 μm x 0.67 μm and 2.5 μm x 0.67 μm cross sections and various waveguide length.

of 0.5 m, 1 m and 1.5 m are experimentally tested. Two pump wavelengths at 1537 nm and 1550 nm are tested with an estimated coupled power of 1.25 W, while the signal is swept on the short wavelength side of the pump with an estimated coupled power of 20 mW.

The CEs at 1550 nm pump wavelength as a function of signal detuning are shown in Figure 3.22(a)-(c) in 0.5 m, 1.0 m and 1.5 m long waveguides, respectively. The 3-dB bandwidth (one-sided) indicated by the black dashed arrow, decreases with length from 48 nm (one-sided) for the 0.5 m long waveguide to 26 nm for the 1.0 m and 15 nm for the 1.5 m long waveguide. The drop in the bandwidth is stronger than the square root of length anticipated from the theory. The possible deviation in the waveguide cross-section plays a more significant role as the waveguide gets longer for the discrepancy.

The experiment is repeated at 1537 nm pump wavelength and the CE values are shown in Figure 3.22(d)-(f) in 0.5 m, 1.0 m and 1.5 m long waveguides, respectively. Although a narrower bandwidth of 38 nm has been observed in the 0.5 m long waveguide, the observed bandwidth is actually broader for 1.0 m and 1.5 m long waveguides due to the cross-section variations. It should be also noted that the strong fluctuations in the CE make the bandwidth measurement intricate.

The average phase-matched values of CE for these three waveguides at 1550 nm were measured to be -15 dB, -6 dB and -7 dB, for the 0.5 m, 1 m and 1.5 m waveguides respectively. While as expected the CE increases when the length is doubled to 1 m, we do not see a further increase with the 1.5 m length waveguide. This behavior could result from the 1.5 m long waveguide having higher propagation losses than the 1 m long one, and/or due to more power being lost to higher-order modes. On the other hand, for 1537 nm, the average phase-matched CE are measured to be -17 dB, -13 dB and -6 dB for 0.5 m, 1.0 m and 1.5 m long waveguides. Due to strong mode-mixing, the CE shows sensitivity to the pump wavelength, which will be investigated in the next chapter. The experiments result in -15 dB CE with 95 nm two-sided 3 dB bandwidth in 0.5 m long waveguides and -6 dB with two-sided 3 dB bandwidth of 52 nm in
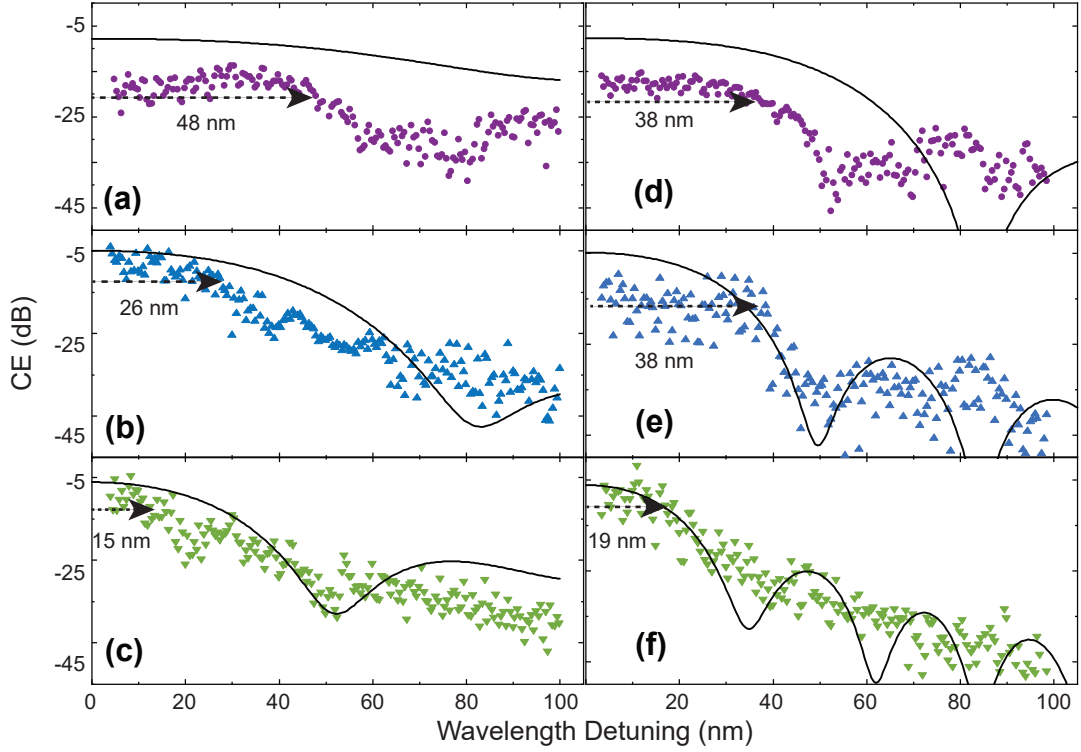
Figure 3.22: CE vs wavelength detuning in 2.2 μm × 0.67 μm cross-section waveguides with lengths of: (a), (b) and (c) 0.5, 1.0 and 1.5 m at 1537 nm pump wavelength; (d), (e) and (f) 0.5, 1.0 and 1.5 m at 1550 nm pump wavelength, respectively. Solid lines show theoretical calculations for the given cross-section and corresponding lengths.

1 m long waveguide are demonstrated.

As the waveguides show strong sensitivity to the variations in the cross-section, various waveguides fabricated as replicas of previously mentioned waveguides are experimented with. Such a vast analysis of waveguides enabled pinpointing a waveguide providing broadband wavelength conversion. In one of the replica waveguides with a cross-section of 2.2 μm × 0.67 μand 1.5 m length, the FWM experiment yields flat wavelength conversion. In Figure 3.23 (a) the superimposed spectra of the pump at 1550 nm, signal light which is swept between 1554 nm to 1660 nm wavelength, and generated idlers are observed.

The waveguide is measured to have a higher loss than previously analyzed waveguides. The extra 6 dB loss can be due to a coupling loss and/or propagation loss making it hard to estimate the exact pump power and effective length. The corresponding experimental CEs together with the theoretical CE values for heights of 670 nm, 669.5 nm and 668 nm are shown in Figure 3.23 (b) for a waveguide with 6 dB propagation loss and 30 dB coupled pump power. Such high optical loss limited the phase-matched CE to around -11 dB. In terms of bandwidth, on the other hand, the response remains relatively flat within the wavelength range investigated. The CE vs wavelength detuning trend shows similarity with both theoretical fits of the heights
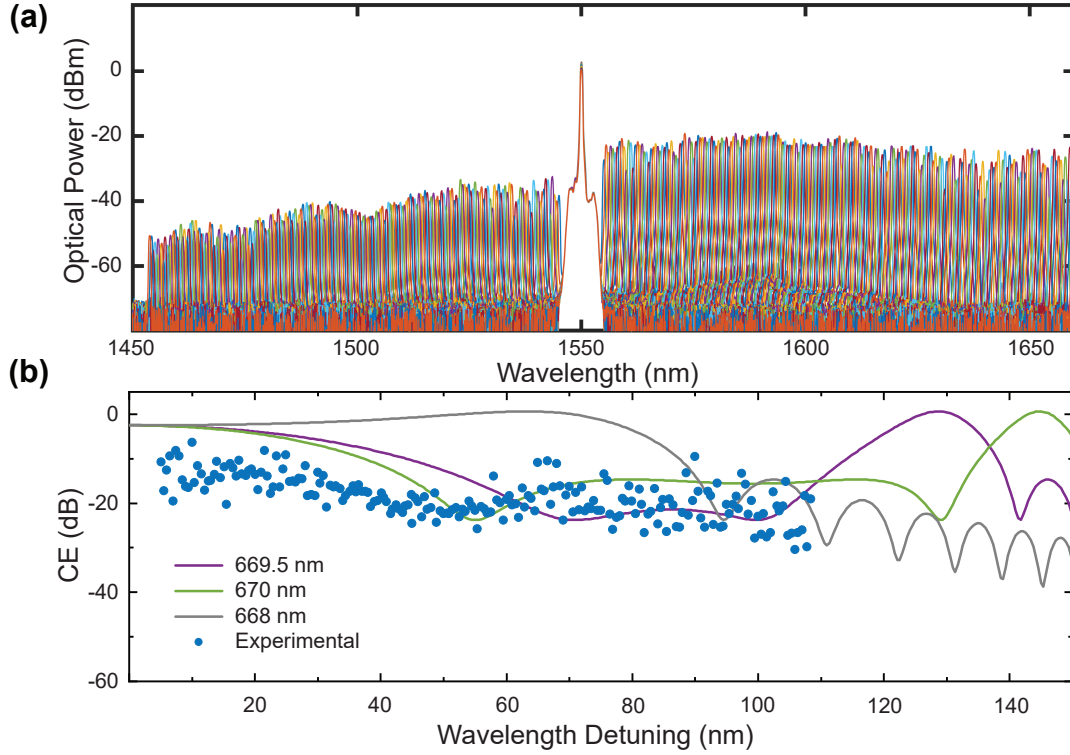
Figure 3.23: (a) Superimposed optical spectra of four-wave-mixing for a pump wavelength of 1550 nm and the signal swept through 1554 nm to 1650 nm (b) CE vs wavelength detuning in 2.2 µm × 0.67 µm cross-section waveguide taken from a different position of the wafer with a length of 1.5 m. Solid lines illustrate the theoretical expectation for the heights of 668 nm, 669.5 nm and 670 nm

of 669.5 nm and 670 nm. Both theoretical plots indicate the merger of the distant phase-matched lobe resulting in a flat CE trend. The two-sided 3 dB bandwidth of 60 nm is expected due to a slight difference from the 668 nm height, at which zero dispersion at 1550 nm is obtained. However, the merger of the distant phase-matched lobe extends the two-sided 20 dB bandwidth further than the experimentally measured 205 nm, which can even extend further than 250 nm according to the theoretical calculations for 669.5 nm and 670 nm.

3.4.4 Power scaling and parametric gain formation

To enhance the characterization of CE trends concerning waveguide lengths, waveguides with a cross-section of 2.5 µm x 0.67 µm were tested, evaluating four different lengths (0.5 m, 1 m, 1.5 m, and 2 m). Despite slight detuning from optimal dispersion for broadband conversion, we present the results for a fixed pump-signal detuning of 1.5 nm in Figure 3.24(a). While the CEs generally align with the trend of the pump power squared (illustrated by the dashed guidelines), notable data fluctuations are apparent. At an estimated coupled pump power of 32 dBm in the 2 m long waveguide, a CE of approximately 2.9 dB is achieved. In addition, the
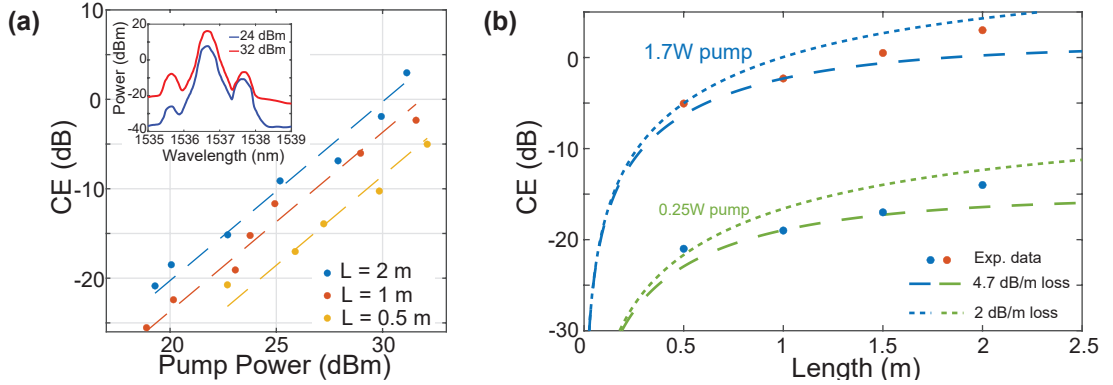
Figure 3.24: Experimental CE (dots) and guides for the eye (dashed lines) as a function of estimated coupled pump power for the waveguide length of 0.5, 1, and 1.5 m. (b) The experimental and theoretical CE for 0.25 and 1.7 W of estimated coupled pump power together with simulated CE vs length curves for 2 dB/m and 4.7 dB/m propagation loss.

3.9 dB observed parametric gain is in accordance with the observed CE. The spectra at 24 dBm coupled power and 32 dBm coupled power are shown in the inset. These waveguides typically yield higher CE than 2.2 μm wide waveguides possibly due to the lower propagation loss. The maximum CE reached in the waveguides are -6 dB, -4 dB, 0.5 dB and 2.9 dB, for the increasing length.

By conducting a linear fit for waveguides of lengths 0.5 m, 1 m, 1.5 m, and 2 m and assuming an average propagation loss of 4 dB/m, we derive a nonlinear parameter, γ, which falls within the range of 0.6-0.8 $W^{-1}m^{-1}$. This range aligns with the A_{eff} values obtained from simulated data $n_2 = 2.4 \times 10^{-19} m^2 W^{-1}$, resulting in a value of 0.75 $W^{-1}m^{-1}$. The observed variations in the measured data may stem from fluctuations in propagation loss and coupling loss among different waveguides, as well as the challenge of precisely determining the effective pump power, which could be lower than the coupled power due to the excitation of higher-order modes.

In an effort to determine the potential operational limits, the CE is presented as a function of waveguide length for both high (1.7W) and low (0.25 W) estimated coupled pump powers. This data is visually represented in Figure 3.24(b). The values for propagation loss have been adapted to align with the experimentally measured results. Two important findings emerge from this analysis: Firstly, it's consistent with expectations that changes in the propagation loss have a more significant impact as the waveguide length increases. Secondly, the effective loss values fall within the anticipated range (typically ranging from 2 to 4.7 dB/m), although it's worth noting that the 1 m and 1.5 m waveguides display slightly reduced performance.

Extending the effective length of the waveguides indeed leads to improved efficiency. According to theory, extending the effective length results in an increase in CE, scales with the square of L_{eff}, and bandwidth reduction, scales with the inverse quadratic root of the L_{eff} around ZDW. Although such a trend is observed by the experimental demonstrations, practical

implementation encounters several hurdles.

First, even a slight error in waveguide height compared to the designed one has a disproportionate impact on bandwidth. This unpredictability makes it challenging to achieve reliable broadband conversion in such waveguides. As illustrated in Figure 3.23, a mere 1.5 nm difference in height can cause the 3 dB bandwidth to vary significantly, ranging from 155 nm to 66 nm. Such change in the dispersion characterization magnifies with the effective length.

Second, optical loss in longer waveguides displays substantial fluctuations. Some replicated waveguides exceeding one meter in length fail to transmit light altogether. Reliable low-loss fabrication of longer waveguides remains challenging. This elevated propagation loss in longer waveguides, which is also observed by Liu et. al. [188], diminishes the significance of increasing the length.

Third, even in waveguides with low propagation loss, the average phase-matched CE falls below theoretical expectations. This deviation is likely attributed to higher-order mode excitation. Light scattered into higher-order modes typically exhibits lower nonlinearity due to a decreased nonlinear parameter. Moreover, as intermodal FWM has a substantial phase mismatch the drop in CE becomes more significant.

Lastly, optical power fluctuations along the signal and idler wavelengths are substantial. These fluctuations can lead to more than 10 dB variations in CE, which become even more pronounced as the waveguide length increases. In the upcoming chapter, the source of optical fluctuations, higher-order mode excitation, and the other parameters affecting the CE will be investigated.

4 Mode-Mixing and Efficiency Factors in Silicon Nitride Waveguides

In the previous chapter, the exploration of parametric wavelength conversion encompassed efficiency and bandwidth, the utilization of polarization for operation in different bands, and the generation of sources through distant wavelength conversion. However, practical experimentation revealed discrepancies compared to theoretical analyses, primarily due to the sensitivity of waveguide dispersion characteristics related to the waveguide's cross-section and variations in propagation loss arising from fabrication processes. Despite these insights, the persistent and substantial fluctuations in CE observed in long low-loss waveguides and the reduction in average CE pose ongoing challenges for comprehension.

This chapter shifts the focus towards other influential factors impacting average CE and optical power fluctuations, with particular emphasis on higher-order modes and mode mixing that can arise in meter-long waveguides. Our investigation aims to uncover the sources of higher-order mode excitation and employs temperature tuning to fine-tune mode interference and alleviate idler power fluctuations.

4.1   Efficiency Analysis

Theoretical calculations were conducted under the assumption of a nonlinear parameter independent of pump frequency and mode-mismatch of the pump, signal, and idler. In addition,the change in propagation loss with the wavelength detuning is neglected . Nevertheless, these assumptions may not always apply, particularly when dealing with significantly different pump frequencies and wavelength detunings. The confinement of the waveguides depends not only on the waveguide dimensions but also the wavelength of the lights participating in the nonlinear interaction. Additionally, the extent of the optical mode in the cladding plays a crucial role for nonlinearity and loss. This section is dedicated to exploring these variables and their impact on CE, especially. Furthermore, the analysis will delve into the multimode characteristics of the waveguides and their associated effects.

The analyzed buried channel Si_3N_4 waveguides are cladded with SiO_2 layer deposited on a
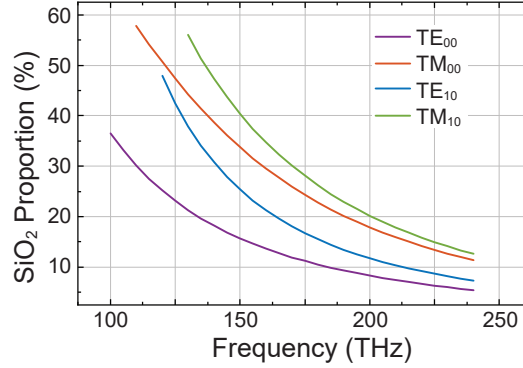
Figure 4.1: The proportion of the optical power that resides in the silica cladding for various optical frequencies and for TE_{00}, TE_{10}, TM_{00} and TM_{10} optical modes in 2.2 μm × 0.67 μm Si_3N_4 waveguide.

Si substrate. Although Si_3N_4 has a wide transparency range covering from mid-IR to visible [230], the optical mode leaking into the cladding can cause an excess optical loss in the system. The SiO_2 layer introduces an increasing amount of infrared absorption loss, which becomes significant for wavelength longer than 2.5 μm and longer wavelengths [231]. Moreover, SiO_2 is sensitive to the humidity introducing water absorption around 1.4 μm and beyond 2.7 μm [72], [232]. This loss depends on the portion of the light propagating through the cladding.

To estimate the optical loss induced by the SiO_2 cladding, the optical modes in 2.2 μm × 0.67 μm Si_3N_4 waveguide are simulated and integrated optical intensity in the cladding over the total is presented in Figure 4.1 for TE_{00}, TE_{10}, TM_{00} and TM_{10} modes. It can be observed that more portion of light propagates in the cladding for the low frequencies (i.e. long wavelengths). This effect is even more pronounced as the higher-order modes are excited in the waveguide for all polarization modes. The extinction coefficient of SiO_2 can go up to roughly 10 times higher as the wavelength approaches 3 μm [233]. Therefore, the propagation in the cladding is a substantial source of optical loss.

One of the strong factors leading to a lower CE in distant wavelength conversion to mid-infrared might be the excessive loss in the cladding for the idler (Figure 3.12). The generated idler experiencing more optical loss through the waveguide also explains the broader bandwidth measured in the distant band. Additionally, the strong drop in the CE beyond 2.65 μm wavelength, shown in Figure 3.12, might be due to the increasing propagation loss in the cladding with the longer wavelengths.

Another source of the drop in CE is the increasing effective area in the waveguides at longer pump wavelengths. The intensity of the mode drops as the mode expands to a larger area resulting in reduced nonlinear interactions in the waveguide. The effective areas for TE_{00}, TE_{10}, TM_{00}, and TM_{10} modes in 2.2 μm × 0.67 μm Si_3N_4 waveguide are shown in 4.2. As it can be seen in Equation (2.4), the electric field can have steeper changes at high frequencies in the transverse direction. On the other hand, at low frequencies, the change in the electric
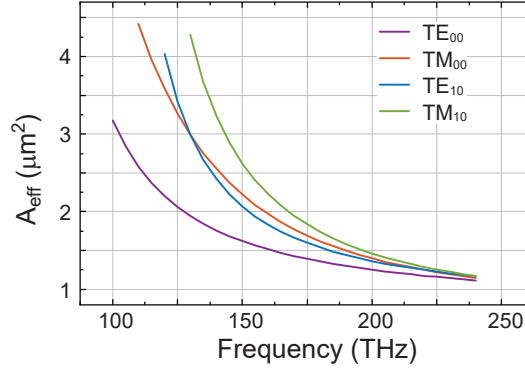
Figure 4.2: The effective area (A_{eff}) for various optical pump frequencies and for TE_{00}, TE_{10}, TM_{00} and TM_{10} optical modes in 2.2 μm × 0.67 μm Si_3N_4 waveguide.

field in the transverse direction is relatively low leading to a weaker confinement. Therefore, the effective area increases drastically at the lower frequencies (longer wavelengths). In addition, excitation to the higher-order modes further reduces the expected CE by increasing the effective area which is especially more pronounced at the longer wavelengths. It should be noted that the nonlinear index, n_2 is also wavelength dependent, which can affect the CE.

The strong asymmetry of the waveguides in height and width and the significant refractive index difference between Si_3N_4 and SiO_2 create a strong discrepancy in the mode shape of the TE and TM modes. Since the height is the limiting dimension of the waveguide, in the TM mode electric field is normal to the boundary whereas in the TE field electric field is tangential. For TM polarization, Maxwell boundary conditions enforce the normal component of the displacement field to be continuous resulting in a higher electric field in SiO_2 at the boundary as opposed to TE polarization where the electric field is continuous. Therefore, a larger portion of the light propagates in the cladding causing a higher effective area in TM polarization which can be seen in both Figures 4.1 and 4.2.

The description of the effective area assumes the optical modes are identical for the pump, signal and idler. However, this condition might no longer hold at high-frequency detunings. Moreover, as the nonlinearity in the cladding is much weaker than the core region, the optical mode overlap in the cladding does not lead to nonlinear interaction. Consequently, the CE of the process deviates from the theoretical calculations under the assumption that all the pump power contributes to the nonlinear process and the contribution is frequency detuning independent.

To quantify such an effect, a nonlinear overlap factor, ξ, is defined where

$$\xi = \frac{\iint \chi^{(3)} \psi_1^* \psi_2^* \psi_3 \psi_4 \, dx \, dy}{\sqrt{\iint \psi_1^* \psi_1 \, dx \, dy \iint \psi_2^* \psi_2 \, dx \, dy \iint \psi_3^* \psi_3 \, dx \, dy \iint \psi_4^* \psi_4 \, dx \, dy}} A_{eff} \quad (4.1)$$
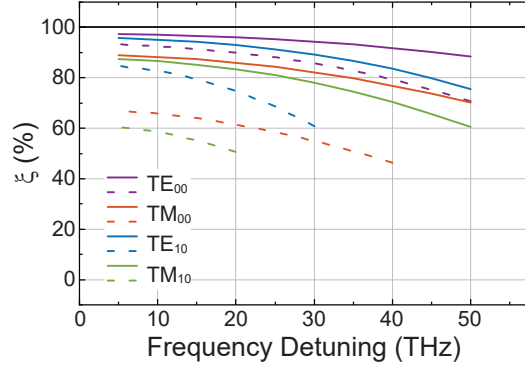
Figure 4.3: The nonlinear overlap factor (ξ) for various optical pump frequencies and for TE_{00}, TE_{10}, TM_{00} and TM_{10} optical modes in 2.2 μm × 0.67 μm Si_3N_4 waveguide. Solid lines show the values at 190 THz optical frequency whereas dashed lines show values at 150 THz.

In Figure 4.3, the nonlinear overlap factor with frequency detuning of signal/idler with the pump is shown for 190 and 150 THz of pump frequency and for TE_{00}, TE_{10}, TM_{00}, and TM_{10} modes in 2.2 μm × 0.67 μm Si_3N_4 waveguide. At the 150 THz pump frequency (2 μm wavelength), not only the optical mode is confined to a larger area, but also a lower nonlinear overlap factor is obtained. The lower nonlinear interaction is mainly due to strong leakage of the mode to the cladding at the low-frequency detunings. As the frequency detuning increases the mode mismatch between the pump, signal and idler also reduces the nonlinear overlap factor resulting in a lower CE. Therefore, the deviation in the CE becomes significant for the distant FWM at the pump wavelengths around 2 μm. It is worth mentioning that any excitation to higher-order modes or operating in TM polarization further drops the nonlinear overlap factor and thus the effective γ.

The analysis of this section investigates the factors that are not included in the theoretical calculation which can explain the measured CE differences observed in the experimental analysis. For the broadband CE around 2 μm, the nonlinear parameter is lower due to the lower nonlinear parameter calculated to be around 0.4 $W^{-1}m^{-1}$ according to the simulations. The drop in the nonlinear parameter is due to longer wavelength, larger effective area and lower nonlinear overlap factor. Such a decrease in the nonlinear parameter and the pump power explains the observed CE around -30 dB in fundamental TE mode.

For broadband conversion in the L-band for TM polarization, the nonlinear parameter is calculated to be around 0.5 $W^{-1}m^{-1}$ in the L band and 0.2 $W^{-1}m^{-1}$ around 2 μm wavelength including these effects. Such low nonlinearity hindered the generation of an idler with a stronger optical power than the amplified spontaneous emission noise of the thulium-doped fiber amplifier. Moreover, the lower CE in the fundamental TM mode compared to the TE case can be understood through the drop in the nonlinear parameter also considering the drop of coupled power due to non-optimized inverse taper couplers in TM.

In the case of distant FWM towards the mid-infrared in the fundamental TE mode, an ap-
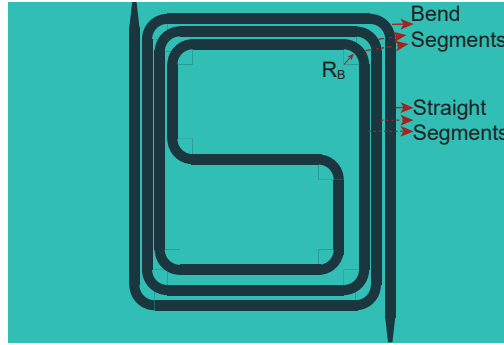
Figure 4.4: Illustration of the spiral waveguide on chip. R_B represents the bend radius.

proximately 10 dB lower CE is observed compared to wavelength conversion around the 2 μm pump wavelength. This lower CE results from a reduced nonlinear overlap factor, causing around a 6 dB decrease in efficiency for wavelengths near μm. The additional disparity can be attributed to the elevated optical loss in the cladding, especially beyond 2.65 μm.

None of the aforementioned factors can account for the lower parametric wavelength CE in the fundamental TE mode around the pump wavelength. Nor the optical power fluctuations can be addressed with the fundamental mode operation. The following section will delve into the origin of the higher-order mode excitation as well as the effect of the bend dimensions.

4.2   The origin of the higher-order modes and mode-mixing

The integration of the meter-long waveguides onto a chip area of a couple of mm^2 poses a challenge. The long waveguides are typically folded into spirals or meanders. The spirals can be formed by constant change in the bend radii of the waveguide (known as archimedean spiral) [189] or merged straight and bend segments forming a spiral as illustrated in Figure 4.4. The number and the size of the segments change with the length of the waveguide and the footprint area on the chip. The compact integration of the waveguide requires hundreds of bend segments for such a design whose radius of curvature, referred to as bend radius, R_B, is limited with the design.

The 2.2 μm x 0.67 μm cross-section waveguide supports 3 TE and 3 TM modes at 1550 nm wavelength. However, as the waveguides are equipped with an inverse taper coupler optimized for fundamental TE mode, the fundamental TE mode propagation in the waveguide is assumed. Without a source of scattering, the optical modes maintain their order while propagating through the waveguide. However, the bends cause a change in the shape of the wavefront such that some portion of the fundamental mode light overlaps with higher-order modes. Therefore, the light can scatter into the higher-order modes due to the presence of many straight-to-bend transitions. and excites them proportional to the bend curvature.
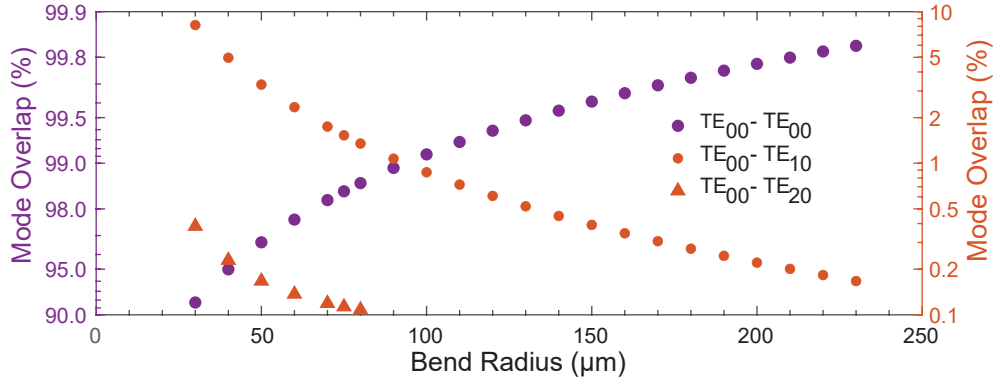
Figure 4.5: Intensity mode overlap factor between fundamental mode in the straight segment and fundamental mode (left axis) and TE_{10} and TE_{20} modes (right axis) in the bend segment .

Figure 4.5 demonstrates the simulated percentage of the intensity mode overlap factor, Γ, of the fundamental mode in the straight segment with the fundamental mode (left axis) and with the TE_{10} and TE_{20} modes (right axis) in the bend segments. The calculation of the Γ is presented in Equation (2.7). Although the intensity overlap integral between a straight and bent section of the waveguide is only 0.15% for the 230 µm bend radius between TE_{00} and TE_{10}, excitation of higher order modes can build up since meter-long waveguides can have more than 400 bend segments. It can be seen that as the bend radius decreases below 100 µm, the intensity overlap integral increases above 1% while it also becomes possible to excite a remarkable amount of TE_{20} mode at each transition.

As the higher-order modes build up through the waveguide, the straight-to-bend transitions become a multimode-multimode interface. Together with the overlap the relative phase of the modes also becomes significant as the overlap of the different modes can interfere constructively or destructively depending on the relative phase difference. In such long waveguides, the phase change is enormous with the change in the wavelength causing strong fluctuations in the excited modes. Consequently, the excitation of the higher order modes causes strong interference of the modes, known as mode-mixing.

The optical TE intensity mode profiles together with the corresponding effective refractive indices are presented in Figure 4.6(a), (b) and (c). The interference through the waveguide does not cause any fluctuation of the optical power as the modes are orthogonal to each other and the total optical power is equal to the sum of optical powers at each optical mode. However, the interference leads to power fluctuations when they are coupled out from to waveguide to a single-mode optical system. As the propagation constants are significantly wavelength-dependent, such interference can be very sensitive to the wavelength. Two junctions in the system causes mode-mixing: the interference at the output coupling to the single-mode platform and the transitions in straight-to-bend and bend-to-straight transitions.

A model is developed to visualize the interference at the outcoupling of the waveguide. In this model, the higher-order modes are launched at the half-length of the straight waveguide, so
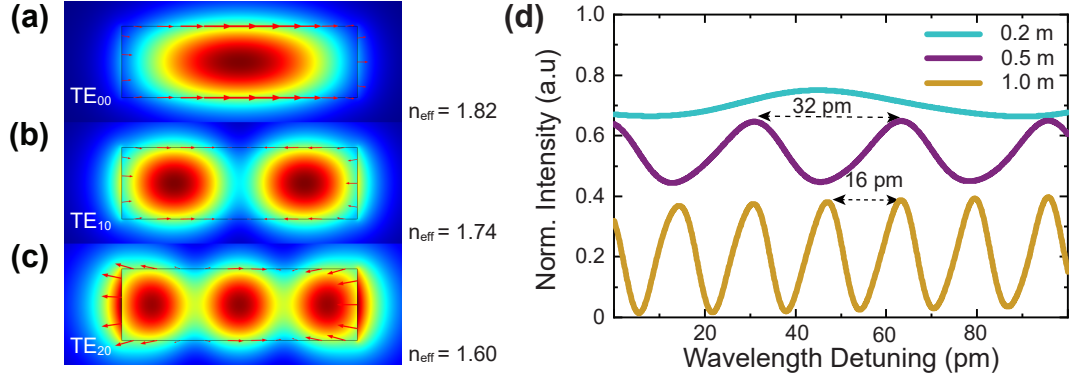
Figure 4.6: The optical mode profiles of (a), (b) and (c) TE_{00}, TE_{10} and TE_{20} with the corresponding effective indices, respectively. (d) Normalized intensity vs wavelength detuning for the model estimates the interference at the output coupling in 0.2, 1.0 and 2.0 m long waveguides.

that modes propagate through the waveguide without the interference effect of bends. The half-length is chosen to be an average point for the generation of higher-order modes. As the interference in the bends is not desired in this model, the optical intensity of higher order modes is chosen to be linearly scaled with the length of the waveguide. Then, the light is coupled out to a single-mode optical system.

$$A_T(L) = \Gamma_{m1} A_{m1}(L) e^{\frac{2\pi n_{\text{eff},1}}{\lambda} \frac{L}{2}} + \Gamma_{m2} A_{m2}(L) e^{\frac{2\pi n_{\text{eff},2}}{\lambda} \frac{L}{2}} + \Gamma_{m3} A_{m3}(L) e^{\frac{2\pi n_{\text{eff},3}}{\lambda} \frac{L}{2}} \qquad (4.2)$$

where Γ_1, Γ_2, and Γ_3 are arbitrary mode overlap factors to the output optical mode of TE_{00}, TE_{10}, and TE_{20} waveguide modes, respectively. A_{m1}, A_{m2}, and A_{m3} are the scaled mode field amplitude and $n_{\text{eff},1}$, $n_{\text{eff},2}$, and $n_{\text{eff},3}$ are the effective refractive indices of TE_{00}, TE_{10}, and TE_{20} waveguide modes, respectively. A_T is the scaled mode field amplitude of the transmitted field. A_{m2} and A_{m3} scale with $\sqrt{L}$ whereas A_{m1} decreases with the length to maintain constant $|A_{m1}|^2 + |A_{m2}|^2 + |A_{m3}|^2$.

The interference patterns are shown in Figure 4.6 for 0.2, 1.0 and 2.0 m long waveguides. The intensity profiles (in arbitrary units) are shifted on the scale for better visibility. It can be seen that the change in the optical power with the wavelength detuning (the relative change compared to the initial position) is less pronounced for the 0.2 m long waveguide with a wavelength detuning period of 80 pm. However, the effect becomes more significant with the change of 32 pm and 16 pm as the waveguide length reaches 0.5 m and 1.0 m. It should be noted that such representation is far from perfect. The generation of higher-order mode can occur at each bend segment throughout the transitions and each generated mode can be affected the external factors such as temperature and the deviation in the waveguide dimensions.

To estimate the interference at the straight-to-bend transition, a model is assumed where
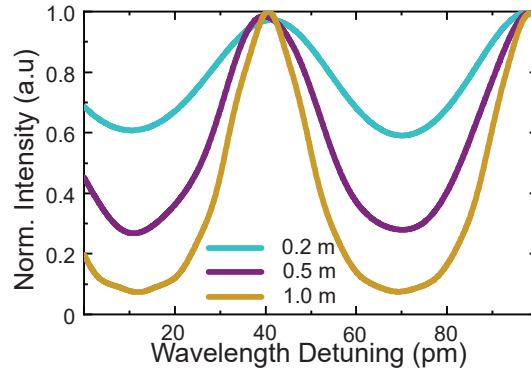
Figure 4.7: Normalized intensity vs wavelength detuning for the model estimates the interference at the bends in 0.2, 0.5 and 1.0 m long waveguides.

the excitation of the higher-order mode occurs once in 5 mm and neglects the length of the bend segment. The model also allows conversion back to the fundamental mode after being converted to the higher-order modes. The overlap values are taken according to the numbers presented in Figure 4.5 at 230 μm bend radius. The transmitted field is calculated with Equation (4.2). The interference patterns are presented in Figure 4.7. The constant length assumption before the scattering causes an interferometer-like pattern with the wavelength detuning where the light can make constructive interference at each scattering point. However, in the actual waveguides, the straight-to-bend transitions occur at distances changing from 3 mm to 5 mm as the length of the straight segments are not constant as can be seen in Figure 4.4. The length of the bend segments in the order of hundred μm can also introduce another scattering source. In addition, temperature and waveguide cross-section variations are still impacting the mode-mixing.

For the waveguides used in this thesis, there are hundreds of bend segments where the light can scatter to the higher-order at both straight-to-bend and bend-to-straight transitions. A 2 m waveguide having more than 440 bends at 230 μbend radius can potentially convert all the light to the higher order modes. Such mode-mixing behavior potentially explains the substantial fluctuations in the optical power with wavelength.

To characterize this, another experiment is conducted by employing a laser with a piezoelectric controller for precise tuning of the wavelength over a small range. The wavelength is gradually detuned up to 150 pm towards longer wavelengths from the center wavelength using an electrical triangular signal waveform and coupled to a waveguide. At the output the light is sent to a photodetector and measured in synchronization with the input signal waveform. In this method, waveguides with a cross-section of 2.2 μm x 0.67 μm and lengths of 0.5 m and 1.0 m are tested. The changes in transmitted optical power, relative to the maximum, are plotted in Figure 4.8(a) and (b) for the 0.5 m and 1.0 m waveguide, respectively. It was observed that the measured optical power can decrease by up to 90% in situations where the modes interfere destructively.

(a)

(b)

Figure 4.8: The normalized optical power vs. wavelength shift of the piezo-controlled laser for 0.5 m and 1.0 m long waveguides with 2.2 μm x 0.67 μm cross-section

The transmission in both waveguides has sinusoidal fluctuation patterns with different periods. In the 0.5 m waveguide, strong fluctuations with periods of around 60 to 90 pm, moderate fluctuations of with a period around 35 nm and dense ($\approx$ 1 pm) fluctuations with smaller magnitudes are observed. Although the introduced models cannot exactly predict the chaotic response of the waveguides, the fluctuation periods are partially in agreement with the models predicting the interference at the bends and the interference at the output coupling. The small dense fluctuations can be understood through Fabry-Perot interference with the period $\Lambda = c/2nL$, which is found to be 1.2 pm for the 0.5 m waveguide for the fundamental TE mode. As predicted by the model, in the 1 m long waveguide, the strong fluctuations due to mode-mixing in the bends maintain the same period in the range of 60 - 90 nm whereas the fluctuations due to output coupling have a reduced period of 24 pm.

The significant variation in optical power due to slight wavelength detuning at the pm level leads to alterations in both signal and idler optical power, causing fluctuations in CE. These fluctuations become more pronounced when many bends are employed, which is necessary for the compact integration of meter-long waveguides. In the upcoming section, The impact of higher-order modes and mode-mixing on FWM CE will be examined.

4.3 Effect of Mode-Mixing on FWM in Spiral Silicon Nitride Waveguides

The previous section demonstrated the existence of the higher-order modes in the waveguides and their scattering. This section will focus on their effect on the CE.

A strong factor affecting the CE is the excited optical modes in the waveguide. As explained previously the higher-order modes typically have larger effective areas resulting in lower nonlinearity. However, the excitation of the higher-order modes can even result in a further drop in the CE if the modes are strongly phase-mismatched. In Figure 4.9, the theoretically calculated CE for 0.1 W pump power and 0.5 m long waveguides for the cross-section of 2.2 μm
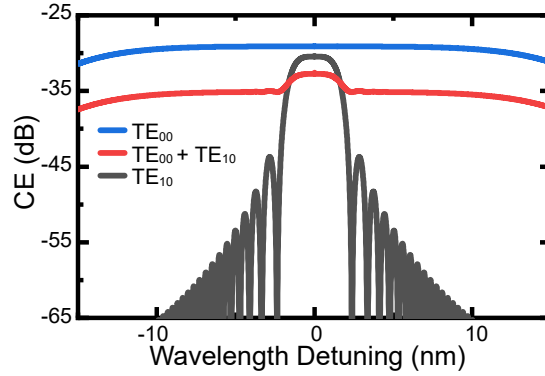
Figure 4.9: The CE vs wavelength detuning for all of the optical power coupled into TE_{00} mode; half of the optical power is coupled into TE_{00} mode and the other half if coupled into the TE_{10} mode; and all of the optical power coupled into TE_{10} mode

$\times$ 0.67 µm are presented. Three cases are investigated: the optical power is completely excited in the fundamental TE mode, the optical power is completely excited in TE_{10} mode, and the optical power is coupled to both modes equally. The calculation assumes all the converted optical power can be collected constructively, i.e. disregarding interference. Comparing the completely confined in the fundamental TE mode and in TE_{10} mode, it can be seen that the phase-matched CE is lower by approximately 2 dB due to a larger effective area as expected. The bandwidth is narrower compared to the fundamental mode as the waveguide is not engineered to have low GVD in the C-band.

When the optical power is shared between the two optical modes the phase-matched CE is found to be even lower. As the CE scales with the square of the pump power, a partition of the light among different modes causes a further drop in the efficiency as in the case of the interested waveguide due to the high intermodal phase-mismatch. Moreover, the bandwidth characteristics are also affected by the existence of the higher-order modes, which can limit the measured 3 dB bandwidth according to the dispersion characteristics of the higher-order modes. Such a response can explain the CE cs wavelength detuning trend that was observed in the 3.1 µm wide waveguide shown in Figure 3.18. The higher-order modes can cause a strong drop beyond a small wavelength detunings. The drop in the phase-matched CE is even more pronounced as the excited number of modes increases. The theoretical analysis anticipates elevated higher mode-excitation with longer waveguide lengths employing more bend segments and with reduced bend radii. In order to investigate this aspect, CE vs wavelength detuning experiments are conducted in another set of Si_3N_4 spiral waveguides having a cross-section of 2.0 µm x 0.8 µm. Although this cross-section is not intended to give the largest bandwidth, these waveguides provide the availability of different bend radii (75 µm and 230 µm) and lengths (7.4, 16, 22, and 32 cm), as shown in Table 4.1.

The CE vs wavelength detuning is experimentally tested in these waveguides and presented in Figure 4.10, together with theoretical fit according to Equation (2.28). The square root

Waveguide name	ROC (µm)	Length (cm)	Reduced chi-square of the fit (dB)
Waveguide I	230	22	1.12
Waveguide II	230	32	1.42
Waveguide III	75	7.4	2.18
Waveguide IV	75	16	3.05
Waveguide V	75	32	4.78

Table 4.1: Tabulation of length and bend radii for one-side tapered Si_3N_4 waveguides used in this work together with the reduced-chi square of theoretical fit according to Equation (2.28).

of the reduced chi-square of the fit is extracted as a figure of merit for the fluctuations and presented in Table 4.1. One can clearly observe that the experimental measurements fit well in the case of the 230 µm bend radius and the 22 and 32 cm waveguides (Figure 4.10(a),(b)), compared to the CE fits in meter-long ones, due to lower excitation to the higher order modes in shorter waveguides. A lower square root of chi-square of 1.12 dB in the 22 cm long waveguide compared to the 32 cm long waveguide with 1.42 dB is obtained. To confirm the effect of bend radii, the data for 75 µm and with lengths of 7.4, 16, and 32 cm, is shown in Figure 4.10(c)-(e), respectively. The fluctuations in CE are more pronounced in these waveguides due to lower bend radii. The square root of the chi-square rises from 2.18 dB to 3.05 and 4.78 dB as the length of the waveguide increases from 7.4 to 16 and 32 cm. In the 32 cm long waveguide, the fit looks arbitrary as the fluctuations wash out the dispersion characteristics.

The bandwidth of wavelength conversion naturally decreases in longer waveguides, aligning with theoretical expectations. Furthermore, when Waveguide II and Waveguide V are compared, the phase-matched CE in Waveguide V is approximately 3 dB lower than that in Waveguide II. In a similar manner, Waveguide I is expected to yield a phase-matched CE roughly 9 dB higher than Waveguide IV. This significant increase in CE cannot be explained solely due to the longer length (22 cm compared to 16 cm), which corresponds to a 3 dB enhancement. Thus, this study underscores the reduction in CE resulting from higher-order mode excitation.

4.4 Temperature Tuning Analysis of FWM in Silicon Nitride Waveguides

As demonstrated before, the primary cause of CE fluctuations is mode-mixing, which is susceptible to refractive index changes. Even a small alteration in the refractive indices of these modes can have a significant impact on CE in meter-long spirals featuring numerous straight-to-bend transitions. One approach to adjust the refractive indices and consequently the phase mismatch between modes is to modify the temperature profile. Although slight adjustments in the temperature profile only lead to minor changes in the refractive index differences between modes, they build up significant phase differences through meter-long waveguides.
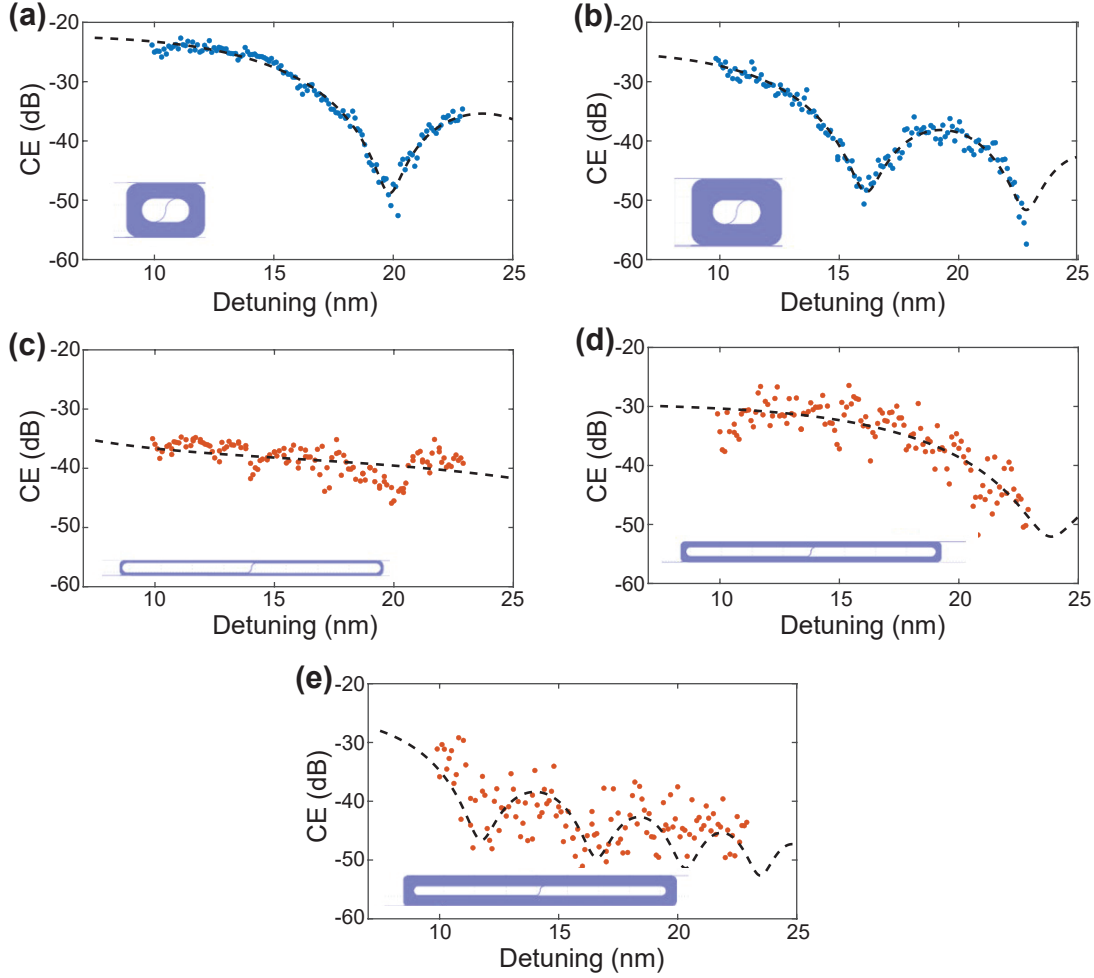
Figure 4.10: (a), (b), (c), (d) and (e) Experimental CE (dots) and Fitted CE (dashed lines) in the one-side tapered waveguides I, II, III, IV and V, respectively. The shape of the corresponding spiral waveguide has been depicted in the lower left corner of each graph.

The coupling loss in the waveguides causes a portion of the light to be reflected, absorbed, or scattered, which eventually gets absorbed through the trap states or the substrate. Therefore, a significant portion of the lost optical power is converted to heat, causing elevation of the temperature. Additionally, as the heat source is mainly localized at the input coupler of the waveguide, it generates a temperature gradient through the chip, causing complex variations in the interference at the bends. The CE fluctuations seen with the pump power in Figure 3.24 can be attributed to such behavior.

To investigate the effect of temperature, the FWM experiment is repeated with the chip positioned on a stage integrated with a heatsink and a Peltier controller. The power scaling experiment, as in Figure 3.24, is repeated in 2.5 µm x 0.67 µm cross-section waveguide at a fixed temperature set at 35° C. In Figure 4.11(a) the CE and gain values are presented for various pump powers, the dashed lines represent the best and worst cases of CE and signal gain fitted
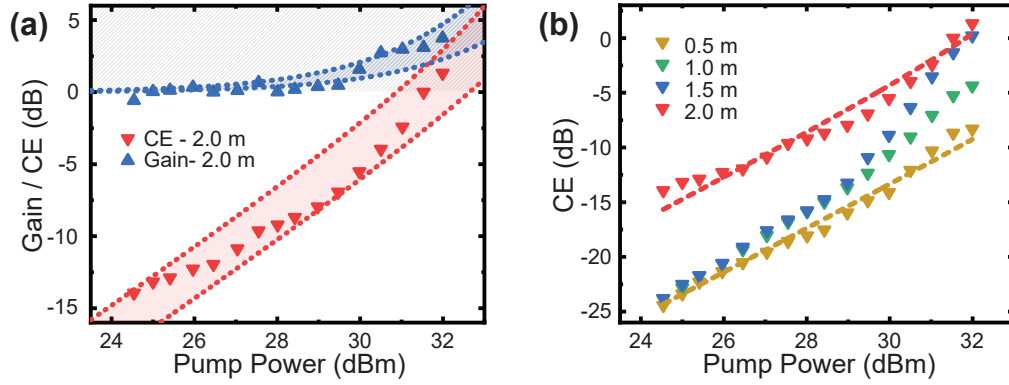
Figure 4.11: (a) Experimental CE (red triangles) and signal gain (blue triangles) and corresponding best and worst guide to eye lines (dashed lines) as a function of estimated coupled pump power in 2.0 m long waveguide. (b) Experimental CE (triangles) and guide to eye fit lines (dashed lines) for the waveguide length of 0.5, 1, 1.5 and 2.0 m with the cross-section of 2.5 μm x 0.67 μm after the integration of a heat sink and Peltier controller

with the same parameters. The gain is calculated according to the transmitted signal power in the absence of the pump. The CE values are in agreement with the best case line at the low pump powers. However, as the pump power is gradually increased the trend approaches the worst case line around 28 to 30 dBm of pump power. If the pump power is further increased, the CE trend returns to aligning with the best case line around 32 dBm pump power. Similarly, the gain also makes a transition from worst to best case line as the pump power is gradually increased from 28 dBm to 32 dBm. This behavior can be understood via temperature gradient on the chip with the coupling losses serving as a heat source. The intermodal interference in the straight-to-bend transitions can lead to more constructive or destructive interference depending on the temperature of the transitions. As the same trend is also observed in the gain in addition to the CE, more constructive interferences to the fundamental mode of the pump in the transitions can be the underlying factor. A 1.6 dB CE is measured at 32 dBm pump power with this method which can go up to around 4 dB for the best case line. Notably, the CE fluctuations are observed to be more limited with the pump power and more stable over time when using a temperature controller, allowing observation of slight changes in the CE trend rather than strong fluctuations.

The measured CE obtained in 0.5 m, 1 m and 2 m long waveguides are presented in Fig 4.11(b). The CE shows good agreement with the square of the pump power in the 0.5 m long waveguide with a minimal amount of fluctuations. However, deviations from the pump power square are observed for 1 m and 1.5 m long waveguides, similar to what was observed in the 2 m long waveguide. The deviation is even more pronounced in the 1.5 m due to more significant excitation to the higher-order modes.

To investigate the impact of temperature on broadband FWM wavelength detuning, the 1 m long waveguide with a cross-section of 2.2 μm x 0.67 μm is selected as a representative example. The experiment is initiated by assessing CE depending on temperature and pump power while
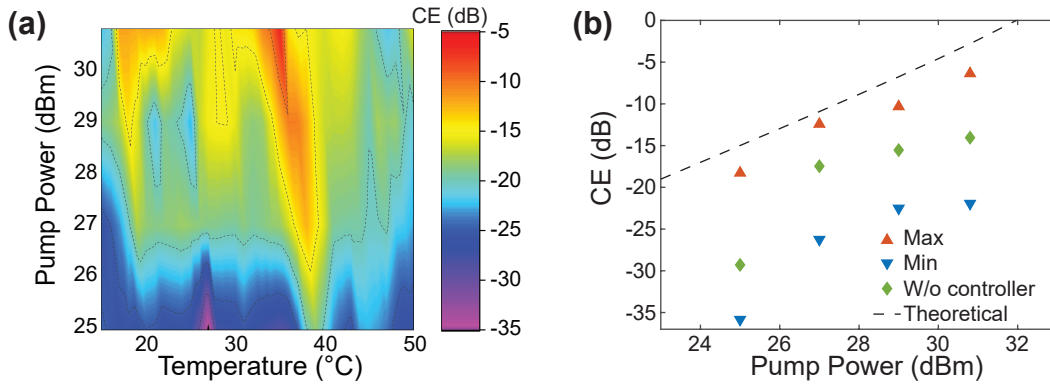
Figure 4.12: (a) Contour graph of experimental CE for various pump power and set temperature of temperature controller in the Si_3N_4 waveguide with the cross-section of 2.2 μm x 0.67 μm and length of 1 m at 1550 nm pump wavelength and 5 nm wavelength detuning (b) The CE values for 25, 27, 29 and 30.8 dBm pump power taken without the temperature controller, and with temperature controller at optimal temperature and least optimal temperature. The dashed line shows the theoretical expectation.

maintaining a fixed 5 nm pump-signal detuning to identify optimal CE conditions. The CE values are derived for coupled pump powers ranging from 25 dBm to 30.8 dBm, considering temperature settings between 15° C and 50° C, with intervals of 1° C. The results of this analysis are depicted in Figure 4.12(a).

The CE fluctuates significantly, exceeding 15 dB variation, with changes in the set temperature, even when the input pump power remains constant. There are distinct optimal temperature settings, in the range of 35° C and 40 ° C, where the highest CE is achieved. It's worth noting that the optimal temperature setting tends to shift to higher values as the pump power decreases. This shift may result from reduced waveguide heating due to lower optical power converted to heat. CEs at optimal temperatures align more closely with the theoretical expectations that CE scales with the square of the pump power.

Figure 4.12(b) shows the CE measured without a temperature controller, the maximum CE obtained at each pump power at the optimal temperatures, and the minimum CE at the least optimal temperatures. The CE retrieved without the temperature controller shows strong variations from the square of the pump power trend. The measured CE values at the optimal temperatures exhibit a better agreement with the theoretical expectation and scaling with the square of the pump power. From the difference between the maximum and minimum temperatures, the temperature can lead to 10-15 dB CE changes as also observed in Figure 4.12(a) . Therefore, heat analysis of the waveguides also plays a strong role.

The optimal temperature setting is one at which interference between different waveguide modes predominantly results in constructive interference at the transitions between the straight and bend segments. This arrangement ensures that most of the light remains within the fundamental mode. Consequently, optical powers are anticipated to exhibit fewer fluctua-
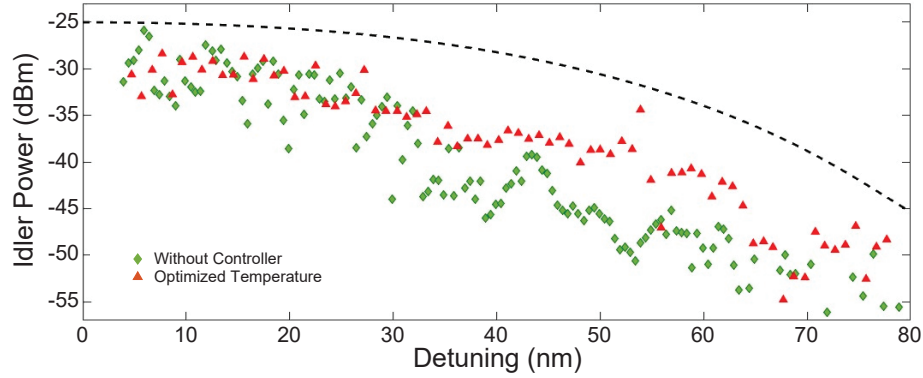
Figure 4.13: The idler power and for an optimized set temperature at every signal wavelength. The dashed line shows the simulated CE for 2.2 μm × 0.67 μm and 1 meter of length

tions with wavelength detuning, provided that FWM is carried out at the optimal temperature for each wavelength detuning.

To verify whether fluctuations with wavelength detuning can indeed be reduced, the idler power is optimized at each wavelength by adjusting the temperature while keeping the input pump and signal powers constant. The results are depicted in Fig. 4.13. It can be observed that optimizing the temperature setting can diminish fluctuations and enhance CE by as much as 10 dB at specific detunings. The experimentally observed trend approaches the theoretical one more closely, although a noticeable discrepancy stemming from the exact waveguide cross-section remains.

4.5   Discussions

Meter-long ultra low-loss buried channel Si_3N_4 waveguides have been the key to unlocking unprecedented CE levels. The dimension tunability feature of the Si_3N_4 waveguides further paves the way for dispersion engineering, and consequently, efficient broadband wavelength conversion. Although various examples of efficient broadband wavelength conversion in such waveguides have been demonstrated in this thesis, several factors have been encountered during the experimental investigation, which limited the enhancement of CE and bandwidth. First, increasing the effective length of the waveguide directly shrinks the bandwidth either with square root or quadratic root of the length depending on the dominance of second-order or fourth-order dispersion, as per theoretical predictions and here experimentally confirmed. Second, the sensitivity of the waveguide's height becomes more pronounced as the length approaches the meter scale, where even a few nm variation in height can significantly narrow the bandwidth. Third, excitation to higher-order modes of the pump can reduce the nonlinear interaction. The existence of the higher-order modes leads to a strong intermodal phase mismatch reducing the effective pump power of the nonlinear process. Moreover, the larger effective areas of the higher-order modes further reduce the CE. Lastly, the excitation of

higher-order modes in the signal and idler leads to mode-mixing during outcoupling from the waveguide, creating fluctuations in pump, signal and idler power, thereby affecting CE.

Tuning the waveguides' temperature is a strategy to reduce power fluctuations when dealing with different optical pump powers. By optimizing the waveguide's temperature based on the specific pump power, it is possible to achieve a significant 10-15 dB enhancement in CE. Diminishing optical fluctuations with wavelength detuning requires meticulous waveguide design engineering. The improvements in design can involve reducing the number of transitions and minimizing the curvature change between the straight and bend segments.

Polarization significantly influences the utilization of Si_3N_4 waveguides in practical applications. Notably, polarization-selective broadband wavelength conversion has been showcased across various wavelength ranges. This includes the L-band and thulium-band, each catering to different polarizations—TM and TE, respectively. Furthermore, polarization-leveraged distant phase-matched wavelength conversion is achieved, opening doors for light generation spanning from the O-band to the mid-infrared spectrum. Nevertheless, some applications call for polarization insensitivity rather than polarization selectivity. In scenarios where the signal's polarization state involves diverse components that cannot always align with a specific wavelength, polarization insensitivity becomes crucial. Achieving this requires symmetry in the principal axes of the waveguide, a condition met by buried channel waveguides.

A square cross-section waveguide can yield a polarization-insensitive nonlinear parameter and bandwidth since it possesses identical mode area and dispersion characteristics for TE and TM polarizations. However, it is important to note that the process remains inherently sensitive to the state of polarization in the pump power, as thoroughly explained in Chapter 2. Depolarized FWM presents a solution to mitigate this sensitivity, albeit at the cost of reduced CE. The upcoming chapter will delve into the theoretical investigation of CE reductions in different depolarization approaches. This theory will be put to the test using chalcogenide glass photonic crystal fibers, known for their relatively less polarization-insensitive nature.

5 Polarization-Insensitive FWM in ChG Fibers

On-chip parametric conversion has a strong potential in various applications. However, the polarization sensitivity is a hurdle in applications where the signal state of polarization (SOP) cannot be adjusted. In this chapter, the concept of depolarization and depolarized FWM theory for polarization-independent FWM will be introduced. In addition, the effect of different depolarization schemes on efficiency will be derived and tested experimentally in meter-long ChG fibers. The ChG fibers are also characterized with polarized FWM at different wavelengths to demonstrate their potential and to compare with the depolarized FWM case.

5.1   Depolarization

Four-wave mixing applications vary significantly with different requirements and figures of merit. Polarization insensitivity of the system to the input polarization of signal is one of the desired features for optical systems exploiting different SOPs. Especially for optical processing where signals could have different SOPs, it is important to have a polarization-independent efficiency and bandwidth in the system to allow for a black box operation and not penalize certain configurations.

The polarization insensitivity comprises the insensitivity of both bandwidth and efficiency. The conversion bandwidth for both principal SOPs depends on the dispersion engineering feature of the platform. The waveguiding structures which are inherently symmetric in the principal polarization axes typically provide similar dispersion characteristics, and hence; a similar conversion is observed [234]. On the other hand, addressing the polarization insensitivity of the waveguide requires intricate solutions due to the inherent susceptibility of the system to the SOPs of the interacting waves as explained in Chapter 2.

One way to address the polarization sensitivity of stimulated degenerate FWM is to split the pump into principal polarization components having orthogonal polarization states counter-propagating through the nonlinear medium. The signal is split into orthogonal SOP components and is injected into the nonlinear platform from the different ends and coupled

together after parametric conversion. However, such a method causes a lower efficiency due to lower pump power and an excess loss due to the requirement of extra optical components [235], [236].

The issue of polarization sensitivity can also be resolved by using a single pump that randomly changes its state of polarization within a specific time frame. This ensures that all polarization-dependent interactions are averaged out. This requirement can be fulfilled by employing a depolarizer. Depolarization plays a crucial role in various domains including fiber-optic communications [237], polarization-dependent gain reduction [238], quantum communications [239], [240], oceanography [241], and navigation [242].

While diverse techniques utilizing electrical modulation of piezoelectric media have demonstrated the effectiveness of polarization scramblers and active depolarizers [243]–[245], passive depolarizers offer a compact and cost-effective solution as they do not require an electric supply. Numerous depolarizer structures have also been demonstrated for free-space operation such as the Cornu depolarizer [246], [247] and wedge-crystal depolarizers [248], [249] or all-fiber design. One of the simple depolarizer schemes that can be implemented via fibers is the Lyot depolarizer employing birefringent fibers with 45 °angle difference exploiting the group-delay time difference of principal modes [250]. However, for narrow linewidth signals, the Lyot depolarizers require kilometers-long fibers limiting the compactness and raising the cost. Such limitations can be overcome by utilizing interferometric depolarization schemes [251], [252]. In interferometric depolarizer structures, the input light is first split into two orthogonal polarizations and then introduced again after decorrelating the polarization components to obtain a depolarized light. One method to obtain a depolarizer is to split the input polarization into two orthogonal polarizations by a polarization beam splitter and with the help of a long polarization-maintaining (PM) fiber, the coherence between two arms is lost. Then, the two polarizations are combined again by another polarization beam splitter [252]. The optical delay to lose the coherence can be obtained by recirculating the light multiple times [253]–[255]. These schemes utilize Mach-Zehnder-based setups to depolarize the light and similar depolarizers have been demonstrated in the last decades [256], [257].

Another method to depolarize the light is to use Michelson-interferometer-based depolarizer schemes. The use of Faraday Rotator Mirrors (FRM) in Michelson-based schemes cancels the birefringence in the arms of the interferometer. Thus, common single-mode fibers (SMF) can be used to induce optical delay instead of PM fibers and directional couplers [258], [259] However, input SOP independent Michelson-based depolarizers reported high injection loss of around 15 dB [258].

Mutugala et al. have made a comparison study between Mach-Zehnder-based depolarizers utilizing long PM fiber and a Michelson-based depolarizer utilizing long SMF fiber. According to their study, the requirement of ultra-long PM fiber makes the Mach-Zehnder-based depolarizers more costly for ultra-narrow bandwidth signals (< 5MHz). However, they are more cost-effective for moderately narrow signals (5-100 MHz) [251]. Therefore, the depolarizer

scheme can be optimized according to the requirements of the applications.

Yang et al. studied FWM with depolarized pump light by Mach-Zehnder-based depolarizer structure and showed that the CE is almost independent of the input SOP of the signal [260]. Various other studies have shown polarization-independent wavelength conversion with scrambled pump SOP [261], [262]. In addition, Salem et al. demonstrated that the scrambled light forming a circle on Poincaré sphere yields a better bit error rate than random scrambling [263].

5.2 Depolarized FWM Theory

In this section, the theory of depolarized FWM depolarization circles is defined on the Poincaré sphere together with possible effects on wavelength CE. The b number, as defined in Chapter 2, will be investigated for different depolarization circles in order to quantify its effect on CE.

5.2.1 Notations and Formalism

The SOP of light can be denoted through two common notations. Jones parameters, as explained in the previous chapters, show the magnitude and relative phase of light polarized in two principal axes and any change in the SOP can be understood through the change in the Jones vector. However, the Jones vector notation is not capable of representing the cases where the light is partially polarized. Stokes parameters, on the other hand, can overcome this limitation. Stokes parameters include 4 parameters, namely S_0, S_1, S_2, and S_3. The S_0 parameter represents the total light intensity of the light which is not information held by Jones vectors. S_1 parameter describes the preponderance of linear horizontal and vertical polarization whereas S_2 parameter describes the preponderance of linear polarization with 45° angle. Lastly, S_3 parameter describes the circularity of the SOP. The Stokes parameters can be described by the following field polarized along principal axes.

$$
\begin{aligned}
S_0 &= \left|\bar{A}_x\right|^2 + \left|\bar{A}_y\right|^2, \quad S_1 = \left|\bar{A}_x\right|^2 - \left|\bar{A}_y\right|^2, \\
S_2 &= 2\operatorname{Re}\left(A_x^* A_y\right), \quad S_3 = 2\operatorname{Im}\left(A_x^* A_y\right)
\end{aligned}
\tag{5.1}
$$

where A_x and A_y are the x and y components of scaled amplitude fields as defined in Equation (2.15), respectively. For a fully polarized light, S parameters also satisfy the condition $S_0^2 = S_1^2 + S_2^2 + S_3^2$. However, this condition is no longer valid for a partially polarized light, i.e. the polarization of light is still biased along a certain SOP but partially randomized. In that case, the ratio of the right-hand side to the left-hand side determines the degree of polarization (DOP), also referred to as ρ, i.e.

$$
\rho = \frac{\sqrt{S_1^2 + S_2^2 + S_3^2}}{S_0^2}
\tag{5.2}
$$
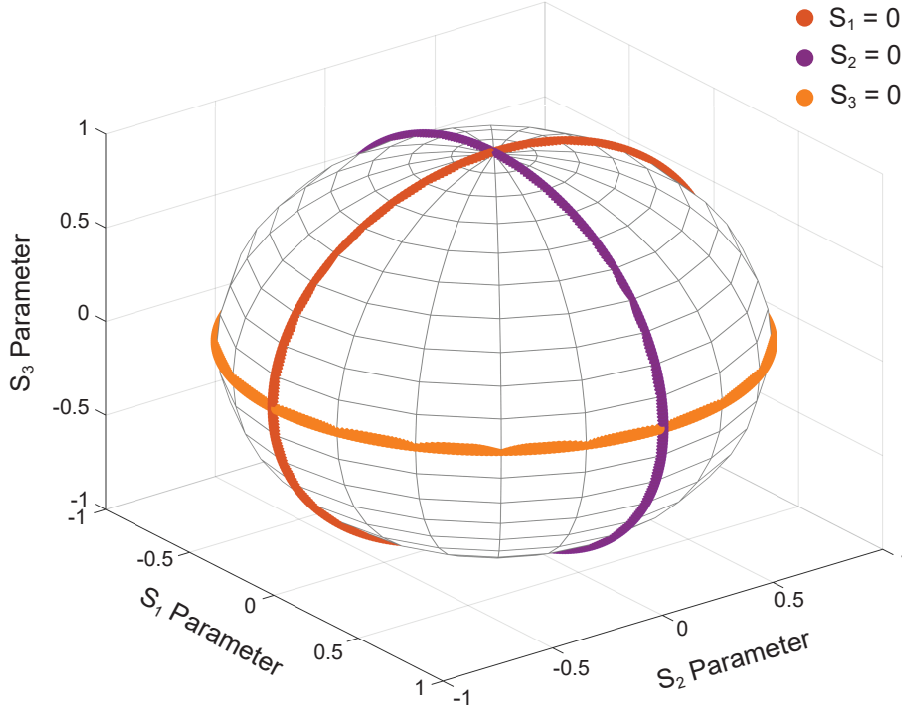
Figure 5.1: The depiction of $S_1 = 0$, $S_2 = 0$ and $S_3 = 0$ circles on the Poincare sphere.

The Stokes parameters can be also shown on the Poincaré sphere whose radius is equal to S_0 parameter and the location on the sphere is determined by the other 3 Stokes parameters. Here, the equator line of the sphere represents the linearly polarized states whereas polar points represent circularly polarized states.

The practical depolarized states average out to a point at the center of the sphere as the DOP approaches 0. However, most practical depolarization schemes consist of incoherently changing orthogonal polarized states. At low integration time, the instantaneous SOP can be resolved into polarized states randomly changing over a circle on Poincaré sphere. Three main circles are depicted in Figure 5.1, namely $S_1 = 0$, $S_2 = 0$ and $S_3 = 0$ circles.

5.2.2 Depolarized FWM efficiency

As explained in Chapter 2, the efficiency of the FWM can change with the pump and signal SOPs. The effect of polarization can be calculated through the b number which can be obtained by Equation (2.46). In this section, the b number for various depolarized pump schemes will be calculated for independently changing signal SOP.

The calculation of b number is relatively intricate for depolarized light. As the depolarized light loses its coherence during depolarization, the CE can be only calculated through averaging in the optical intensity domain. To calculate the average intensity, a uniform probability

for all the SOPs on the depolarization circle is assumed. In other words, the angle on the depolarization circle, θ_{dep}, has an equal probability for all the values between 0 to 2π. To be able to compare the effective nonlinear interactions with the linearly and circularly polarized case, the factor b^2 is defined as

$$b^2 = \frac{\frac{1}{2\pi}\int_0^{2\pi}\left|\chi^{(3)}(\vec{A}.\vec{A})\vec{A}\right|^2 d\theta_{dep}}{\left|3\chi^{(3)}A^3\right|^2} \tag{5.3}$$

where A is the scaled mode field amplitude as defined as (2.15).

The depolarized FWM efficiency can be investigated through 3 main depolarization circles, $S_1 = 0$, $S_2 = 0$ and $S_3 = 0$ circles. The depolarization circles are normally described by Stokes parameters. However, as the FWM efficiency equations are represented in Jones vector formalism, the Stokes vectors will be converted to Jones vectors for the 3 depolarization scheme.

$$J_{p,S_1=0} = \begin{bmatrix} 1/\sqrt{2} \\ e^{j\phi_p}/\sqrt{2} \end{bmatrix} \tag{5.4}$$

$$J_{p,S_2=0} = \begin{bmatrix} \left|\sin\frac{\theta_p}{2}\right| \\ \left|\cos\frac{\theta_p}{2}\right|e^{j\theta_p} \end{bmatrix} \tag{5.5}$$

$$J_{p,S_3=0} = \begin{bmatrix} \sin\frac{\theta_p}{2} \\ \cos\frac{\theta_p}{2} \end{bmatrix} \tag{5.6}$$

where θ_p is the azimuthal angle ϕ_p is the polar angle of the pump on the Poincaré sphere. For the given Jones vectors, if the field is averaged over the equation 2.45 the following b numbers are obtained.

$$b_{S_1=0} = \frac{\sqrt{7}}{3\sqrt{2}} \tag{5.7}$$

$$b_{S_2=0} = \frac{\sqrt{7}}{3\sqrt{2}} \tag{5.8}$$

$$b_{S_3=0} = \frac{\sqrt{5}}{3} \tag{5.9}$$

which are independent of signal polarization angles unlike the cases for linear horizontally or right-hand circularly polarized pump

$$b_{lin} = 3\cos\theta_s + \sin\theta_s \tag{5.10}$$

$$b_{cir} = 2\sin\phi_s \tag{5.11}$$

where θ_s and ϕ_s are azimuthal and polar angle of signal polarization.

The b numbers calculated for different depolarized and polarized pump schemes vs. signal
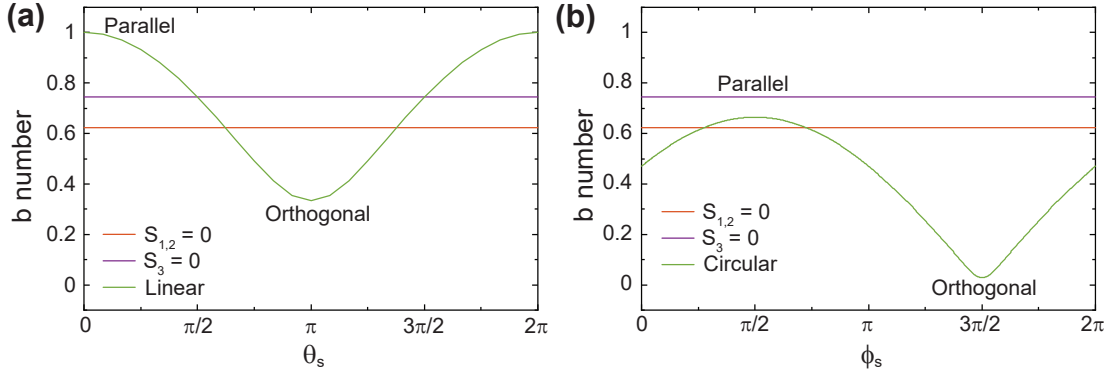
Figure 5.2: The b numbers $S_1 = 0$, $S_2 = 0$ and $S_3 = 0$ circles together with (a) the linearly polarized pump light on the azimuthal angle of the signal SOP (b) the circularly polarized pump light on the polar angle of the signal SOP.

azimuthal angle and polar angle are shown in Figure 5.2 to visualise. As it can be seen from the graph, the b number shows a strong dependence on the signal SOP for polarized pump SOPs as also observed in Equations (5.10) and (5.11). For $S_1 = 0$ and $S_2 = 0$ depolarization circles, the calculated b numbers are identical for all signal SOPs, which can be understood as $S_2 = 0$ circle is made out of the same SOP as $S_1 = 0$ rotated by 45°. However, the $S_3 = 0$ depolarization circle yields higher CE as it consists of only linear SOPs.

Although three main depolarization cases are investigated in the previous parts, the depolarization circle might experience certain transformations for various reasons. First, the coupled power in the nonlinear media can change between two principal polarizations. The optical power imbalance between two orthogonal incoherent lights can cause the light to be biased along a certain axis, resulting in a shrinkage in the radius of the depolarization circles on the Poincaré sphere. To quantify this effect, four cases are investigated where the azimuthal angle is set to 0° ($S_1 = 0$ circle), 30°, 60° and 90° (vertically polarized light) as shown in Figure 5.3(a) inset. The Equation 2.45 is solved numerically for the given four cases. The polarization bias along an axis for the depolarization circle introduces a dependence on the signal polarization. The dependence of the signal polarization is more pronounced as the radius of the depolarization circles on Poincaré sphere shrinks as shown in Figure 5.3(a). Second, the depolarization state can experience polarization rotation due to the birefringence. The rotation of the depolarization circles can cause arbitrary depolarization circles as shown in Figure 5.3(b). For all 4 cases, where the maximum polar angle on Poincaré sphere are 0° ($S_3 = 0$ circle), 30°, 60° and 90° ($S_1 = 0$ circle) polarization-independent CE can be obtained as long as the depolarization circle has the maximum radius on Poincaré sphere. However, the magnitude of the idler field depends on the maximum S_3 parameter as can be seen from Figure 5.3(b). Therefore, the b number for arbitrarily depolarized states lies between $\frac{\sqrt{5}}{3}$ and $\frac{\sqrt{7}}{3\sqrt{2}}$. Notably, the CE scales with the square of the b number as it depends on the optical powers rather than the field amplitudes. Thus, all the depolarization states lead to a CE drop ranging from 2.55 dB to 4.1 dB compared to the observed maximum CE obtained for linear
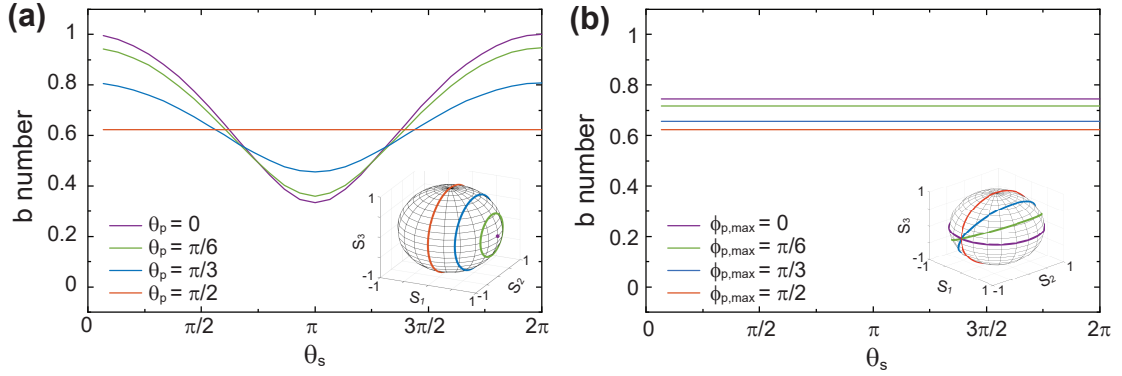
Figure 5.3: The b numbers for (a) various radii of the depolarization circle on the azimuthal angle of the signal SOP (b) various maximum S_3 parameter of the depolarization circle on the polar angle of the signal SOP.

SOPs. As CE for all other depolarization circles lies between this range, $S_1 = 0$ and $S_3 = 0$ cases provide the maximum and the minimum boundaries.

5.2.3 Depolarizer design and results

A Michelson-based all-fiber depolarizer scheme is designed to be later used for depolarized FWM experiments. The depolarizer setup is shown in Figure 5.4. In this scheme, input light is amplified and set to horizontal SOP via polarization beam splitter. Then, an isolator is connected to protect the source from the reflected light. Then, the light is divided into two with the help of a 50-50 coupler. A 5m long silica SMF is used in one of the arms as an optical delay line (ODL), decorrelating the lights from the two arms, followed by a Faraday rotating mirror (FRM) to rotate the polarization. As the polarization is rotated 90 degrees, any birefringence along the way is canceled while propagating backward. In the other arm, a variable optical attenuator is placed to equalise the optical power in the two arms, which is required to neutralize the polarisation bias. An optical reflector (OR) is used at the end to reflect the light without changing the polarization. As the two orthogonal SOPs got introduced together at the output, the resultant polarization state changes randomly along the $S_1 = 0$ circle.

In this design, the isolator, the coupler, and the optical reflector should be polarization-maintaining (PM) to satisfy the orthogonality of the SOP in the two arms. However, as most PM components only maintain the polarization in the principal axes, a polarizer or a polarization beam splitter (PBS) is needed to ensure incident horizontally or vertically polarized light. To overcome the input polarization sensitivity of the depolarizer, a two-stage depolarizer can be employed [251].

The length of the delay line depends on the coherence time of the laser. Depending on the laser spectral linewidth, the phase of the light having different frequency components starts
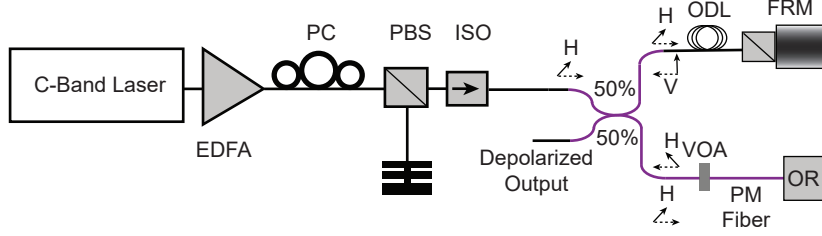
Figure 5.4: The experimental setup of the depolarizer. EDFA: erbium-doped fiber amplifier, PC: polarization controller, ISO: optical isolator, PM: polarization maintaining, PBS: Polarization Beam Splitter, ODL: Optical Delay Line, VOA: variable optical attenuator; FRM: Faraday Rotating Mirror; OR: optical reflector. The dashed arrows depict the propagation direction and the solid arrows depicts the state of polarization: H: horizontal, V: vertical

to lose its temporal coherence as time passes. For a laser with a spectral linewidth $\Delta \nu$, the coherence time, τ_c, is measured as

$$\tau_c = \frac{1}{\Delta \nu} \tag{5.12}$$

The coherence length can be expressed by the length the light travels in a medium in a coherence time. As the light propagates the ODL twice, the length of the ODL should be selected to be higher than the half length of the coherence length, i.e.

$$L_{ODL} \geq \frac{c}{2\Delta \nu n_{\text{eff}}} \tag{5.13}$$

where L_{ODL} is the length of ODL and n_{eff} is the effective refractive index of the medium.

The depolarizer in this work is designed to partially keep the coherence of the two arms so that the polarimeter can resolve the combination of randomly changing polarized light forming the depolarization circle. Such a feature allows us to identify the depolarization circles, which is crucial to distinguish their effect in FWM experiments. The partial coherence has been satisfied by utilizing a 5 m-long optical delay line instead of a much longer delay line (> 100 m) required to completely decorrelate two principal polarizations.

The depolarized light at the output of the depolarizer is inherently set to $S_1 = 0$ circle. However, the depolarization circle on Poincaré sphere can be rotated with a polarization controller. The output of the depolarizer is analyzed with a polarimeter. 10000 measured data points with 1 ms of integration time are taken when the depolarization circle is set to the $S_1 = 0$ circle and the $S_3 = 0$ circle. The obtained Stokes parameters from the polarimeter are shown on the Poincaré sphere in Figure 5.5 (a) and (b), respectively. The histogram of the data points shown in Figure 5.5(c) indicates that there is no significant variance in the angle distribution and uniform random variable assumption is valid. As the integration time increases, the depolarization

(a)

(b)

(c)

(d)
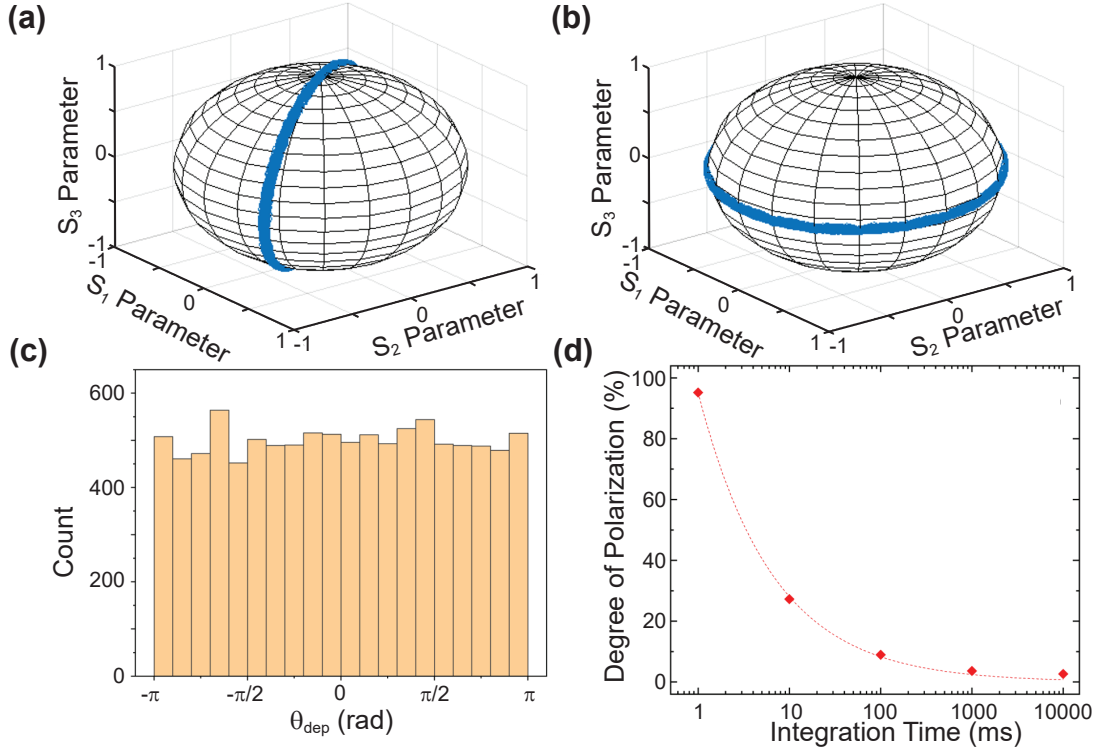
Figure 5.5: The measured Stokes parameters plotted on the Poincaré sphere when the depolarization circle set to (a) $S_1 = 0$ (b) $S_3 = 0$. (c) The measured angle on the depolarization circle plotted as a histogram. (d) The measured degree of polarization (DOP) for various integration times of the polarimeter.

circle approaches a single point close to the center of the sphere which indicates that the depolarizer can be employed in polarization-independent applications for high integration time. The DOP of the depolarizer for various integration time is shown in Figure 5.5(d). The DOP only drops below 10% for an integration time higher than 100 ms. The integration time can be reduced by increasing the length of the optical delay line which might be necessary for high-speed applications. However, the depolarizer is designed as a proof-of-concept in order to examine the depolarized CW FWM where a large integration time is not a liability.

The experimental verification of the theoretical calculations requires a suitable medium. . The waveguides employed in prior chapters exhibit a significant asymmetry in two principal polarization axes. Since the inverse taper couplers are fine-tuned for TE polarization, coupled depolarized light would become partially polarized along a specific axis, thus introducing a polarization sensitivity akin to what is depicted in Figure 5.3(a). The substantial disparities in the effective areas and the marked effective index mismatch between principal polarizations also render the rectangular waveguides impractical for this purpose. Although a short square waveguide employing polarization-insensitive couplers can be used to test the theory, such a waveguide was not at my disposal. Therefore, instead of a waveguide, the theory is examined in a nonlinear fiber platform. ChG fibers provide a great platform to analyze depolarized

FWM as they can provide high CE in short lengths, thanks to their large intrinsic nonlinearity. In the next section, the ChG PCFs will be characterized with the standard polarized FWM experiments to reveal their potential in mid-infrared applications.

5.3   Chalcogenide fibers for nonlinear applications

Chalcogenide fibers have great potential for efficient wavelength conversion, especially in the mid-infrared thanks to their wide transparency and their extremely high nonlinearity. Chalcogenide glasses however exhibit very strong normal dispersion at typical pump wavelegnth, such as in the telecom, which has often been a hurdle in exploiting their potential in these wavelength ranges. In this subchapter, first, the latest studies showing nonlinear interactions in ChG fibers are summarised. Then, two fabricated ChG PCFs theoretically designed for facilitating near-IR operation are characterized at 1.55 μm and 2.0 μwith four-wave-mixing. In addition, the potential of broadband conversion beyond 3.0 μm is investigated in these ChG PCFs in order to achieve a broadband tunable coherent light source that can be used for sensing and spectroscopy applications.

5.3.1   Applications of ChG fibers

A particular feature of nonlinear interactions is that they are not fundamentally bound to any particular spectral band given that a transparent nonlinear medium is available. Such nonlinear interactions, while widely exploited at optical communication wavelengths, are also very well suited for long wavelength operations such as beyond the 2 μm wavelength. Coherent and tunable sources generated in the mid-infrared and far-infrared portion of the spectra can be exploited to sense molecular fingerprints, unlocking various applications[264]–[267].

The traveling wave nonlinear interactions enable obtaining temperature-stable efficient tunable coherent light sources in different wavelength ranges including mid-infrared. Moreover, the generation of nonlinear sources in an all-fiber design offers compactness and robustness [104], [268]. A platform that can provide strong nonlinearity, a wide transparency window and low propagation loss is required for the generation of coherent tunable all-fiber light sources beyond 2 μm wavelength. ChG fibers have indeed tremendous intrinsic nonlinearity [269] (as also explained before in Chapter 2) and a transparency window whose long wavelength cut-off can be tuned from 7 μm to beyond 12 μm depending on the material composition [270]. ChG fibers have been mostly exploited for supercontinuum generation, where the nonlinear propagation of a short pulse results in extreme spectral broadening. Peterson et al. demonstrated a supercontinuum generation extending from 1.5 μm to 13.3 μm covering almost all the molecular fingerprint region [271] with a pump at 4.5 μm and 6.3 μm wavelengths. The following works manage to extend the spectrum of the supercontinuum up to 15 μm [272], [273]. Optical parametric amplification is also simulated in ChG step-index fibers and experimentally shown in liquid-filled ChG PCF [274], [275]. Other works shifting the generated octave-spanning supercontinua to the near-infrared have also been demonstrated [276]. In
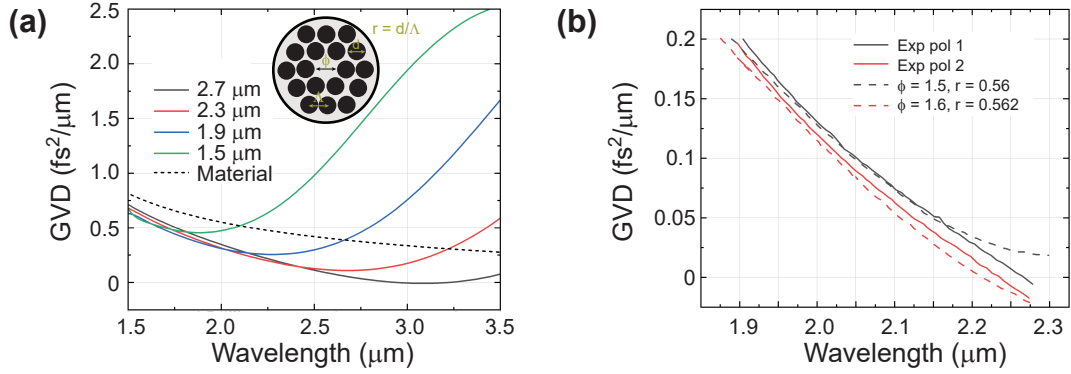
Figure 5.6: (a) The simulated GVD of ChG PCFs for r=0.47 and various core diameters. The dashed line represents the material GVD of GeAsSe glass. The inset depicts the cross-section ChG PCF (b) Measured GVD with interferograms for two different polarizations in the tapered ChG fiber with tapered section core diameter of 1.5 µm and r of 0.56. The dashed lines show the simulated GVDs for the given core diameter and r ratio [280].

addition, an all-normal-dispersion supercontinuum is also demonstrated pumped by more common optical sources at 2 µm wavelength [277].

The ChG materials show very strong group-velocity dispersion for shorter wavelengths than 4 µm hindering the possibility of obtaining efficient phase-matched nonlinear interactions. Although photonic crystal fibers provide some range of tunability by providing strong waveguide dispersion to counteract the material properties, their effect remains limited for relatively large core diameters (>4 µm) such that material dispersion still dominates at short wavelengths. Recently, with advancements in the fiber tapering of ChG PCF, small core PFC could be fabricated with high quality and low loss, not only further enhancing the nonlinearity but also enabling to tune the ZDW closer to 2 µm wavelength [104], significantly reducing the dispersion with a drawback of excess loss. With the advances in the fabrication of tapered ChG PCFs, the excess loss of tapering was able to be mitigated and an output power of 57 mW generated supercontinuum covering from 1 µm to 8 µm has been obtained [278]. Tapering the waveguide also enables the cascaded supercontinuum generation that can be tailored to extend the wavelength span [279].

A hole-to-pitch ratio exceeding 0.65 together with tapering can theoretically shift the ZDW to 1.55 µm for broadband conversion in the telecom band. However, the fabrication of such PCFs poses practical challenges [268].

5.3.2 Characterization of FWM in ChG fibers

Two tapered GeAsSe PCFs were fabricated by SelenOptics to be used in FWM experiments. Fiber 1 is tapered from 11 µm core diameter to 2.7 µm tapered section core. It has a taper length of 1 m with r equals 0.47. Fiber 2 has a tapered section core of 1.5 µm, and an untapered
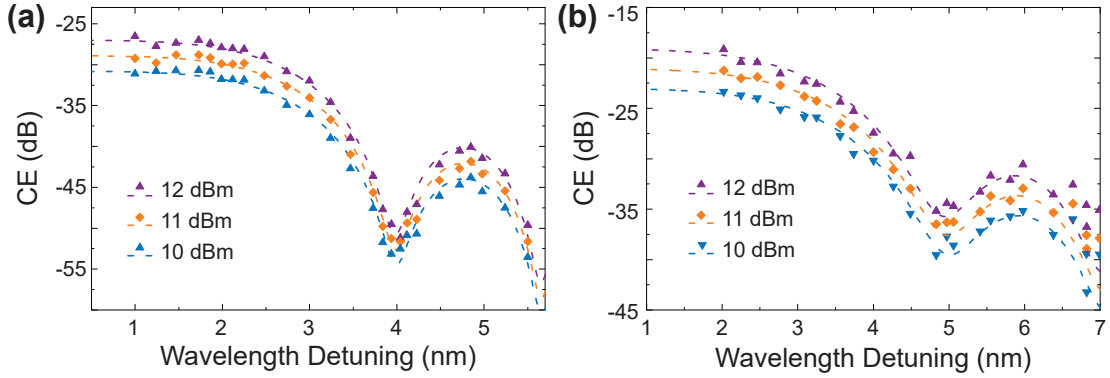
Figure 5.7: The CE vs wavelength detuning PCFs at 10, 11 and 12 dBm pump power (a) in Fiber 1 (b) in Fiber 2. The dashed lines represent the theoretical fits to Equation (2.28)

section core of 4 µm. It has a taper length of 1 m with r equals 0.56 and slightly different GeAsSe content.

In order to investigate the nonlinear potential of the GeAsSe PCF, the structures are simulated with COMSOL for various parameters such as the core diameters (ϕ) and the air holes' diameter-to-pitch ratios r = d/Λ (Figure 5.6(a)). The simulated GVD for various core diameters is shown in Figure 1(a) together with material GVD. The minima of the GVD shifts toward shorter wavelengths as the core diameter shrinks. However, such reduction also causes the fiber to have all-normal dispersion without a ZDW in the interested wavelength range. Such behavior of GVD can be altered by changing the r ratio or Ge content in GeAsSe.

Fiber 1 is expected to have dispersion characteristics shown in Figure 5.6(a). Fiber 2 is also simulated according to Sellmeier's Equation provided by the manufacturer and characterized by low-coherence interferometry with an all-fiber Mach Zehnder interferometer by Dr. Svyatoslav Kharitonov [280], shown in Figure 5.6(b). The measurements showed that the fiber exhibits a birefringence which can be attributed to the slight ellipticity of the core and mismatch in the air holes diameter-to-pitch ratio. Fiber 2 is measured to have a ZDW at 2.23 and at 2.265 µm for different polarization states together with another expected ZDW around 2.5 µm according to the simulations. Similarly, Fiber 1 is expected to show 2 ZDWs at 2.95 µm and 3.2 µm. It should be noted that the ZDWs are very sensitive to the core diameter and that the fibers could have all-normal dispersion characteristics with only a slight change in structure dimensions even though the absolute GVD is still expected to remain low, allowing broadband wavelength conversion.

The ChG PCFs are characterized by four-wave-mixing (FWM) with a setup including pump-probe architecture utilizing sources in the C-band and at around 2 µm wavelength at the coupled pump powers of 10, 11, and 12 dBm and -10 dBm signal power. Before testing the depolarization scheme, the sources serving as pump and signal are set to linear polarization and coupled into the fiber with a lensed fiber. The output light is collected with a lens and collimated to the optical spectrum analyzer (OSA) Yokogawa AQ6375B. For close enough waves
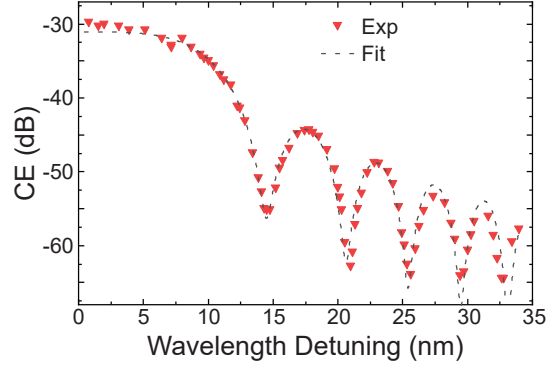
Figure 5.8: The CE vs wavelength detuning for co-polarized signal and idler at 2002 nm wavelength in Fiber 2 at 10 dBm coupled power. The dashed line represents the theoretical fit.

in wavelength, the CE can be directly extracted from the OSA traces by taking the measured output idler power divided by the measured output signal power. The results of the FWM study in Fiber 1 and 2 for a the pump wavelength set to 1550 nm are shown in Figure 5.7(a) and (b). The measured CE fitted with Equation (2.28) with nonlinear parameter, $\gamma = 4.5 \mathrm{W}^{-1}\mathrm{m}^{-1}$, GVD of 625 ps^2/km, and absorption coefficient, α, of 1.8 dB/m for Fiber 1 and $\gamma = 9.0 \mathrm{W}^{-1}\mathrm{m}^{-1}$, GVD of 400 ps^2/km and α of 4.0 dB/m for Fiber 2. A smaller core diameter, as for Fiber 2, provides stronger confinement in the core, resulting in higher nonlinear parameters and CE. The coupling loss is measured to be 4 dB which might be due to the excess loss at the transition between untapered and tapered sections. Such optical loss at the transitions causes an error in the coupled input power, and as a result, in γ. Nevertheless, the nonlinear parameter is in agreement with the simulations. The fitted GVD of 625 ps^2/km is also in good agreement with the simulation results. Evidently, despite the tapering, the GVD is still very strong at telecom wavelength, resulting in a narrow bandwidth. The fit implicates higher propagation loss in Fiber 2 which may be caused by more scattering loss due to smaller core or higher attenuation of the material. Two-photon absorption is not observed at these power levels.

The experiment is repeated with sources at 2000 nm wavelength (as explained in Chapter 3) in Fiber 2, which is expected to have a lower GVD near this wavelength and should therefore exhibit a broadening in the bandwidth. The estimated coupled pump power is approximately 9.5 dBm. The experimentally measured CEs with wavelength detuning together theoretical fits are presented in Figure 5.8. A very good fit of CEs is observed with parameters $\gamma = 4.0 \mathrm{W}^{-1}\mathrm{m}^{-1}$, $\beta_2 = 135 \mathrm{ps}^2$/km, and $\alpha = 1.5$dB/m. The measured GVD in FWM process also confirms the GVD values obtained in simulations and in interferometric measurements shown in Figure 5.6. Compared to the experiment at telecom wavelength, a lower propagation loss is expected at the longer wavelengths as photon energy gets further from the band tail. The decrease in the nonlinear parameter is also expected as it drops not only with the increasing wavelength but also with the increasing effective area. The conversion bandwidth is increased from 6 nm to 24, the GVD is still relatively high and longer pump wavelength would be required to get closer to the ZDWs expected to be at 2.27 μm.
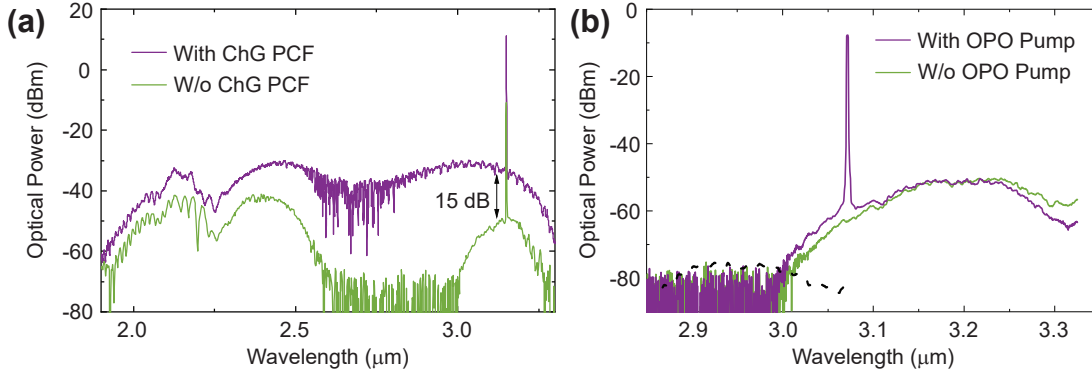
Figure 5.9: (a) The optical spectra obtained in the OSA with and without the ChG fiber, demonstrating the optical loss of the waveguide. (b) The dispersive wave spectra filtered below 3000 nm wavelength with and without OPO idler serving as pump- The expected idler formation at a constant -25 dB CE is shown by the dashed line, serving as a guide to eye.

Another experiment is designed to exploit the expected ZDWs of Fiber 1 at around 3 μm in pursuit of broadband wavelength conversion. An FWM experiment with a free-space setup is built where the idler of the optical parametric oscillator (OPO) serves as the pump, which is tunable between 2.7 μm to 3.2 μm. The signal was generated by Dr. Eirini Tagkoudi from a silicon nitride chip pumped with a fs source at 1550 nm wavelength at 90 fs pulse duration and 1 nJ pulse energy. The pulsed source generated a dispersive wave (DW) during a soliton driven supercontinuum generation [281], [282] . The DW generated between 2.8 μm and 3.4 μm is filtered with a long-pass filter at 3 μm and coupled with the pump in and out of the fiber with the help of chalcogenide lenses and collimated into the OSA. The obtained spectra with and without ChG fiber are shown in Figure 5.8(a). An extensive increase in the propagation loss beyond 2.5 μm up until 3.1 μm is observed. The origin of such an extensive loss is quite intricate and unexpected in ChG fibers. One of the factors of the loss in that part of the spectra can be the water absorption, which is dominantly effective between 2.7 μm to 3.1 μm, and which is already visible in the spectra without the ChG fiber. Water in the fiber might be due to exposure to humidity during storage which could lead to extremely strong absorption upon propagation. The DW is filtered with a long-pass filter in order to observe idler generation in the shorter wavelengths of the OPO light via FWM. However, the generated idler remained lower than the noise level the OSA (Figure 5.8(b)) which might be due to lower nonlinear interaction or excess loss in the wavelength span of the idler. Due to the limited availability of sources, the exploitation of the mid-infrared ZDW of the ChG fiber could not be further investigated.

5.4   Depolarized FWM in ChG fibers

Testing of the depolarized FWM theory is challenging as most platforms cause a strong rotation of the depolarization circle due to birefringence. The birefringence problem is even more
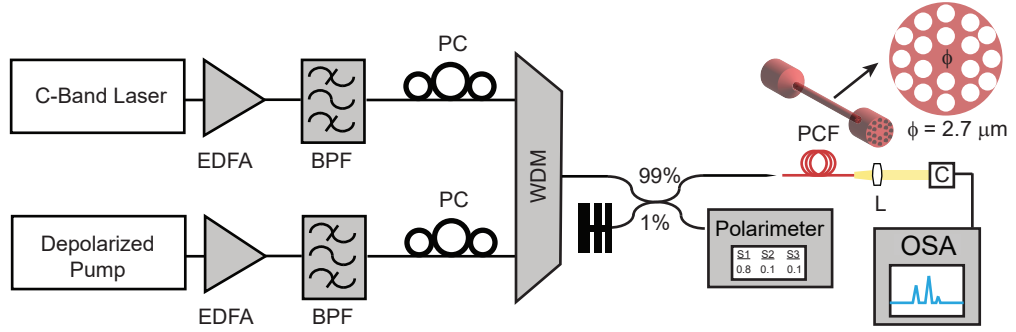
Figure 5.10: The experimental setup of the depolarized FWM. EDFA: Erbium-Doped Fiber Amplifier, BPF: Band-Pass Filter, WDM: Wavelength-Division Multiplexer, OSA: Optical Spectrum Analyzer.

pronounced in PM fibers as the depolarized light cannot be set to principal axes. Such rotation prevents us from observing the difference between CEs of different depolarization circles which would be expected from the theory. A medium demonstrating low loss, low birefringence, and high nonlinearity is required in order to differentiate the effect of the depolarization circle on the CE. The ChG PCFs tested in the previous sections are good candidates for satisfying these conditions. The strong nonlinearity of the ChG PCFs provides the possibility of wavelength conversion in short lengths providing a possibility of maintaining the depolarization circles before getting totally randomized as a result of birefringence.

Fiber 1 has been tested by a traveling-wave pump-probe architecture where the CW depolarized light serves as the pump. The obtained depolarized light is set at 1547.5 nm wavelength, which is then amplified with an erbium-doped fiber amplifier (EDFA) serving as the pump for the FWM process. The amplified light is then filtered out with a band-pass filter to eliminate the amplified spontaneous emission. A polarization controller is placed to adjust the depolarization circle. Similarly, the signal is also amplified and filtered to be able to measure the lower conversion efficiencies. The pump and signal, about 1 nm apart, are combined with a wavelength division multiplexer to reduce losses. A 99/1 coupler is utilized to measure SOP with the polarimeter through the 1% port. while 99% of the light is coupled to the tapered ChG PCF with a lensed fiber. The coupled pump power is estimated to be 12 dBm and the coupled signal power is estimated to be -10 dBm. The light is coupled out with an objective and a collimator at the output and analyzed with an optical spectrum analyzer (Figure 5.10).

The CEs are measured repeatedly after changing the signal azimuthal and polar angle of SOP. The CEs with the $S_1 = 0$ and $S_3 = 0$ depolarized pumps for the various signal SOPs are shown in Figure 5.11. Similar to the polarization-independent CE expected from the calculations, limited differences between the maximum and the minimum CEs are obtained, which are approximately 0.75 dB and 1.2 dB for $S_1 = 0$ and $S_3 = 0$, respectively. The difference is rather small in comparison to the 9.5 dB difference between the maximum and the minimum CEs for
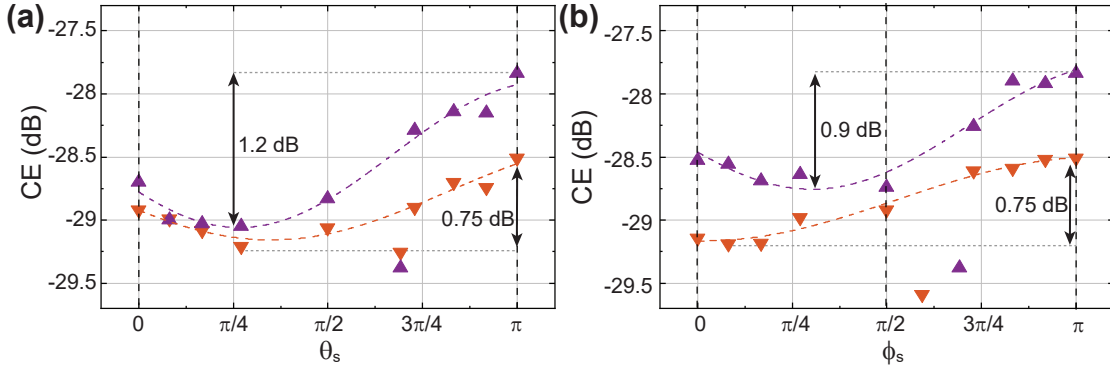
Figure 5.11: The conversion efficiencies for $S_1 = 0$ and $S_3 = 0$ depolarized pump (a) for various azimuthal angles of the signal SOP (b) for various polar angles of the signal SOP.
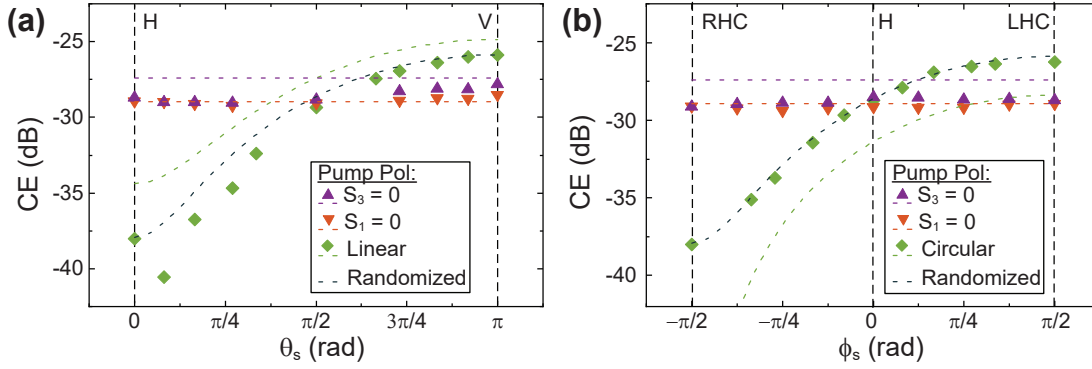
Figure 5.12: The CE for (a) vertically polarized light together with $S_1 = 0$ and $S_3 = 0$ depolarized light for various azimuthal angles of the signal SOP. LHC-Pol refers to left-hand circularly polarized light. H refers to horizontally polarized light, V refers to vertically polarized light, and RHC refers to right-hand circularly polarized light. The legend denotes the pump SOPs.

linearly polarized pump light. The discrepancy might be due to the slightly different nonlinear parameters for different SOPs of the ChG fiber as well as the discrepancy in the coupled pump power for different SOPs.

The calculated b numbers from the Equations 5.7,5.8,5.9 envision a 1.55 dB CE difference between $S_3 = 0$ and $S_1 = 0$. The average CE for $S_3 = 0$ depolarization is higher than for $S_1 = 0$ showing a significant dependence on the depolarization circle as estimated from the theory. However, the measured average difference in CEs is smaller than 1.55 dB, which is approximately 0.3 - 0.5 dB on average. The birefringence of the ChG fiber might be the cause of lower CE differences between the $S_3 = 0$ and $S_1 = 0$. The change of CE remained around 0.5 dB.

To further investigate the polarization effect in ChG PCF, the same experiment is repeated for a vertically polarized and right-hand circularly polarized light. The CEs for various azimuthal angle and polar angle of signal SOPs together with the corresponding CEs of depolarized pump SOPs are presented in Figure 5.12(a) and (b), respectively. The black dotted line shows
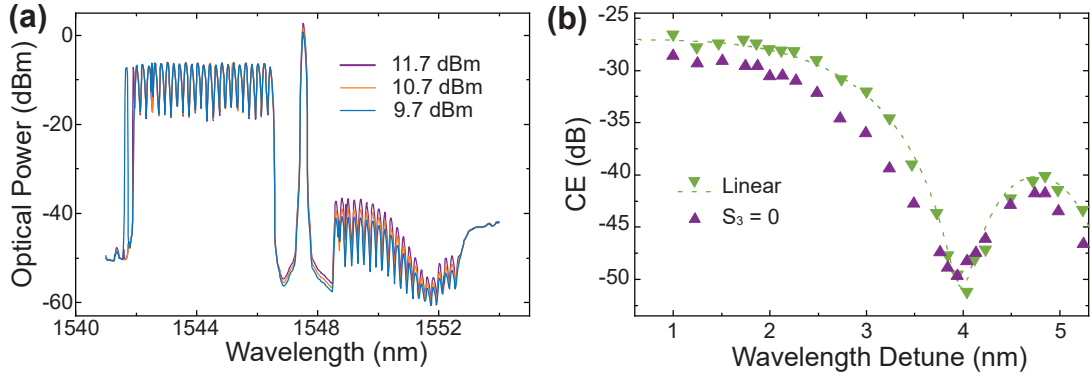
Figure 5.13: (a) The superimposed spectra with the swept signal wavelength for the $S_3 = 0$ depolarized pump. (b) The CE for $S_3 = 0$ depolarized and horizontally polarized light vs. wavelength detuning for 11.65 dB pump power.

the expected trend for the linearly polarized light, whereas the green dashed line shows the trend for the randomized polarization with birefringence in Figure 5.12(a). How the b number changes for the birefringent platform randomizing the SOP is calculated in Equations (2.49) and (2.50). The change in CEs with the azimuthal angle of the signal SOP agrees better with the randomized polarization compared to the expected trend for the linearly polarized light. Similarly, for a right-hand circularly polarized pump light, the polar angle is changed this time and CEs are presented in Figure 5.12(b). Compared to the dotted line showing the expected change for the circular polarization, the change of CEs with the polar angle agrees better with the randomized polarization with the birefringence. In addition, obtaining a similar trend for both linear and circular pump SOP favors the existence of birefringence. The CEs obtained via depolarized FWM are also shown to demonstrate polarization insensitivity and the maximum efficiency drop of depolarized FWM compared to polarized and strongly birefringent FWM.

The effect of depolarized FWM on wavelength detuning trend is also investigated by detuning the signal wavelength from 1542 nm to 1546 nm. The spectra are superimposed by holding the maxima of the spectra for three pump power values (Figure 5.13(a)). The formed idler power scales with the square of the pump power as expected with no significant change in the dispersion with the pump power. The CEs for the 11.65 dB pump power are compared with the linearly polarized pump power and presented in Figure 5.13(b). The generated idler remains coherent as it follows the sinc trend with the wavelength detuning. Moreover, the difference in the CEs for linearly polarized light and $S_3 = 0$ depolarized pump light is in agreement with the expected 2.5 dB difference for the small wavelength detunings. The wavelength detuning at which the first minima occurs shifts slightly with the depolarized pump. The change in the dispersion with the polarization might cause such a shift in the wavelength detuning at which the CE minima occur.

The experimental study in this subchapter confirms the three theoretical expectations. First, the CE scarcely changes with the changing signal SOP, in agreement with the previous claims

[260] and the analysis made in this work. Second, around 2.5 dB CE difference has been observed between the linearly polarized pump and $S_3 = 0$ depolarized pump, confirming the drop in efficiency estimated from the derivation. Last, different depolarization schemes can yield different efficiencies, with the observed CE change of around 0.5 dB. However, the 1.5 dB CE difference is not observed in the ChG PCF between the $S_3 = 0$ depolarized and the $S_1 = 0$ depolarized pump, possibly due to the birefringence. Although the ChG PCF was chosen to satisfy the high CE in a reduced lengths the possible mismatch in the hole diameters might lead to a strong refractive index mismatch between different polarization components [280]. Therefore, a platform that provides even lower refractive index mismatch for the principal polarizations, as well as strong nonlinear interactions in short distances, is required. High mode-confinement and polarization-independent effective index of the on-chip square waveguides might overcome this limitation to prove the theory. A short version of this chapter can be found in [283].

6 Conclusions and Outlook

The Si_3N_4 waveguides have strong potential for CMOS-fabrication compatible monolithic integration of nonlinear processing units. Continuous-wave (CW) parametric wavelength CE of the waveguides can be boosted up to unprecedented levels thanks to the ultra-low propagation loss, high-quality stress-free fabrication, capability of operating at watt-level pump powers and relatively higher nonlinearity compared to other CMOS-compatible insulators. The advancements in fabrication techniques overcome the limitations due to excess stress in thick waveguides which also enables a strong tunability for the dispersion engineering.

6.1 Efficient broadband on-chip wavelength conversion in the telecom band

Various CW parametric wavelength converters have been demonstrated in this thesis operating in the C-band for efficient broadband conversion in Si_3N_4 buried channel waveguides. The highest CE of 2.9 dB is demonstrated in the thesis with narrow bandwidths and bandwidths that can extend up to 160 nm in the L-band at a lower CE. The wavelength conversion schemes shown in this thesis are compared with the state-of-the-art CW wavelength converters in various platforms, as shown in Figure 6.1. The Si_3N_4 waveguides clearly emerged in recent years as a competitive alternative to the Si-based and AlGaAs-based platforms. This thesis serves as a significant framework for bandwidth broadening and possible drawbacks of the process.

The theoretical calculations show that the ideal cross-section of 2.2 µm × 0.67 µm and 1 m length can yield 350 nm 3-dB bandwidth in addition to the 11 dB phase-matched CE at 6 W of coupled pump power, as coupled before [190], and -1 dB CE at 1.7 W. Although the challenges presented hindered reaching such an efficient broadband performance, it also shows the room to improve the performance of the waveguides.
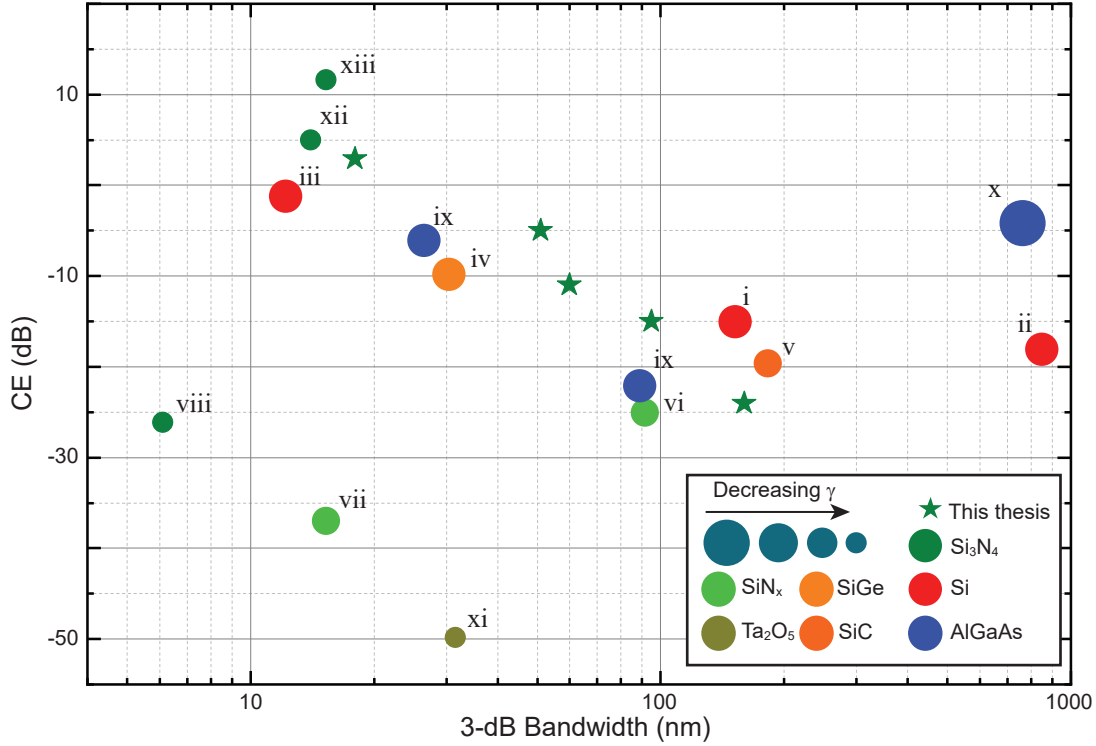
Figure 6.1: The selected state-of-the-art CE and 3-dB bandwidth performance of wavelength conversion schemes in comparison with the results presented in this thesis. i [284], ii [126], iii [128], iv [130], v [285], vi [173], vii [168], viii [163], ix [149], x [155], xi [286], xii [189], xiii [190], the works presented in this thesis [287]–[289]. SiN_x represents the silicon-rich silicon nitride.

6.1.1 Challenges toward efficient broadband parametric conversion

To begin with, equipping on-chip structures with high-power pump sources that can deliver watt-level optical power poses a significant challenge. While recent demonstrations with on-chip erbium-doped waveguide amplifiers have achieved output powers around 150 mW [290], reaching the watt-level powers remains elusive. Moreover, the optical losses at such high optical powers can introduce heating and create temperature gradients, potentially affecting other interferometric or microresonator components. Finally, attempting to increase optical powers beyond a certain threshold can lead to device failures, as exemplified in the case of a ridge Si_3N_4 waveguide, which was observed to experience a waveguide fuse at a pump power of 38 dBm (approximately 6.3 W) [291].

Second, the hypersensitivity of the dispersion characteristics to the waveguide dimensions forms an impediment. Theoretical calculations estimate a decrease in the bandwidth with the quadratic root of the length around ZDW, which indicates that a high CE enhancement can be achieved at the expense of a relatively lower reduction in the bandwidth. However, a few nm changes in the height of the waveguide increase the GVD. Consequently, a significantly smaller bandwidth is obtained than the desired one. Moreover, the bandwidth narrows with

the square root of the effective length, causing a steeper change. Another factor arises when the broadband conversion is satisfied with the merger of the main phase-matched conversion band with the higher-order phase-matching band. As the effective length increases, these bands segregate and cause a rapid drop in the bandwidth. Minute variations in the waveguide height can also hinder the merge of the main phase-matching band with the higher-order phase-matching band.

The excitation of the higher-order modes is also a major concern for efficient broadband wavelength conversion. The meter-long integrated waveguides are folded into spirals utilizing circular (bend) segments with different curvatures. The curvature changes through the waveguides give rise to the excitation of the higher-order mode with slight optical power yet they build up as a consequence of hundreds of transitions. Dissociating optical power from the fundamental mode to multiple modes causes a severe reduction in the CE due to high intermodal phase mismatch and lower nonlinearity of the higher-order modes. Additionally, as the dispersion characteristics of the higher-order modes are not engineered to have low dispersion, the wavelength conversion at the higher-order modes yields a narrow bandwidth.

Another major concern in the operation is mode-mixing leading to fluctuations higher than the CE drop at the 3 dB bandwidth. Idler power oscillations are not only active in the bend segment transitions but also at the outcoupling stage. Additionally, mode-mixing is sensitive to temperature, wavelength and optical power at high powers and insensitivity of these factors is the main advantage of traveling-wave nonlinear interactions compared to resonator-based schemes.

For spirals having straight and bend segments, the number and curvature of transitions depend on the length of the waveguide and the footprint of the waveguide on the chip. The footprint also constitutes a crucial optimization parameter for fully integrated applications. Engineering the waveguide design can ameliorate the number and curvature of the bends to limit the high-order mode excitation [292]. However, further improvements might come with the sacrifice of compact integration to small footprints.

A more smooth change in the curvature can also yield a lower excitation to the higher-order modes. The employment of Euler bends [293] or changing the spiral structure to a uniform change in the curvature as in the case of Archimedean spirals [294] can serve as a potential improvement in such structures. However, as CE fluctuations are also observed in parametric amplification experiments in Archimedean spirals [189], such optimization necessitates careful optimization and further experimental verification.

6.1.2   Enhancing nonlinear parameter

The moderate nonlinearity of Si_3N_4 waveguides necessitates high pump powers and effective length to compete with other semiconducting platforms. The power and length requirements of the waveguides can be alleviated with an increased nonlinear parameter. Introducing a
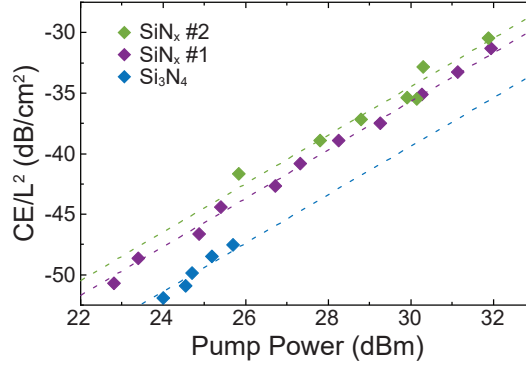
Figure 6.2: CE per length square for various pump powers for the characterization of the nonlinear parameter. Dashed lines are linear fit used to measure the nonlinear parameter.

slightly higher proportion of silicon into the Si_3N_4 compound can provide such improvement.

To estimate the potential of such waveguides, two LPCVD-grown Si-rich SiN_x buried channel waveguides fabricated by Univ. Grenoble Alpes, CEA, LETI [295] with sub-micron dimensions ($0.9\,\mu m \times 0.8\,\mu m$) are tested. The lengths of the waveguides are 1.1 and 0.8 cm. In addition, another stochiometric Si_3N_4 waveguide with the cross-section is fabricated by A. Stroganov from LIGENTEC at 3 cm length to serve as a control group.

Loss measurements conducted by O. Yakar revealed that the propagation loss of Si-rich SiNx waveguides reached approximately 6 dB/m in the microresonators on the same chip. In the transmission experiments, a 2 dB coupling loss was observed. Subsequently, the traveling CW wavelength conversion performance of the waveguides at 1550 nm was tested at 5 nm wavelength detuning. The measured CE per the length square for various pump powers in the waveguides are shown in Figure 6.2. The nonlinear parameter was calculated based on the linear fits indicated by the dashed lines. For the stoichiometric Si_3N_4 waveguide, the nonlinear parameter is measured to be $1.05\ \mathrm{W}^{-1}\mathrm{m}^{-1}$. For SiN_x #2, the waveguide with the highest Si ratio, the nonlinear parameter is found to be $1.64\ \mathrm{W}^{-1}\mathrm{m}^{-1}$ and for SiN_x #1, which contains less Si percentage, it is found to be $1.51\ \mathrm{W}^{-1}\mathrm{m}^{-1}$.

The low loss of these waveguides together with enhanced nonlinearity holds great promise for on-chip wavelength converters. With the advancements in the fabrication of these waveguides, the pump power and effective length requirements can be alleviated. Still, a study of nonlinearity-loss trade-off with incorporated Si is required to further estimate the potential as well as an exploration for two-photon absorption limits. Other platforms offering strong nonlinearity can be an alternative solution as well with the advancements in the fabrication reducing the optical loss.

6.2 Potential in nonlinear applications

Spiral meter-long Si_3N_4 waveguides display substantial promise in many nonlinear applications despite the encountered challenges. The dispersion engineering in the waveguides still unlocks various possibilities and potential applications. The generation of coherent light in the various wavelength spans enables IR-light detection, chemical or bio-sensing and spectroscopy, to name a few. Si_3N_4 waveguides are still a strong candidate for various system-on-a-chip applications not only for their nonlinear performance but also for material stability, CMOS compatibility for monolithic integration and induced $\chi^{(2)}$ nonlinearities [196], [197].

Two-sided 20-dB bandwidths of over 400 nm at 2 µm wavelength and over 200 nm at 1.55 µm have been demonstrated in this thesis in addition to 160 nm 3-dB bandwidth. Such functionality enables the generation of sources from 1450 nm to 1690 nm and 1820 to 2200 nm utilizing erbium and thulium band sources. Distant phase-matched conversion also extends the wavelength span to 2.6 µm in the longer wavelengths allowing near-infrared spectroscopy that can sense various molecules such as vitamins, nucleobases, alcohol, and caffeine [296]–[299]. Moreover, the distant conversion to the O-band enables biosensing and bioimaging applications [300], [301].

Utilizing nonlinear applications for optical communication based applications requires a narrow-band pump linewidth to avoid interchannel crosstalk in the converted wavelengths.CW sources not only provide the required narrow linewidth but also the ability to conduct optical processing without walk-off with the input data. Therefore, this thesis focuses on CW wavelength conversion that can address such requirements. However, other applications can have more tolerance for a broader linewidth or do not constitute the walk-off risk so that a modulated or pulsed pump light can be employed. The pulsed pump light results in an enhancement in CE proportional to the duty cycle at the same average power. The pulsed operation further allows supercontinuum generation together with distant FWM as it has been demonstrated by Kowligy et al. [71]. They showed that efficient conversion up to 3.6 µm wavelength can be obtained in the ridge Si_3N_4 waveguides.

6.2.1 Cascaded four-wave-mixing process

The FWM process is not limited to generating one idler but can generate many idlers provided that the signal has sufficient optical power to serve as a pump. This process is called cascaded four-wave-mixing as many degenerate and non-degenerate four-wave-mixing occur simultaneously stimulated by the cascaded generated idlers. The efficient conversion in Si_3N_4 waveguides shows great potential to host cascaded four-wave mixing.

To explore this potential, the 2 m long waveguide, which exhibited the highest CE performance, is chosen to host cascaded FWM. In this setup, 1537 and 1541 nm CW light was introduced into the waveguide with an estimated coupled power of 31 and 29 dBm, respectively. This con-

(a)

(b)
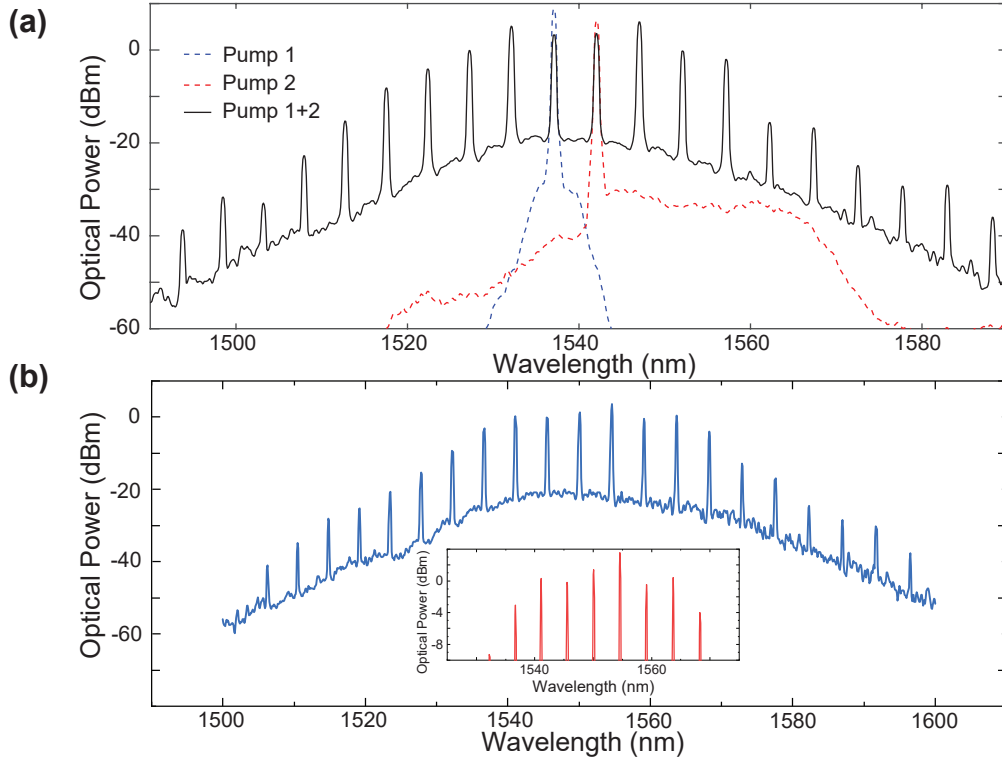
Figure 6.3: Optical spectra of cascaded FWM as a result of (a) 31 dBm and 29 dBm coupled pump power at 1537 and 1541 nm (b) 32 dBm and 31 dBm at 1550 and 1554.7 nm. The inset shows the zoomed spectra for the lines having the highest optical power.

figuration acted as a two-pump parametric amplifier, resulting in the generation of both first and higher-order idlers. These idlers were produced through efficient FWM with a consistent separation of 4 nm, as illustrated in Figure 6.3(a). Notably, the first-order idlers experienced parametric gain, and the generated idlers spanned more than 100 nm in wavelength.

Wavelengths were adjusted to 1550 and 1554.7 nm using optical powers of 32 dBm and 31 dBm. Through precise temperature and wavelength tuning, these waveguides achieved more efficient conversion by reducing the impact of mode-mixing. Figure 6.3(b) illustrates the resulting spectra from cascaded four-wave-mixing, where the generated idlers cover a range of over 100 nm in wavelength. The enhancement in CE resulted in eight distinct lines within an 8 dB range.

Cascaded FWM processes have been previously showcased for generating laser sidebands, pulse compression, and generating multicolor pulses [302]–[304]. The Si_3N_4 waveguides present promising opportunities for utilizing pulsed light. Enhancing the efficient continuous-wave (CW) idler generation is possible with pulsed sources. Furthermore, this process of cascaded idler formation using coherent sources holds significant potential for creating tunable optical frequency combs in Si_3N_4 waveguides.

6.2.2 Polarization-insensitive waveguide conversion

The waveguides' polarization-selective characteristics enable a range of on-chip applications. However, this polarization sensitivity can pose challenges when controlling the signal polarization is not feasible. For such an FWM process, the polarization-insensitive parameters of the waveguide are necessary but not sufficient. While square waveguide fabrication may meet these criteria, confirming the low-loss fabrication of extended square waveguides through experimentation is essential.

The FWM process has inherent pump polarization sensitivity even when the medium is completely symmetric. Depolarization is a way of overcoming the pump polarization sensitivity with passive components. Depolarized FWM comes with a sacrifice of CE. Three depolarization circles are investigated theoretically in this thesis, namely $S_1 = 0$, $S_2 = 0$ and $S_3 = 0$. The theoretical calculations anticipate a minimum amount of 2.55 dB drop in CE, which occurs for $S_3 = 0$, and a maximum amount of 4.1 dB drop in CE, which occurs for $S_1 = 0$ and $S_2 = 0$.

The decrease in the CE is experimentally investigated in chalcogenide glass (ChG) photonic-crystal fibers (PCF). The experimental characterization observed a minimum amount of 2.5 dB and drop in CE and a maximum amount of 3.0 dB which might be explained by changing the birefringence axes of the fiber randomizing the polarization state. The fabrication errors in the PCF structure can lead to such a change as well as a twist along the propagation axis.

The theoretical calculations can be tested in square waveguides provided that the fabrication error can be mitigated below a certain level so that the polarization change due to birefringence is relatively negligible. The waveguide can be selected as relatively short to further reduce the birefringence effect.

In conclusion, the extensive exploration of nonlinear silicon nitride waveguides within the scope of this thesis underscores their immense potential for on-chip optical processing and integrated photonics. While addressing the challenges highlighted herein is vital, there is still ample room for enhancing CE and bandwidth. The intriguing polarization-selective properties of these waveguides can cater to specific applications and depolarized FWM offers a pathway to achieving on-chip polarization-insensitive parametric conversion. With the characteristics explored in this work, silicon nitride waveguides are poised to play a pivotal role in the future of nonlinear integrated photonics.

Bibliography

[1]   G. E. Moore, "Cramming more components onto integrated circuits", *Electronics*, vol. 38, no. 8, pp. 114–117, Apr. 1965.

[2]   G. E. Moore *et al.*, "Progress in digital integrated electronics", in *Electron devices meeting*, Washington, DC, vol. 21, 1975, pp. 11–13.

[3]   G. Bae, D.-I. Bae, M. Kang, *et al.*, "3nm gaa technology featuring multi-bridge-channel fet for low power and high performance applications", in *2018 IEEE International Electron Devices Meeting (IEDM)*, IEEE, 2018, pp. 28–7.

[4]   N. Loubet, T. Hook, P. Montanini, *et al.*, "Stacked nanosheet gate-all-around transistor to enable scaling beyond finfet", in *2017 Symposium on VLSI Technology*, IEEE, 2017, T230–T231.

[5]   T. N. Theis and H.-S. P. Wong, "The end of moore's law: A new beginning for information technology", *Computing in science & engineering*, vol. 19, no. 2, pp. 41–50, 2017.

[6]   G. Kurian, J. E. Miller, J. Psota, *et al.*, "Atac: A 1000-core cache-coherent processor with on-chip optical network", in *Proceedings of the 19th international conference on Parallel architectures and compilation techniques*, 2010, pp. 477–488.

[7]   M. A. I. Sikder, A. K. Kodi, M. Kennedy, S. Kaya, and A. Louri, "Own: Optical and wireless network-on-chip for kilo-core architectures", in *2015 IEEE 23rd Annual Symposium on High-Performance Interconnects*, IEEE, 2015, pp. 44–51.

[8]   D. A. Miller, "Rationale and challenges for optical interconnects to electronic chips", *Proceedings of the IEEE*, vol. 88, no. 6, pp. 728–749, 2000.

[9]   J. W. Goodman, F. J. Leonberger, S.-Y. Kung, and R. A. Athale, "Optical interconnections for vlsi systems", *Proceedings of the IEEE*, vol. 72, no. 7, pp. 850–866, 1984.

[10]   A. V. Krishnamoorthy, "Photonics-to-electronics integration for optical interconnects in the early 21st century", *Optoelectronics letters*, vol. 2, no. 3, pp. 163–168, 2006.

[11]   J. Bashir, E. Peter, and S. R. Sarangi, "A survey of on-chip optical interconnects", *ACM Computing Surveys (CSUR)*, vol. 51, no. 6, pp. 1–34, 2019.

[12]   C. Sun, M. T. Wade, Y. Lee, *et al.*, "Single-chip microprocessor that communicates directly using light", *Nature*, vol. 528, no. 7583, pp. 534–538, 2015.

Bibliography

[13] A. H. Atabaki, S. Moazeni, F. Pavanello, *et al.*, "Integrating photonics with silicon nanoelectronics for the next generation of systems on a chip", *Nature*, vol. 556, no. 7701, pp. 349–354, 2018.

[14] D. A. Miller, "Device requirements for optical interconnects to silicon chips", *Proceedings of the IEEE*, vol. 97, no. 7, pp. 1166–1185, 2009.

[15] A. Pospischil, M. Humer, M. M. Furchi, *et al.*, "Cmos-compatible graphene photodetector covering all optical communication bands", *Nature Photonics*, vol. 7, no. 11, pp. 892–896, 2013.

[16] Y. Salamin, P. Ma, B. Baeuerle, *et al.*, "100 ghz plasmonic photodetector", *ACS photonics*, vol. 5, no. 8, pp. 3291–3297, 2018.

[17] J. Gosciniak, F. B. Atar, B. Corbett, and M. Rasras, "Plasmonic schottky photodetector with metal stripe embedded into semiconductor and with a cmos-compatible titanium nitride", *Scientific reports*, vol. 9, no. 1, p. 6048, 2019.

[18] J. Osmond, G. Isella, D. Chrastina, R. Kaufmann, M. Acciarri, and H. Von Känel, "Ultralow dark current ge/si (100) photodiodes with low thermal budget", *Applied physics letters*, vol. 94, no. 20, 2009.

[19] J. Michel, J. Liu, and L. C. Kimerling, "High-performance ge-on-si photodetectors", *Nature photonics*, vol. 4, no. 8, pp. 527–534, 2010.

[20] C. T. DeRose, D. C. Trotter, W. A. Zortman, *et al.*, "Ultra compact 45 ghz cmos compatible germanium waveguide photodiode with low dark current", *Optics express*, vol. 19, no. 25, pp. 24 897–24 904, 2011.

[21] D. Patel, A. Samani, V. Veerasubramanian, S. Ghosh, and D. V. Plant, "Silicon photonic segmented modulator-based electro-optic dac for 100 gb/s pam-4 generation", *IEEE Photonics Technology Letters*, vol. 27, no. 23, pp. 2433–2436, 2015.

[22] E. Timurdogan, C. M. Sorace-Agaskar, J. Sun, E. Shah Hosseini, A. Biberman, and M. R. Watts, "An ultralow power athermal silicon modulator", *Nature communications*, vol. 5, no. 1, pp. 1–11, 2014.

[23] Y.-H. Kuo, Y. K. Lee, Y. Ge, *et al.*, "Strong quantum-confined stark effect in germanium quantum-well structures on silicon", *Nature*, vol. 437, no. 7063, pp. 1334–1336, 2005.

[24] L. Wu, Y. Zhou, Y. Cai, *et al.*, "Design of a broadband ge1-xsix electro-absorption modulator based on the franz-keldysh effect with thermal tuning", *Optics Express*, vol. 28, no. 5, pp. 7585–7595, 2020.

[25] S. A. Srinivasan, M. Pantouvaki, S. Gupta, *et al.*, "56 gb/s germanium waveguide electro-absorption modulator", *Journal of Lightwave Technology*, vol. 34, no. 2, pp. 419–424, 2015.

[26] D. Leong, M. Harry, K. Reeson, and K. Homewood, "A silicon/iron-disilicide light-emitting diode operating at a wavelength of 1.5 μm", *Nature*, vol. 387, no. 6634, pp. 686–688, 1997.

[27] B. Unlu, M. Ghasemi, S. Yerci, and C. Boztug, "Simultaneous crystallization and strain induction enable light-emitting germanium nano/microbridges for infrared lasers", *ACS Applied Nano Materials*, vol. 5, no. 4, pp. 4700–4709, 2022.

[28] A. Ayan, D. Turkay, B. Unlu, *et al.*, "Strain engineering of germanium nanobeams by electrostatic actuation", *Scientific Reports*, vol. 9, no. 1, p. 4963, 2019.

[29] S. Wirths, D. Buca, and S. Mantl, "Si-ge-sn alloys: From growth to applications", *Progress in crystal growth and characterization of materials*, vol. 62, no. 1, pp. 1–39, 2016.

[30] R. Soref, "Mid-infrared photonics in silicon and germanium", *Nature photonics*, vol. 4, no. 8, pp. 495–497, 2010.

[31] J. Liu, X. Sun, D. Pan, *et al.*, "Tensile-strained, n-type ge as a gain medium for monolithic laser integration on si", *Optics express*, vol. 15, no. 18, pp. 11 272–11 277, 2007.

[32] S. Bao, D. Kim, C. Onwukaeme, *et al.*, "Low-threshold optically pumped lasing in highly strained germanium nanowires", *Nature communications*, vol. 8, no. 1, p. 1845, 2017.

[33] Y. Zhou, Y. Miao, S. Ojo, *et al.*, "Electrically injected gesn lasers on si operating up to 100 k", *Optica*, vol. 7, no. 8, pp. 924–928, 2020.

[34] K. P. Homewood and M. A. Lourenço, "The rise of the gesn laser", *Nature Photonics*, vol. 9, no. 2, pp. 78–79, 2015.

[35] Y. Li, J. Zhang, D. Huang, *et al.*, "Room-temperature continuous-wave lasing from monolayer molybdenum ditelluride integrated with a silicon nanobeam cavity", *Nature nanotechnology*, vol. 12, no. 10, pp. 987–992, 2017.

[36] J. Liu, X. Sun, R. Camacho-Aguilera, L. C. Kimerling, and J. Michel, "Ge-on-si laser operating at room temperature", *Optics letters*, vol. 35, no. 5, pp. 679–681, 2010.

[37] F. Armand Pilon, A. Lyasota, Y.-M. Niquet, *et al.*, "Lasing in strained germanium microbridges", *Nature communications*, vol. 10, no. 1, p. 2724, 2019.

[38] R. E. Camacho-Aguilera, Y. Cai, N. Patel, *et al.*, "An electrically pumped germanium laser", *Optics express*, vol. 20, no. 10, pp. 11 316–11 320, 2012.

[39] P. Minzioni, C. Lacava, T. Tanabe, *et al.*, "Roadmap on all-optical processing", *Journal of Optics*, vol. 21, no. 6, p. 063 001, 2019.

[40] T. Alexoudi, G. T. Kanellos, and N. Pleros, "Optical ram and integrated optical memories: A survey", *Light: Science & Applications*, vol. 9, no. 1, p. 91, 2020.

[41] K. Nozaki, A. Shinya, S. Matsuo, *et al.*, "Ultralow-power all-optical ram based on nanocavities", *Nature Photonics*, vol. 6, no. 4, pp. 248–252, 2012.

[42] E. Kuramochi, K. Nozaki, A. Shinya, *et al.*, "Large-scale integration of wavelength-addressable all-optical memories on a photonic crystal chip", *Nature Photonics*, vol. 8, no. 6, pp. 474–481, 2014.

[43] A. Malacarne, A. Bogoni, and L. Poti, "Erbium–ytterbium-doped fiber-based optical flip-flop", *IEEE Photonics Technology Letters*, vol. 19, no. 12, pp. 904–906, 2007.

[44] G. Berrettini, L. Potì, and A. Bogoni, "Optical dynamic ram for all-optical digital processing", *IEEE Photonics Technology Letters*, vol. 23, no. 11, pp. 685–687, 2011.

[45] X. Li, N. Youngblood, C. Ríos, *et al.*, "Fast and reliable storage using a 5 bit, nonvolatile photonic memory cell", *Optica*, vol. 6, no. 1, pp. 1–6, 2019.

[46] C. Ríos, M. Stegmaier, P. Hosseini, *et al.*, "Integrated all-photonic non-volatile multi-level memory", *Nature photonics*, vol. 9, no. 11, pp. 725–732, 2015.

[47] Y. Shen, N. C. Harris, S. Skirlo, *et al.*, "Deep learning with coherent nanophotonic circuits", *Nature photonics*, vol. 11, no. 7, pp. 441–446, 2017.

[48] J. L. O'brien, "Optical quantum computing", *Science*, vol. 318, no. 5856, pp. 1567–1570, 2007.

[49] A. Savage and R. C. Miller, "Measurements of second harmonic generation of the ruby laser line in piezoelectric crystals", *Applied Optics*, vol. 1, no. 5, pp. 661–664, 1962.

[50] W. E. Torruellas, G. Assanto, B. L. Lawrence, R. A. Fuerst, and G. I. Stegeman, "All-optical switching by spatial walkoff compensation and solitary-wave locking", *Applied physics letters*, vol. 68, no. 11, pp. 1449–1451, 1996.

[51] P. Minzioni, "Nonlinearity compensation in a fiber-optic link by optical phase conjugation", *Fiber and Integrated Optics*, vol. 28, no. 3, pp. 179–209, 2009.

[52] O. Leclerc, B. Lavigne, E. Balmefrezol, *et al.*, "Optical regeneration at 40 gb/s and beyond", *J. Lightwave Technol.*, vol. 21, no. 11, p. 2779, 2003.

[53] D. J. Blumenthal, B.-E. Olsson, G. Rossi, *et al.*, "All-optical label swapping networks and technologies", *Journal of Lightwave Technology*, vol. 18, no. 12, p. 2058, 2000.

[54] D. J. Blumenthal, J. E. Bowers, L. Rau, *et al.*, "Optical signal processing for optical packet switching networks", *IEEE Communications Magazine*, vol. 41, no. 2, S23–S29, 2003.

[55] Y. Zhang, C. Husko, J. Schröder, *et al.*, "Phase-sensitive amplification in silicon photonic crystal waveguides", *Optics letters*, vol. 39, no. 2, pp. 363–366, 2014.

[56] P. Guan, K. M. Røge, M. Lillieholm, *et al.*, "Time lens-based optical fourier transformation for all-optical signal processing of spectrally-efficient data", *Journal of Lightwave Technology*, vol. 35, no. 4, pp. 799–806, 2016.

[57] A. Malacarne, Y. Park, M. Li, S. LaRochelle, and J. Azaña, "Real-time fourier transformation of lightwave spectra and application in optical reflectometry", *Optics Express*, vol. 23, no. 25, pp. 32 516–32 527, 2015.

[58] C. Finot, S. Pitois, and G. Millot, "Regenerative 40? gbit? s wavelength converter based on similariton generation", *Optics letters*, vol. 30, no. 14, pp. 1776–1778, 2005.

[59] J. Dong, X. Zhang, and D. Huang, "A proposal for two-input arbitrary boolean logic gates using single semiconductor optical amplifier by picosecond pulse injection", *Optics Express*, vol. 17, no. 10, pp. 7725–7730, 2009.

[60] S. Kumar, A. E. Willner, D. Gurkan, K. R. Parameswaran, and M. M. Fejer, "All-optical half adder using an soa and a ppln waveguide for signal processing in optical networks", *Optics express*, vol. 14, no. 22, pp. 10 255–10 260, 2006.

[61] L. Li, J. Wu, J. Qiu, *et al.*, "Reconfigurable all-optical logic gate using four-wave mixing (fwm) in hnlf for nrz-polsk signal", *Optics Communications*, vol. 283, no. 19, pp. 3608–3612, 2010.

[62] R. M. Younis, N. F. Areed, and S. S. Obayya, "Fully integrated and and or optical logic gates", *IEEE Photonics Technology Letters*, vol. 26, no. 19, pp. 1900–1903, 2014.

[63] P. Singh, D. K. Tripathi, S. Jaiswal, and H. Dixit, "All-optical logic gates: Designs, classification, and comparison", *Advances in Optical Technologies*, vol. 2014, 2014.

[64] E. A. Fagotto, L. H. Bonani, S. M. Rossi, *et al.*, "Impact of wideband wavelength conversion on the performance of optical networks", *Optics & Laser Technology*, vol. 169, p. 109 948, 2024.

[65] K. Garay-Palmett, H. McGuinness, O. Cohen, *et al.*, "Photon pair-state preparation with tailored spectral properties by spontaneous four-wave mixing in photonic-crystal fiber", *Optics express*, vol. 15, no. 22, pp. 14 870–14 886, 2007.

[66] M. Shi, V. Ribeiro, and A. M. Perego, "Parametric amplification based on intermodal four-wave mixing between different supermodes in coupled-core fibers", *Optics Express*, vol. 31, no. 6, pp. 9760–9768, 2023.

[67] W.-H. Zhang, J.-Y. Peng, E.-Z. Li, *et al.*, "Detection of infrared light through stimulated four-wave mixing process", *Frontiers in Quantum Science and Technology*, vol. 1, p. 984 638, 2022.

[68] C. Dorman, I. Kucukkara, and J. Marangos, "Measurement of high conversion efficiency to 123.6-nm radiation in a four-wave-mixing scheme enhanced by electromagnetically induced transparency", *Physical Review A*, vol. 61, no. 1, p. 013 802, 1999.

[69] S. Hannemann, U. Hollenstein, E.-J. van Duijn, and W. Ubachs, "Production of narrowband tunable extreme-ultraviolet radiation by noncollinear resonance-enhanced four-wave mixing", *Optics letters*, vol. 30, no. 12, pp. 1494–1496, 2005.

[70] R. Mincigrucci, A. Cannizzo, F. Capotondi, *et al.*, "Noncollinear, inelastic four-wave mixing in the extreme ultraviolet", *Optica*, vol. 10, no. 10, pp. 1383–1388, 2023.

[71] A. S. Kowligy, D. D. Hickstein, A. Lind, *et al.*, "Tunable mid-infrared generation via wide-band four-wave mixing in silicon nitride waveguides", *Optics Letters*, vol. 43, no. 17, pp. 4220–4223, 2018.

[72] L. Thevenaz, *Advanced fiber optics: concepts and technology*. EPFL press, 2011.

[73] B. E. Saleh and M. C. Teich, *Fundamentals of photonics*. john Wiley & sons, 2019.

[74] G. Li, R. F. Ando, M. Zeisberger, T. Weiss, and M. A. Schmidt, "Interpreting light guidance in antiresonant and photonic bandgap waveguides and fibers by light scattering: Analytical model and ultra-low guidance", *Optics Express*, vol. 30, no. 2, pp. 2768–2779, 2022.

Bibliography

[75] M. Duguay, Y. Kokubun, T. Koch, and L. Pfeiffer, "Antiresonant reflecting optical waveguides in sio2-si multilayer structures", *Applied Physics Letters*, vol. 49, no. 1, pp. 13–15, 1986.

[76] A. Karadimitrakis, M. Debbah, and A. L. Moustakas, "Optical mimo: Results and analysis", in *2014 11th International Symposium on Wireless Communications Systems (ISWCS)*, IEEE, 2014, pp. 966–970.

[77] G. Ceccato, J. L. Cano, A. Mediavilla, and L. Perregrini, "Controlled excitation of waveguide high-order modes for a simple and accurate monopulse tracking system test bench", *IEEE Transactions on Microwave Theory and Techniques*, vol. 69, no. 2, pp. 1327–1334, 2021.

[78] W. Emkey and C. Jack, "Analysis and evaluation of graded-index fiber lenses", *Journal of Lightwave Technology*, vol. 5, no. 9, pp. 1156–1164, 1987.

[79] M. Feit and J. Fleck, "Light propagation in graded-index optical fibers", *Applied optics*, vol. 17, no. 24, pp. 3990–3998, 1978.

[80] A. Gholami, D. Molin, and P. Sillard, "Compensation of chromatic dispersion by modal dispersion in mmf-and vcsel-based gigabit ethernet transmissions", *IEEE Photonics Technology Letters*, vol. 21, no. 10, pp. 645–647, 2009.

[81] F. Schiappelli, R. Kumar, M. Prasciolu, *et al.*, "Efficient fiber-to-waveguide coupling by a lens on the end of the optical fiber fabricated by focused ion beam milling", *Microelectronic Engineering*, vol. 73, pp. 397–404, 2004.

[82] V. R. Almeida, R. R. Panepucci, and M. Lipson, "Nanotaper for compact mode conversion", *Optics letters*, vol. 28, no. 15, pp. 1302–1304, 2003.

[83] M. Pu, L. Liu, H. Ou, K. Yvind, and J. M. Hvam, "Ultra-low-loss inverted taper coupler for silicon-on-insulator ridge waveguide", *Optics Communications*, vol. 283, no. 19, pp. 3678–3682, 2010.

[84] X. Zhu, G. Li, X. Wang, *et al.*, "Low-loss fiber-to-chip edge coupler for silicon nitride integrated circuits", *Optics Express*, vol. 31, no. 6, pp. 10 525–10 532, 2023.

[85] H. A. Lorentz, *The theory of electrons and its applications to the phenomena of light and radiant heat*. GE Stechert & Company, 1916, vol. 29.

[86] M. E. Marhic, *Fiber optical parametric amplifiers, oscillators and related devices*. Cambridge university press, 2008.

[87] G. Agrawal, *Nonlinear Fiber Optics*. Elsevier Science, 2019.

[88] R. Boyd and D. Prato, *Nonlinear Optics*. Elsevier Science, 2008.

[89] R. Luo, H. Jiang, S. Rogers, H. Liang, Y. He, and Q. Lin, "On-chip second-harmonic generation and broadband parametric down-conversion in a lithium niobate microresonator", *Optics express*, vol. 25, no. 20, pp. 24 531–24 539, 2017.

[90] J. Lin, Y. Xu, J. Ni, *et al.*, "Phase-matched second-harmonic generation in an on-chip l i nbo 3 microresonator", *Physical Review Applied*, vol. 6, no. 1, p. 014 002, 2016.

[91] M. Jankowski, C. Langrock, B. Desiatov, *et al.*, "Ultrabroadband nonlinear optics in nanophotonic periodically poled lithium niobate waveguides", *Optica*, vol. 7, no. 1, pp. 40–46, 2020.

[92] S. Yamada, B.-S. Song, S. Jeon, *et al.*, "Second-harmonic generation in a silicon-carbide-based photonic crystal nanocavity", *Optics letters*, vol. 39, no. 7, pp. 1768–1771, 2014.

[93] H. Sato, M. Abe, I. Shoji, J. Suda, and T. Kondo, "Accurate measurements of second-order nonlinear optical coefficients of 6h and 4h silicon carbide", *JOSA B*, vol. 26, no. 10, pp. 1892–1896, 2009.

[94] P. Lundquist, W. Lin, G. Wong, M. Razeghi, and J. Ketterson, "Second harmonic generation in hexagonal silicon carbide", *Applied physics letters*, vol. 66, no. 15, pp. 1883–1885, 1995.

[95] I. Roland, M. Gromovyi, Y. Zeng, *et al.*, "Phase-matched second harmonic generation with on-chip gan-on-si microdisks", *Scientific reports*, vol. 6, no. 1, p. 34 191, 2016.

[96] J. F. Reintjes, "Nonlinear optical processes", 2003.

[97] R. Tkach, A. Chraplyvy, F. Forghieri, A. Gnauck, and R. Derosier, "Four-photon mixing and high-speed wdm systems", *Journal of Lightwave Technology*, vol. 13, no. 5, pp. 841–849, 1995.

[98] P. Maker and R. Terhune, "Study of optical effects due to an induced polarization third order in the electric field strength", *Physical Review*, vol. 137, no. 3A, A801, 1965.

[99] M. Guasoni, F. Parmigiani, P. Horak, J. Fatome, and D. J. Richardson, "Intermodal four-wave mixing and parametric amplification in kilometer-long multimode fibers", *Journal of Lightwave Technology*, vol. 35, no. 24, pp. 5296–5305, 2017.

[100] T. Torounidis, P. A. Andrekson, and B.-E. Olsson, "Fiber-optical parametric amplifier with 70-db gain", *IEEE Photonics Technology Letters*, vol. 18, no. 10, pp. 1194–1196, 2006.

[101] A. Gershikov, E. Shumakher, A. Willinger, and G. Eisenstein, "Fiber parametric oscillator for the 2 μm wavelength range based on narrowband optical parametric amplification", *Optics letters*, vol. 35, no. 19, pp. 3198–3200, 2010.

[102] A. Mussot, A. Durecu-Legrand, E. Lantz, *et al.*, "Impact of pump phase modulation on the gain of fiber optical parametric amplifier", *IEEE Photonics Technology Letters*, vol. 16, no. 5, pp. 1289–1291, 2004.

[103] T. Cheng, L. Zhang, X. Xue, D. Deng, T. Suzuki, and Y. Ohishi, "Broadband cascaded four-wave mixing and supercontinuum generation in a tellurite microstructured optical fiber pumped at 2 μm", *Optics Express*, vol. 23, no. 4, pp. 4125–4134, 2015.

[104] S. Xing, D. Grassani, S. Kharitonov, *et al.*, "Mid-infrared continuous-wave parametric amplification in chalcogenide microstructured fibers", *Optica*, vol. 4, no. 6, pp. 643–648, 2017.

[105] J. E. Sharping, M. Fiorentino, A. Coker, P. Kumar, and R. S. Windeler, "Four-wave mixing in microstructure fiber", *Optics letters*, vol. 26, no. 14, pp. 1048–1050, 2001.

Bibliography

[106] M. Marhic, N. Kagi, T.-K. Chiang, and L. Kazovsky, "Broadband fiber optical parametric amplifiers", *Optics letters*, vol. 21, no. 8, pp. 573–575, 1996.

[107] C. J. McKinstrie and M. G. Raymer, "Four-wave-mixing cascades near the zero-dispersion frequency", *Optics express*, vol. 14, no. 21, pp. 9600–9610, 2006.

[108] O. F. Anjum, M. Guasoni, P. Horak, *et al.*, "Polarization-insensitive four-wave-mixing-based wavelength conversion in few-mode optical fibers", *Journal of Lightwave Technology*, vol. 36, no. 17, pp. 3678–3683, 2018.

[109] A. S. Raja, A. S. Voloshin, H. Guo, *et al.*, "Electrically pumped photonic integrated soliton microcomb", *Nature communications*, vol. 10, no. 1, p. 680, 2019.

[110] A. G. Griffith, R. K. Lau, J. Cardenas, *et al.*, "Silicon-chip mid-infrared frequency comb generation", *Nature communications*, vol. 6, no. 1, p. 6299, 2015.

[111] Y. Hu, M. Yu, B. Buscaino, *et al.*, "High-efficiency and broadband on-chip electro-optic frequency comb generators", *Nature Photonics*, vol. 16, no. 10, pp. 679–685, 2022.

[112] S. Miller, K. Luke, Y. Okawachi, J. Cardenas, A. L. Gaeta, and M. Lipson, "On-chip frequency comb generation at visible wavelengths via simultaneous second-and third-order optical nonlinearities", *Optics Express*, vol. 22, no. 22, pp. 26 517–26 525, 2014.

[113] H. Jung and H. X. Tang, "Aluminum nitride as nonlinear optical material for on-chip frequency comb generation and frequency conversion", *Nanophotonics*, vol. 5, no. 2, pp. 263–271, 2016.

[114] M. Borghi, A. Trenti, and L. Pavesi, "Four wave mixing control in a photonic molecule made by silicon microring resonators", *Scientific reports*, vol. 9, no. 1, p. 408, 2019.

[115] Y. Zhang, J. Wu, Y. Qu, L. Jia, B. Jia, and D. J. Moss, "Design and optimization of four-wave mixing in microring resonators integrated with 2d graphene oxide films", *Journal of Lightwave Technology*, vol. 39, no. 20, pp. 6553–6562, 2021.

[116] M. Ferrera, D. Duchesne, L. Razzari, *et al.*, "Low power four wave mixing in an integrated, micro-ring resonator with q= 1.2 million", *Optics express*, vol. 17, no. 16, pp. 14 098–14 103, 2009.

[117] B. Little, "A vlsi photonics platform", in *Optical Fiber Communication Conference*, Optica Publishing Group, 2003, ThD1.

[118] A. Pasquazi, Y. Park, J. Azaña, *et al.*, "Efficient wavelength conversion and net parametric gain via four wave mixing in a high index doped silica waveguide", *Optics express*, vol. 18, no. 8, pp. 7634–7641, 2010.

[119] M. Ferrera, L. Razzari, D. Duchesne, *et al.*, "Low-power continuous-wave nonlinear optics in doped silica glass integrated waveguide structures", *Nature photonics*, vol. 2, no. 12, pp. 737–740, 2008.

[120] D. Duchesne, M. Ferrera, L. Razzari, *et al.*, "Efficient self-phase modulation in low loss, high index doped silica glass integrated waveguides", *Optics Express*, vol. 17, no. 3, pp. 1865–1870, 2009.

[121] D. J. Moss, A. Pasquazi, M. Peccianti, *et al.*, "Hydex waveguides for nonlinear optics", *arXiv preprint arXiv:1404.7619*, 2014.

[122] M. Peccianti, M. Ferrera, L. Razzari, *et al.*, "Subpicosecond optical pulse compression via an integrated nonlinear chirper", *Optics Express*, vol. 18, no. 8, pp. 7625–7633, 2010.

[123] L. Tong, R. R. Gattass, J. B. Ashcom, *et al.*, "Subwavelength-diameter silica wires for low-loss optical wave guiding", *Nature*, vol. 426, no. 6968, pp. 816–819, 2003.

[124] R. Salem, M. A. Foster, A. C. Turner, D. F. Geraghty, M. Lipson, and A. L. Gaeta, "Signal regeneration using low-power four-wave mixing on silicon chip", *Nature photonics*, vol. 2, no. 1, pp. 35–38, 2008.

[125] M. A. Foster, A. C. Turner, J. E. Sharping, B. S. Schmidt, M. Lipson, and A. L. Gaeta, "Broad-band optical parametric gain on a silicon photonic chip", *Nature*, vol. 441, no. 7096, pp. 960–963, 2006.

[126] A. C. Turner-Foster, M. A. Foster, R. Salem, A. L. Gaeta, and M. Lipson, "Frequency conversion over two-thirds of an octave in silicon nanowaveguides", *Optics express*, vol. 18, no. 3, pp. 1904–1908, 2010.

[127] A. C. Turner, M. A. Foster, A. L. Gaeta, and M. Lipson, "Ultra-low power parametric frequency conversion in a silicon microring resonator", *Optics express*, vol. 16, no. 7, pp. 4881–4887, 2008.

[128] A. Gajda, L. Zimmermann, M. Jazayerifar, *et al.*, "Highly efficient cw parametric conversion at 1550 nm in soi waveguides by reverse biased pin junction", *Optics express*, vol. 20, no. 12, pp. 13 100–13 107, 2012.

[129] W. Mathlouthi, H. Rong, and M. Paniccia, "Characterization of efficient wavelength conversion by four-wave mixing in sub-micron silicon waveguides", *Optics express*, vol. 16, no. 21, pp. 16 735–16 745, 2008.

[130] M. Ettabib, C. Lacava, Z. Liu, *et al.*, "Wavelength conversion of complex modulation formats in a compact sige waveguide", *Optics express*, vol. 25, no. 4, pp. 3252–3258, 2017.

[131] K. Hammani, M. A. Ettabib, A. Bogris, *et al.*, "Optical properties of silicon germanium waveguides at telecommunication wavelengths", *Optics express*, vol. 21, no. 14, pp. 16 690–16 701, 2013.

[132] K.-Y. Wang and A. C. Foster, "Ultralow power continuous-wave frequency conversion in hydrogenated amorphous silicon waveguides", *Optics letters*, vol. 37, no. 8, pp. 1331–1333, 2012.

[133] P. Xing, D. Ma, K. J. Ooi, J. W. Choi, A. M. Agarwal, and D. Tan, "Cmos-compatible pecvd silicon carbide platform for linear and nonlinear optics", *ACS Photonics*, vol. 6, no. 5, pp. 1162–1167, 2019.

[134] P. Xing, D. Ma, L. C. Kimerling, A. M. Agarwal, and D. T. Tan, "High efficiency four wave mixing and optical bistability in amorphous silicon carbide ring resonators", *APL Photonics*, vol. 5, no. 7, 2020.

[135] A. Yi, Y. Zheng, H. Huang, *et al.*, "Wafer-scale 4h-silicon carbide-on-insulator (4h–sicoi) platform for nonlinear integrated optical devices", *Optical Materials*, vol. 107, p. 109 990, 2020.

[136] X. Gai, S. Madden, D.-Y. Choi, D. Bulla, and B. Luther-Davies, "Dispersion engineered ge11.5as24se64.5 nanowires with a nonlinear parameter of 136w- 1 m- 1 at 1550nm", *Optics express*, vol. 18, no. 18, pp. 18 866–18 874, 2010.

[137] X. Gai, T. Han, A. Prasad, *et al.*, "Progress in optical waveguides fabricated from chalcogenide glasses", *Optics express*, vol. 18, no. 25, pp. 26 635–26 646, 2010.

[138] S. Madden, D.-Y. Choi, D. Bulla, *et al.*, "Long, low loss etched as2s3 chalcogenide waveguides for all-optical signal regeneration", *Optics express*, vol. 15, no. 22, pp. 14 414–14 421, 2007.

[139] S. Serna, H. Lin, C. Alonso-Ramos, *et al.*, "Nonlinear optical properties of integrated gesbs chalcogenide waveguides", *Photonics research*, vol. 6, no. 5, B37–B42, 2018.

[140] D.-I. Yeom, E. C. Mägi, M. R. Lamont, M. A. Roelens, L. Fu, and B. J. Eggleton, "Low-threshold supercontinuum generation in highly nonlinear chalcogenide nanowires", *Optics letters*, vol. 33, no. 7, pp. 660–662, 2008.

[141] Y. Ruan, B. Luther-Davies, W. Li, A. Rode, V. Kolev, and S. Madden, "Large phase shifts in as2s3 waveguides for all-optical processing devices", *Optics letters*, vol. 30, no. 19, pp. 2605–2607, 2005.

[142] B. J. Eggleton, B. Luther-Davies, and K. Richardson, "Chalcogenide photonics", *Nature photonics*, vol. 5, no. 3, pp. 141–148, 2011.

[143] N. Ashok, Y. L. Lee, and W. Shin, "Chalcogenide waveguide structure for dispersion in mid-infrared wavelength", *Japanese Journal of Applied Physics*, vol. 56, no. 3, p. 032 501, 2017.

[144] H. G. Dantanarayana, N. Abdel-Moneim, Z. Tang, *et al.*, "Refractive index dispersion of chalcogenide glasses for ultra-high numerical-aperture fiber for mid-infrared supercontinuum generation", *Optical Materials Express*, vol. 4, no. 7, pp. 1444–1455, 2014.

[145] B. Amin, I. Ahmad, M. Maqbool, S. Goumri-Said, and R. Ahmad, "Ab initio study of the bandgap engineering of al1- xgaxn for optoelectronic applications", *Journal of Applied Physics*, vol. 109, no. 2, 2011.

[146] K. Vyas, D. H. Espinosa, D. Hutama, *et al.*, "Group iii-v semiconductors as promising nonlinear integrated photonic platforms", *Advances in Physics: X*, vol. 7, no. 1, p. 2 097 020, 2022.

[147] F. Saouma, C. Stoumpos, J. Wong, M. Kanatzidis, and J. Jang, "Selective enhancement of optical nonlinearity in two-dimensional organic-inorganic lead iodide perovskites", *Nature communications*, vol. 8, no. 1, p. 742, 2017.

[148] C. Lacava, V. Pusino, P. Minzioni, M. Sorel, and I. Cristiani, "Nonlinear properties of algaas waveguides in continuous wave operation regime", *Optics Express*, vol. 22, no. 5, pp. 5291–5298, 2014.

[149] J. J. Wathen, P. Apiratikul, C. J. Richardson, G. A. Porkolab, G. M. Carter, and T. E. Murphy, "Efficient continuous-wave four-wave mixing in bandgap-engineered algaas waveguides", *Optics letters*, vol. 39, no. 11, pp. 3161–3164, 2014.

[150] E. Stassen, C. Kim, D. Kong, *et al.*, "Ultra-low power all-optical wavelength conversion of high-speed data signals in high-confinement algaas-on-insulator microresonators", *Apl Photonics*, vol. 4, no. 10, 2019.

[151] P. M. Kaminski, F. Da Ros, E. P. da Silva, *et al.*, "Characterization and optimization of four-wave-mixing wavelength conversion system", *Journal of Lightwave Technology*, vol. 37, no. 21, pp. 5628–5636, 2019.

[152] V. Eckhouse, I. Cestier, G. Eisenstein, *et al.*, "Highly efficient four wave mixing in gainp photonic crystal waveguides", *Optics letters*, vol. 35, no. 9, pp. 1440–1442, 2010.

[153] U. D. Dave, B. Kuyken, F. Leo, *et al.*, "Nonlinear properties of dispersion engineered ingap photonic wire waveguides in the telecommunication wavelength range", *Optics express*, vol. 23, no. 4, pp. 4650–4657, 2015.

[154] P. Apiratikul, J. J. Wathen, G. A. Porkolab, *et al.*, "Enhanced continuous-wave four-wave mixing efficiency in nonlinear algaas waveguides", *Optics express*, vol. 22, no. 22, pp. 26 814–26 824, 2014.

[155] M. Pu, H. Hu, L. Ottaviano, *et al.*, "Ultra-efficient and broadband nonlinear algaas-on-insulator chip for low-power optical signal processing", *Laser & Photonics Reviews*, vol. 12, no. 12, p. 1 800 111, 2018.

[156] E. Stassen, M. Pu, E. Semenova, E. Zavarin, W. Lundin, and K. Yvind, "High-confinement gallium nitride-on-sapphire waveguides for integrated nonlinear photonics", *Optics letters*, vol. 44, no. 5, pp. 1064–1067, 2019.

[157] D. J. Moss, R. Morandotti, A. L. Gaeta, and M. Lipson, "New cmos-compatible platforms based on silicon nitride and hydex for nonlinear optics", *Nature photonics*, vol. 7, no. 8, pp. 597–607, 2013.

[158] K. Ikeda, R. E. Saperstein, N. Alic, and Y. Fainman, "Thermal and kerr nonlinear properties of plasma-deposited silicon nitride/silicon dioxide waveguides", *Optics express*, vol. 16, no. 17, pp. 12 987–12 994, 2008.

[159] C. H. Henry, R. F. Kazarinov, H. J. Lee, K. J. Orlowsky, and L. Katz, "Low loss si3n4–sio2 optical waveguides on si", *Applied optics*, vol. 26, no. 13, pp. 2621–2624, 1987.

[160] J. F. Bauters, M. J. Heck, D. D. John, *et al.*, "Planar waveguides with less than 0.1 db/m propagation loss fabricated with wafer bonding", *Optics express*, vol. 19, no. 24, pp. 24 090–24 101, 2011.

[161] D. Tan, K. Ikeda, P. Sun, and Y. Fainman, "Group velocity dispersion and self phase modulation in silicon nitride waveguides", *Applied Physics Letters*, vol. 96, no. 6, 2010.

Bibliography

[162] J. S. Levy, A. Gondarenko, M. A. Foster, A. C. Turner-Foster, A. L. Gaeta, and M. Lipson, "Cmos-compatible multiple-wavelength oscillator for on-chip optical interconnects", *Nature photonics*, vol. 4, no. 1, pp. 37–40, 2010.

[163] C. J. Krückel, P. A. Andrekson, D. T. Spencer, J. F. Bauters, M. J. Heck, J. E. Bowers, *et al.*, "Continuous wave-pumped wavelength conversion in low-loss silicon nitride waveguides", *Optics letters*, vol. 40, no. 6, pp. 875–878, 2015.

[164] D. K. Ng, Q. Wang, T. Wang, *et al.*, "Exploring high refractive index silicon-rich nitride films by low-temperature inductively coupled plasma chemical vapor deposition and applications for integrated waveguides", *ACS applied materials & interfaces*, vol. 7, no. 39, pp. 21 884–21 889, 2015.

[165] H. Mertens, K. N. Andersen, and W. E. Svendsen, "Optical loss analysis of silicon rich nitride waveguides", in *2002 28TH European Conference on Optical Communication*, IEEE, vol. 3, 2002, pp. 1–2.

[166] H. T. Philipp, K. N. Andersen, W. Svendsen, and H. Ou, "Amorphous silicon rich silicon nitride optical waveguides for high density integrated optics", *Electronics Letters*, vol. 40, no. 7, p. 1, 2004.

[167] T. Barwicz, M. A. Popovic, P. T. Rakich, *et al.*, "Microring-resonator-based add-drop filters in sin: Fabrication and analysis", *Optics express*, vol. 12, no. 7, pp. 1437–1442, 2004.

[168] C. J. Krückel, A. Fülöp, T. Klintberg, J. Bengtsson, P. A. Andrekson, *et al.*, "Linear and nonlinear characterization of low-stress high-confinement silicon-rich nitride waveguides", *Optics express*, vol. 23, no. 20, pp. 25 827–25 837, 2015.

[169] C.-L. Wu, Y.-H. Lin, S.-P. Su, *et al.*, "Enhancing optical nonlinearity in a nonstoichiometric sin waveguide for cross-wavelength all-optical data processing", *Acs Photonics*, vol. 2, no. 8, pp. 1141–1154, 2015.

[170] M. Mitrovic, X. Guan, H. Ji, L. K. Oxenløwe, and L. H. Frandsen, "Four-wave mixing in silicon-rich nitride waveguides", in *Frontiers in Optics*, Optica Publishing Group, 2015, FM1D–6.

[171] T. Wang, D. K. Ng, S.-K. Ng, *et al.*, "Supercontinuum generation in bandgap engineered, back-end cmos compatible silicon rich nitride waveguides", *Laser & Photonics Reviews*, vol. 9, no. 5, pp. 498–506, 2015.

[172] C. Lacava, S. Stankovic, A. Z. Khokhar, *et al.*, "Si-rich silicon nitride for nonlinear signal processing applications", *Scientific reports*, vol. 7, no. 1, p. 22, 2017.

[173] K. Ooi, D. Ng, T. Wang, *et al.*, "Pushing the limits of cmos optical parametric amplifiers with usrn: Si7n3 above the two-photon absorption edge", *Nature communications*, vol. 8, no. 1, p. 13 878, 2017.

[174] X. Ji, X. Yao, Y. Gan, *et al.*, "On-chip tunable photonic delay line", *APL Photonics*, vol. 4, no. 9, 2019.

[175] C. Xiang, W. Jin, and J. E. Bowers, "Silicon nitride passive and active photonic integrated circuits: Trends and prospects", *Photonics Research*, vol. 10, no. 6, A82–A96, 2022.

[176] N. M. Lüpken, T. Würthwein, K.-J. Boller, and C. Fallnich, "Optical parametric amplification in silicon nitride waveguides for coherent raman imaging", *Optics express*, vol. 29, no. 7, pp. 10 424–10 433, 2021.

[177] J. Liu, E. Lucas, A. S. Raja, *et al.*, "Photonic microwave generation in the x-and k-band using integrated soliton microcombs", *Nature Photonics*, vol. 14, no. 8, pp. 486–491, 2020.

[178] X. Ji, J. K. Jang, U. D. Dave, *et al.*, "Exploiting ultralow loss multimode waveguides for broadband frequency combs", *Laser & Photonics Reviews*, vol. 15, no. 1, p. 2 000 353, 2021.

[179] Z. Ye, H. Jia, Z. Huang, *et al.*, "Foundry manufacturing of tight-confinement, dispersion-engineered, ultralow-loss silicon nitride photonic integrated circuits", *Photonics Research*, vol. 11, no. 4, pp. 558–568, 2023.

[180] D. T. Spencer, J. F. Bauters, M. J. Heck, and J. E. Bowers, "Integrated waveguide coupled si 3 n 4 resonators in the ultrahigh-q regime", *Optica*, vol. 1, no. 3, pp. 153–157, 2014.

[181] D. Bose, J. Wang, and D. J. Blumenthal, "250c process for< 2db/m ultra-low loss silicon nitride integrated photonic waveguides", in *CLEO: Science and Innovations*, Optica Publishing Group, 2022, SF3O–1.

[182] M. H. Pfeiffer, A. Kordts, V. Brasch, *et al.*, "Photonic damascene process for integrated high-q microresonator based nonlinear photonics", *Optica*, vol. 3, no. 1, pp. 20–25, 2016.

[183] M. W. Puckett, K. Liu, N. Chauhan, *et al.*, "422 million intrinsic quality factor planar integrated all-waveguide resonator with sub-mhz linewidth", *Nature communications*, vol. 12, no. 1, p. 934, 2021.

[184] Q. Li, A. A. Eftekhar, M. Sodagar, Z. Xia, A. H. Atabaki, and A. Adibi, "Vertical integration of high-q silicon nitride microresonators into silicon-on-insulator platform", *Optics express*, vol. 21, no. 15, pp. 18 236–18 248, 2013.

[185] M. Gao, Q.-F. Yang, Q.-X. Ji, *et al.*, "Probing material absorption and optical nonlinearity of integrated photonic materials", *Nature Communications*, vol. 13, no. 1, p. 3323, 2022.

[186] Z. Ye, K. Twayana, P. A. Andrekson, *et al.*, "High-q si3n4 microresonators based on a subtractive processing for kerr nonlinear optics", *Optics express*, vol. 27, no. 24, pp. 35 719–35 727, 2019.

[187] Z. Ye, P. Zhao, K. Twayana, M. Karlsson, P. A. Andrekson, and V. Torres-Company, "Ultralow-loss meter-long dispersion-engineered silicon nitride waveguides", in *2021 Conference on Lasers and Electro-Optics (CLEO)*, IEEE, 2021, pp. 1–2.

[188] J. Liu, G. Huang, R. N. Wang, *et al.*, "High-yield, wafer-scale fabrication of ultralow-loss, dispersion-engineered silicon nitride photonic circuits", *Nature communications*, vol. 12, no. 1, p. 2236, 2021.

Bibliography

[189] Z. Ye, P. Zhao, K. Twayana, M. Karlsson, V. Torres-Company, and P. A. Andrekson, "Overcoming the quantum limit of optical amplification in monolithic waveguides", *Science advances*, vol. 7, no. 38, eabi8150, 2021.

[190] J. Riemensberger, N. Kuznetsov, J. Liu, J. He, R. N. Wang, and T. J. Kippenberg, "A photonic integrated continuous-travelling-wave parametric amplifier", *Nature*, vol. 612, no. 7938, pp. 56–61, 2022.

[191] P. Zhao, M. Karlsson, and P. A. Andrekson, "Low-noise integrated phase-sensitive waveguide parametric amplifiers", *Journal of Lightwave Technology*, vol. 40, no. 1, pp. 128–135, 2022.

[192] J. Wang, Y. Yu, Y.-M. Wei, *et al.*, "High-efficiency broadband second harmonic generation in single hexagonal gaas nanowire", *Scientific reports*, vol. 7, no. 1, p. 2166, 2017.

[193] X. Zhang, H. He, J. Fan, *et al.*, "Sum frequency generation in pure zinc-blende gaas nanowires", *Optics Express*, vol. 21, no. 23, pp. 28 432–28 437, 2013.

[194] A. Andronico, I. Favero, and G. Leo, "Difference frequency generation in gaas microdisks", *Optics letters*, vol. 33, no. 18, pp. 2026–2028, 2008.

[195] X. Lu, G. Moille, A. Rao, D. A. Westly, and K. Srinivasan, "Efficient photoinduced second-harmonic generation in silicon nitride photonics", *Nature Photonics*, vol. 15, no. 2, pp. 131–136, 2021.

[196] D. D. Hickstein, D. R. Carlson, H. Mundoor, *et al.*, "Self-organized nonlinear gratings for ultrafast nanophotonics", *Nature Photonics*, vol. 13, no. 7, pp. 494–499, 2019.

[197] A. Billat, D. Grassani, M. H. Pfeiffer, S. Kharitonov, T. J. Kippenberg, and C.-S. Brès, "Large second harmonic generation enhancement in si3n4 waveguides by all-optically induced quasi-phase-matching", *Nature communications*, vol. 8, no. 1, p. 1016, 2017.

[198] O. Yakar, E. Nitiss, J. Hu, and C.-S. Brès, "Integrated backward second-harmonic generation through optically induced quasi-phase-matching", *Phys. Rev. Lett.*, vol. 131, p. 143 802, 14 2023. DOI: 10.1103/PhysRevLett.131.143802.

[199] O. Yakar, E. Nitiss, J. Hu, and C.-S. Brès, "Generalized coherent photogalvanic effect in coherently seeded waveguides", *Laser & Photonics Reviews*, vol. 16, no. 12, p. 2 200 294, 2022.

[200] E. Sahin, B. Zabelich, O. Yakar, *et al.*, "Difference-frequency generation in optically poled silicon nitride waveguides", *Nanophotonics*, vol. 10, no. 7, pp. 1923–1930, 2021.

[201] R. Dalidet, F. Mazeas, E. Nitiss, *et al.*, "Near perfect two-photon interference out of a down-converter on a silicon photonic chip", *Optics Express*, vol. 30, no. 7, pp. 11 298–11 305, 2022.

[202] I. Agha, M. Davanço, B. Thurston, and K. Srinivasan, "Low-noise chip-based frequency conversion by four-wave-mixing bragg scattering in sin x waveguides", *Optics letters*, vol. 37, no. 14, pp. 2997–2999, 2012.

[203] Z. Tu, D. Chen, H. Hu, S. Gao, and X. Guan, "Characterization and optimal design of silicon-rich nitride nonlinear waveguides for 2 μm wavelength band", *Applied Sciences*, vol. 10, no. 22, p. 8087, 2020.

[204] K. Wörhoff, R. G. Heideman, A. Leinse, and M. Hoekman, "Triplex: A versatile dielectric photonic platform", *Advanced Optical Technologies*, vol. 4, no. 2, pp. 189–207, 2015.

[205] Y. Wang, V. Pelgrin, S. Gyger, *et al.*, "Enhancing si3n4 waveguide nonlinearity with heterogeneous integration of few-layer ws2", *ACS photonics*, vol. 8, no. 9, pp. 2713–2721, 2021.

[206] P. Demongodin, H. El Dirani, S. Kerdilès, *et al.*, "Pulsed four-wave mixing at telecom wavelengths in si3n4 waveguides locally covered by graphene", *Nanomaterials*, vol. 13, no. 3, p. 451, 2023.

[207] Y. Qu, J. Wu, Y. Yang, *et al.*, "Enhanced four-wave mixing in silicon nitride waveguides integrated with 2d layered graphene oxide films", *Advanced Optical Materials*, vol. 8, no. 23, p. 2 001 048, 2020.

[208] J. Goell, "Rib waveguide for integrated optical circuits", *Applied optics*, vol. 12, no. 12, pp. 2797–2798, 1973.

[209] J. Jackel and J. Johnson, "Reverse exchange method for burying proton exchanged waveguides", *Electronics Letters*, vol. 27, pp. 1360–1361, 1991. DOI: 10.1049/EL:19910856.

[210] M. H. Pfeiffer, J. Liu, A. S. Raja, T. Morais, B. Ghadiani, and T. J. Kippenberg, "Ultra-smooth silicon nitride waveguides based on the damascene reflow process: Fabrication and loss origins", *Optica*, vol. 5, no. 7, pp. 884–892, 2018.

[211] X. Ji, F. A. Barbosa, S. P. Roberts, *et al.*, "Ultra-low-loss on-chip resonators with sub-milliwatt parametric oscillation threshold", *Optica*, vol. 4, no. 6, pp. 619–624, 2017.

[212] Y. Xuan, Y. Liu, L. T. Varghese, *et al.*, "High-q silicon nitride microresonators exhibiting low-power frequency comb initiation", *Optica*, vol. 3, no. 11, pp. 1171–1180, 2016.

[213] J. Liu, A. S. Raja, M. Karpov, *et al.*, "Ultralow-power chip-based soliton microcombs for photonic integration", *Optica*, vol. 5, no. 10, pp. 1347–1353, 2018.

[214] M. A. Foster, K. D. Moll, and A. L. Gaeta, "Optimal waveguide dimensions for nonlinear interactions", *Optics Express*, vol. 12, no. 13, pp. 2880–2887, 2004.

[215] C. J. Krückel, A. Fülöp, Z. Ye, P. A. Andrekson, *et al.*, "Optical bandgap engineering in nonlinear silicon nitride waveguides", *Optics express*, vol. 25, no. 13, pp. 15 370–15 380, 2017.

[216] R. Dupiol, A. Bendahmane, K. Krupa, *et al.*, "Far-detuned cascaded intermodal four-wave mixing in a multimode fiber", *Optics Letters*, vol. 42, no. 7, pp. 1293–1296, 2017.

[217] S. Signorini, M. Mancinelli, M. Borghi, *et al.*, "Intermodal four wave mixing in silicon waveguides for on-chip wavelength conversion and generation (conference presentation)", in *Nonlinear Optics and its Applications 2018*, SPIE, vol. 10684, 2018, p. 1 068 407.

Bibliography

[218] G. Roelkens, D. Vermeulen, F. Van Laere, *et al.*, "Bridging the gap between nanophotonic waveguide circuits and single mode optical fibers using diffractive grating structures", *Journal of nanoscience and nanotechnology*, vol. 10, no. 3, pp. 1551–1562, 2010.

[219] Z. Lu and D. W. Prather, "Total internal reflection–evanescent coupler for fiber-to-waveguide integration of planar optoelectric devices", *Optics letters*, vol. 29, no. 15, pp. 1748–1750, 2004.

[220] A. Delage, S. Janz, D. X. Xu, D. Dalacu, B. Lamontagne, and A. L. Bogdanov, "Graded-index coupler for microphotonic soi waveguides", in *Photonics North 2004: Optical Components and Devices*, SPIE, vol. 5577, 2004, pp. 204–212.

[221] K. K. Lee, D. R. Lim, D. Pan, *et al.*, "Mode transformer for miniaturized optical circuits", *Optics letters*, vol. 30, no. 5, pp. 498–500, 2005.

[222] G. Ren, S. Chen, Y. Cheng, and Y. Zhai, "Study on inverse taper based mode transformer for low loss coupling between silicon wire waveguide and lensed fiber", *Optics Communications*, vol. 284, no. 19, pp. 4782–4788, 2011.

[223] Y. Wu and K. S. Chiang, "Mode-selective coupling between few-mode fibers and buried channel waveguides", *Optics Express*, vol. 24, no. 26, pp. 30 108–30 123, 2016.

[224] X. Yi, C. Li, W. Zhao, L. Zhang, Y. Shi, and D. Dai, "On-chip mode-selective manipulation based on the modal-field redistribution assisted with subwavelength grating structures", *Nanophotonics*, vol. 12, no. 9, pp. 1809–1821, 2023.

[225] D. Runde, S. Breuer, and D. Kip, "Mode-selective coupler for wavelength multiplexing using linbo 3: Ti optical waveguides", *Central European Journal of Physics*, vol. 6, pp. 588–592, 2008.

[226] W. D. Sacher, Y. Huang, L. Ding, *et al.*, "Wide bandwidth and high coupling efficiency si 3 n 4-on-soi dual-level grating coupler", *Optics express*, vol. 22, no. 9, pp. 10 938–10 947, 2014.

[227] J. Fernández, R. Baños, D. Doménech, C. Domínguez, and P. Muñoz, "Low-loss inverted taper edge coupler in silicon nitride", *IET Optoelectronics*, vol. 13, no. 2, pp. 62–66, 2019.

[228] C. Ozcan, J. S. Aitchison, and M. Mojahedi, "Adiabatic waveguide taper profile optimization on al2o3/si platform for polarization insensitive fiber-to-chip light coupling", in *The European Conference on Lasers and Electro-Optics*, Optica Publishing Group, 2021, ck_p_4.

[229] A. Billat, S. Cordette, Y.-P. Tseng, S. Kharitonov, and C.-S. Brès, "High-power parametric conversion from near-infrared to short-wave infrared", *Optics Express*, vol. 22, no. 12, pp. 14 341–14 347, 2014.

[230] P. T. Lin, V. Singh, H.-Y. G. Lin, T. Tiwald, L. C. Kimerling, and A. M. Agarwal, "Low-stress silicon nitride platform for mid-infrared broadband and monolithically integrated microphotonics", *Advanced Optical Materials*, vol. 1, no. 10, pp. 732–739, 2013.

[231] H. Lin, Z. Luo, T. Gu, *et al.*, "Mid-infrared integrated photonics on silicon: A perspective", *Nanophotonics*, vol. 7, no. 2, pp. 393–420, 2017.

[232] B. J. de Aragão and Y. Messaddeq, "Peak separation by derivative spectroscopy applied to ftir analysis of hydrolyzed silica", *Journal of the Brazilian chemical Society*, vol. 19, pp. 1582–1594, 2008.

[233] R. Kitamura, L. Pilon, and M. Jonasz, "Optical constants of silica glass from extreme ultraviolet to far infrared at near room temperature", *Applied optics*, vol. 46, no. 33, pp. 8118–8133, 2007.

[234] S. Watanabe, S. Takeda, and T. Chikama, "Interband wavelength conversion of 320 gb/s (32/spl times/10 gb/s) wdm signal using a polarization-insensitive fiber four-wave mixer", in *24th European Conference on Optical Communication. ECOC'98 (IEEE Cat. No. 98TH8398)*, IEEE, vol. 3, 1998, pp. 83–87.

[235] K. K. Wong, M. E. Marhic, K. Uesaka, and L. G. Kazovsky, "Polarization-independent one-pump fiber-optical parametric amplifier", *IEEE Photonics Technology Letters*, vol. 14, no. 11, pp. 1506–1508, 2002.

[236] T. Hasegawa, K. Inoue, and K. Oda, "Polarization independent frequency conversion by fiber four-wave mixing with a polarization diversity technique", *IEEE photonics technology letters*, vol. 5, no. 8, pp. 947–949, 1993.

[237] K. Mochizuki, "Degree of polarization in jointed fibers: The lyot depolarizer", *Applied optics*, vol. 23, no. 19, pp. 3284–3288, 1984.

[238] V. Mazurczyk and J. Zyskind, "Polarization dependent gain in erbium doped-fiber amplifiers", *IEEE photonics technology letters*, vol. 6, no. 5, pp. 616–618, 1994.

[239] A. Shaham and H. Eisenberg, "Realizing controllable depolarization in photonic quantum-information channels", *Physical Review A*, vol. 83, no. 2, p. 022 303, 2011.

[240] Á. Rivas and A. Luis, "Su (2)-invariant depolarization of quantum states of light", *Physical Review A*, vol. 88, no. 5, p. 052 120, 2013.

[241] E. Waluschka, M. Wilson, M. Quijada, B. McAndrew, and L. Ding, "Orca's depolarizer", in *Earth Observing Systems XVI*, SPIE, vol. 8153, 2011, pp. 310–320.

[242] G. Ropars, G. Gorre, A. Le Floch, J. Enoch, and V. Lakshminarayanan, "A depolarizer as a possible precise sunstone for viking navigation by polarized skylight", *Proceedings of the Royal Society A: Mathematical, physical and engineering sciences*, vol. 468, no. 2139, pp. 671–684, 2012.

[243] A. D. Kersey, A. Dandridge, and M. Marrone, "Single-mode fiber pseudo-depolarizer", in *Fiber Optic and Laser Sensors V*, SPIE, vol. 838, 1988, pp. 360–364.

[244] W. Burns, "Degree of polarization in the lyot depolarizer", *Journal of Lightwave Technology*, vol. 1, no. 3, pp. 475–479, 1983.

[245] P.-Y. Chien and C.-L. Pan, "Fiber-optic gyroscopes based on polarization scrambling", *Optics letters*, vol. 16, no. 3, pp. 189–190, 1991.

Bibliography

[246] A. Cornu, "Détermination des trois paramètres optiques principaux d'un cristal, en grandeur et en direction, par le réfractomètre", *J. Phys. Theor. Appl.*, vol. 1, no. 1, pp. 136–147, 1902.

[247] F. Kroh, M. Rosskopf, and W. Elsässer, "Utilizing a cornu depolarizer in the generation of spatially unpolarized light", *Applied Optics*, vol. 60, no. 16, pp. 4892–4900, 2021.

[248] J. H. Ge, Z. Chen, Y. F. Chen, *et al.*, "Optimized design of parameters for wedge-crystal depolarizer", *Applied Mechanics and Materials*, vol. 110, pp. 3351–3357, 2012.

[249] Y. Jin and W. Shen, "Design of double wedge depolarizer for grating imaging spectrometer", in *Selected Papers of the Chinese Society for Optical Engineering Conferences held October and November 2016*, SPIE, vol. 10255, 2017, pp. 555–564.

[250] K. Bohm, K. Petermann, and E. Weidel, "Performance of lyot depolarizers with birefringent single-mode fibers", *Journal of Lightwave Technology*, vol. 1, no. 1, pp. 71–74, 1983.

[251] U. S. Mutugala, I. P. Giles, M. Ding, D. J. Richardson, and R. Slavík, "All-fiber passive alignment-free depolarizers capable of depolarizing narrow linewidth signals", *Journal of Lightwave Technology*, vol. 37, no. 3, pp. 704–714, 2018.

[252] K. Takada, K. Okamoto, and J. Noda, "New fiber-optic depolarizer", *Journal of lightwave technology*, vol. 4, no. 2, pp. 213–219, 1986.

[253] P. Shen, J. C. Palais, and C. Lin, "Fiber recirculating delay-line tunable depolarizer", *Applied optics*, vol. 37, no. 3, pp. 443–448, 1998.

[254] P. Shen and J. C. Palais, "Passive single-mode fiber depolarizer", *Applied optics*, vol. 38, no. 9, pp. 1686–1691, 1999.

[255] M. Martinelli and J. C. Palais, "Dual fiber-ring depolarizer", *Journal of lightwave technology*, vol. 19, no. 6, p. 899, 2001.

[256] W. Burns, R. Moeller, C. Bulmer, and A. Greenblatt, "Depolarized source for fiber-optic applications", *Optics letters*, vol. 16, no. 6, pp. 381–383, 1991.

[257] K. Takada, A. Himeno, K. Kato, and M. Okuno, "Development of fiber-optic depolarizer and its application to measurement systems for polarization-insensitive operation of silica-waveguide matrix switches", *Journal of Lightwave Technology*, vol. 12, no. 9, pp. 1640–1647, 1994.

[258] S. Yamashita and K. Hotate, "Polarization-independent depolarizers for highly coherent light using faraday rotator mirrors", *Journal of lightwave technology*, vol. 15, no. 5, pp. 900–905, 1997.

[259] H. Kim, C.-H. Lee, and H. Lee, "Suppression of the polarization hole burning in the edfa using an unpolarized source", in *Conference on Lasers and Electro-Optics/Pacific Rim*, Optica Publishing Group, 1995, TuI3.

[260] T. Yang, C. Shu, and C. Lin, "Depolarization technique for wavelength conversion using four-wave mixing in a dispersion-flattened photonic crystal fiber", *Optics Express*, vol. 13, no. 14, pp. 5409–5415, 2005.

[261] W. Astar, C.-C. Wei, Y.-J. Chen, J. Chen, and G. Carter, "Polarization-insensitive, 40 gb/s wavelength and rz-ook-to-rz-bpsk modulation format conversion by xpm in a highly nonlinear pcf", *Optics Express*, vol. 16, no. 16, pp. 12 039–12 049, 2008.

[262] T. Mahmood, W. Astar, B. M. Cannon, *et al.*, "Polarization-insensitive wavelength conversion by fwm of 100-ghz-spaced dwdm 4 × 10 gb/s rz-bpsk signals in a birefringent nonlinear algaas waveguide", *IEEE Journal of Quantum Electronics*, vol. 50, no. 2, pp. 74–84, 2013.

[263] R. Salem, A. S. Lenihan, G. M. Carter, and T. E. Murphy, "Techniques for polarization-independent cross-phase modulation in nonlinear birefringent fibers", *IEEE Journal of Selected Topics in Quantum Electronics*, vol. 14, no. 3, pp. 540–550, 2008.

[264] P. Ma, D.-Y. Choi, Y. Yu, *et al.*, "Low-loss chalcogenide waveguides for chemical sensing in the mid-infrared", *Optics express*, vol. 21, no. 24, pp. 29 927–29 937, 2013.

[265] P. Ma, D.-Y. Choi, Y. Yu, *et al.*, "High q factor chalcogenide ring resonators for cavity-enhanced mir spectroscopic sensing", *Optics express*, vol. 23, no. 15, pp. 19 969–19 979, 2015.

[266] D.-W. Sun, *Infrared spectroscopy for food quality analysis and control*. Academic press, 2009.

[267] G. Edwards, R. Logan, M. Copeland, *et al.*, "Tissue ablation by a free-electron laser tuned to the amide ii band", *Nature*, vol. 371, no. 6496, pp. 416–419, 1994.

[268] S. Xing, "Development of coherent mid-infrared source using chalcogenide photonic crystal fibers", EPFL, Tech. Rep., 2019.

[269] S. D. Le, D. M. Nguyen, M. Thual, *et al.*, "Efficient four-wave mixing in an ultra-highly nonlinear suspended-core chalcogenide as 38 se 62 fiber", *Optics Express*, vol. 19, no. 26, B653–B660, 2011.

[270] W. Kim, V. Nguyen, L. Shaw, *et al.*, "Recent progress in chalcogenide fiber technology at nrl", *Journal of Non-Crystalline Solids*, vol. 431, pp. 8–15, 2016.

[271] C. R. Petersen, U. Møller, I. Kubat, *et al.*, "Mid-infrared supercontinuum covering the 1.4–13.3 μm molecular fingerprint region using ultra-high na chalcogenide step-index fibre", *Nature Photonics*, vol. 8, no. 11, pp. 830–834, 2014.

[272] T. Cheng, K. Nagasaka, T. H. Tuan, *et al.*, "Mid-infrared supercontinuum generation spanning 2.0 to 15.1 μm in a chalcogenide step-index fiber", *Optics letters*, vol. 41, no. 9, pp. 2117–2120, 2016.

[273] Z. Zhao, X. Wang, S. Dai, *et al.*, "1.5–14 μm midinfrared supercontinuum generation in a low-loss te-based chalcogenide step-index fiber", *Optics letters*, vol. 41, no. 22, pp. 5222–5225, 2016.

[274] S. Singh, S. Varshney, and P. Datta, "Optical parametric amplification in chalcogenide step index fiber over infrared region", in *International Conference on Fibre Optics and Photonics*, Optica Publishing Group, 2012, WPo–12.

[275] S. Singh and S. Varshney, "Tunable optical parametric amplification characteristics of liquid-filled chalcogenide photonic crystal fibers", *Optics Letters*, vol. 38, no. 19, pp. 3846–3849, 2013.

[276] D. D. Hudson, S. A. Dekker, E. C. Mägi, *et al.*, "Octave spanning supercontinuum in an as 2 s 3 taper using ultralow pump pulse energy", *Optics letters*, vol. 36, no. 7, pp. 1122–1124, 2011.

[277] S. Xing, S. Kharitonov, J. Hu, and C.-S. Brès, "Linearly chirped mid-infrared supercontinuum in all-normal-dispersion chalcogenide photonic crystal fibers", *Optics express*, vol. 26, no. 15, pp. 19 627–19 636, 2018.

[278] C. R. Petersen, R. D. Engelsholm, C. Markos, *et al.*, "Increased mid-infrared supercontinuum bandwidth and average power by tapering large-mode-area chalcogenide photonic crystal fibers", *Optics express*, vol. 25, no. 13, pp. 15 336–15 348, 2017.

[279] N. Singh, D. Vermulen, A. Ruocco, *et al.*, "Supercontinuum generation in varying dispersion and birefringent silicon waveguide", *Optics express*, vol. 27, no. 22, pp. 31 698–31 712, 2019.

[280] S. Kharitonov, S. Xing, and C.-S. Brès, "Broadband dispersion characterization of chalcogenide tapered photonic crystal fiber", in *Advanced Solid State Lasers*, Optica Publishing Group, 2017, JM5A–10.

[281] D. Grassani, E. Tagkoudi, H. Guo, *et al.*, "Mid infrared gas spectroscopy using efficient fiber laser driven photonic chip-based supercontinuum", *Nature communications*, vol. 10, no. 1, p. 1553, 2019.

[282] E. Tagkoudi, D. Grassani, F. Yang, C. Herkommer, T. Kippenberg, and C.-S. Brès, "Parallel gas spectroscopy using mid-infrared supercontinuum from a single si 3 n 4 waveguide", *Optics Letters*, vol. 45, no. 8, pp. 2195–2198, 2020.

[283] A. Ayan, S. Kharitonov, and C.-S. Brès, "Design and analysis of depolarized four-wave mixing in dhalcogenide photonic crystal fibers", in *The European Conference on Lasers and Electro-Optics*, Optica Publishing Group, 2021, cd_7_6.

[284] M. A. Foster, A. C. Turner, R. Salem, M. Lipson, and A. L. Gaeta, "Broad-band continuous-wave parametric wavelength conversion in silicon nanowaveguides", *Optics Express*, vol. 15, no. 20, pp. 12 949–12 958, 2007.

[285] J. Cardenas, S. Miller, Y. Okawachi, *et al.*, "Parametric frequency conversion in silicon carbide waveguides", in *2015 Conference on Lasers and Electro-Optics (CLEO)*, IEEE, 2015, pp. 1–3.

[286] C.-L. Wu, Y.-J. Chiu, C.-L. Chen, Y.-Y. Lin, A.-K. Chu, and C.-K. Lee, "Four-wave-mixing in the loss low submicrometer ta 2 o 5 channel waveguide", *Optics letters*, vol. 40, no. 19, pp. 4528–4531, 2015.

[287] A. Ayan, F. Mazeas, J. Liu, T. J. Kippenberg, and C.-S. Brès, "Polarization selective ultra-broadband wavelength conversion in silicon nitride waveguides", *Optics Express*, vol. 30, no. 3, pp. 4342–4350, 2022.

[288] A. Ayan, J. Liu, T. Kippenberg, and C.-S. Brès, "Continuous-wave four-wave mixing efficiency-bandwidth tradeoff study in meter-long silicon nitride waveguides", in *2022 Conference on Lasers and Electro-Optics (CLEO)*, IEEE, 2022, pp. 1–2.

[289] A. Ayan, J. Liu, T. Kippenberg, and C.-S. Brès, "Towards efficient broadband parametric conversion in ultra-long si3n4 waveguides", *Optics Express*, 2023. DOI: 10.1364/oe.502648.

[290] Y. Liu, Z. Qiu, X. Ji, *et al.*, "A photonic integrated circuit–based erbium-doped amplifier", *Science*, vol. 376, no. 6599, pp. 1309–1313, 2022.

[291] H. El Dirani, L. Youssef, C. Petit-Etienne, *et al.*, "Ultralow-loss tightly confining si 3 n 4 waveguides and high-q microresonators", *Optics express*, vol. 27, no. 21, pp. 30 726–30 740, 2019.

[292] H. Wu, C. Li, L. Song, H.-K. Tsang, J. E. Bowers, and D. Dai, "Ultra-sharp multimode waveguide bends with subwavelength gratings", *Laser & Photonics Reviews*, vol. 13, no. 2, p. 1 800 119, 2019.

[293] X. Ji, J. Liu, J. He, *et al.*, "Compact, spatial-mode-interaction-free, ultralow-loss, nonlinear photonic integrated circuits", *Communications Physics*, vol. 5, no. 1, p. 84, 2022.

[294] T. Chen, H. Lee, J. Li, and K. J. Vahala, "A general design algorithm for low optical loss adiabatic connections in waveguides", *Optics express*, vol. 20, no. 20, pp. 22 819–22 829, 2012.

[295] O. Yakar, C. Lafforgue, A. Ayan, *et al.*, "Mid-ir all-optical poling in silicon nitride waveguides", in *The European Conference on Lasers and Electro-Optics*, Optica Publishing Group, 2023, cd_6_4.

[296] K. B. Beć, J. Grabska, Y. Ozaki, M. A. Czarnecki, and C. W. Huck, "Simulated nir spectra as sensitive markers of the structure and interactions in nucleobases", *Scientific reports*, vol. 9, no. 1, p. 17 398, 2019.

[297] K. B. Beć, J. Grabska, and C. W. Huck, "In silico nir spectroscopy–a review. molecular fingerprint, interpretation of calibration models, understanding of matrix effects and instrumental difference", *Spectrochimica Acta Part A: Molecular and Biomolecular Spectroscopy*, vol. 279, p. 121 438, 2022.

[298] K. B. Beć, J. Grabska, C. W. Huck, S. Mazurek, and M. A. Czarnecki, "Anharmonicity and spectra–structure correlations in mir and nir spectra of crystalline menadione (vitamin k3)", *Molecules*, vol. 26, no. 22, p. 6779, 2021.

[299] J. Grabska, K. B. Beć, Y. Ozaki, and C. W. Huck, "Anharmonic dft study of near-infrared spectra of caffeine: Vibrational analysis of the second overtones and ternary combinations", *Molecules*, vol. 26, no. 17, p. 5212, 2021.

[300] C. Sun, B. Li, M. Zhao, *et al.*, "J-aggregates of cyanine dye for nir-ii in vivo dynamic vascular imaging beyond 1500 nm", *Journal of the American Chemical Society*, vol. 141, no. 49, pp. 19 221–19 225, 2019.

Bibliography

[301] B. Li, M. Zhao, and F. Zhang, "Rational design of near-infrared-ii organic molecular dyes for bioimaging and biosensing", *ACS Materials Letters*, vol. 2, no. 8, pp. 905–917, 2020.

[302] J. Liu and T. Kobayashi, "Generation and amplification of tunable multicolored femtosecond laser pulses by using cascaded four-wave mixing in transparent bulk media", *Sensors*, vol. 10, no. 5, pp. 4296–4341, 2010.

[303] W. Liu, L. Zhu, L. Wang, and C. Fang, "Cascaded four-wave mixing for broadband tunable laser sideband generation", *Optics Letters*, vol. 38, no. 11, pp. 1772–1774, 2013.

[304] H. Crespo, J. Mendonça, and A. Dos Santos, "Cascaded highly nondegenerate four-wave-mixing phenomenon in transparent isotropic condensed media", *Optics Letters*, vol. 25, no. 11, pp. 829–831, 2000.

Optical Engineer
Arman Ayan

Doctoral School of Photonics, EPFL
Lausanne, Switzerland
arman.ayan@epfl.ch

EDUCATION

Ecole Polytechnique Federal de Lausanne (EPFL)   Lausanne, Switzerland
Ph.D. Candidate in *Photonics*   July 2019–Present
Area: Nonlinear Integrated and Fiber Optics
Advisor: Prof. Dr. Camille-Sophie Brès

Middle East Techincal University (METU)   Ankara, Turkey
M.S. in *Electrical-Electronics Eng.*   September 2015–September 2018
Area: Integrated Photonics and Fabrication
Advisor: Asst. Prof. Dr. Selçuk Yerci
Thesis: Strain Induction on Ge Nanobeams by Electrostatic Actuation
CGPA: 4.00/4.00

Middle East Technical University (METU)   Ankara, Turkey
B.S. in *Physics* (Double Major)   September 2012–June 2016
CGPA: 3.71/4.00

Middle East Technical University (METU)   Ankara, Turkey
B.S. in *Electrical and Electronics Eng.*   September 2010– June 2015
CGPA: 3.81/4.00

EMPLOYMENT HISTORY

Research and Teaching Assistant   July 2019–Present
Doctoral School of Photonics, EPFL   Lausanne, Switzerland

Research and Teaching Assistant   November 2015–April 2019
Department of Electrical-Electronics Eng., METU   Ankara, Turkey

Meteksan Defence Industries Inc.   Summer Internship June–July 2014
DC/DC converters with PCB design   Ankara, Turkey

Kasırga Electronics   Summer Internship June–July 2013
Digital Circuit Design with Verilog HDL   Ankara, Turkey

RESEARCH EXPERIENCE

All-fiber and free-space four-wave-mixing rxperiments in Si_3N_4 eaveguides
Depolarized four-wave-mixing in chalcogenide fibers
Finite-element-method analysis of electromechanical strain on Ge
Fabrication of c-Ge-on-Si devices

FABRICATION EXPERIENCE

Machine Supervisor
Sputtering Deposition System   *Rapid-Thermal-Annealing*

Licensed User
E-beam Deposition System   *Wet Bench*   *Photolithography*
Oxygen Plasma System   *Spectral Ellipsometry*   *Raman Spectroscopy*

SELECTED PUBLICATIONS	**Towards efficient broadband parametric conversion in ultra-long** Si_3N_4 **waveguides** 2023
	Ayan, A., Liu, J., Kippenberg, T. J., Bres, C. S.
	Optics Express, DOI: 10.1364/OE.502648
	Polarization Selective Ultra-Broadband Wavelength Conversion in Silicon Nitride Waveguides 2022
	Ayan, A., Mazeas, F., Liu, J., Kippenberg, T. J., Bres, C. S.
	Optics Express DOI: 10.1364/OE.446357
	Strain Engineering of Ge Nanobeams by Electrostatic Actuation 2019
	Ayan, A., Turkay, D., Unlu, B., Naghinazhadahmadi, P., Oliaei, S. N. B., Boztug, C., Yerci, S.
	Scientific reports DOI: 10.1038/s41598-019-41097-1

CONFERENCES	**Conference of Lasers and Electro-Optics 2022** May 2022
	Oral Presentation
	Continuous-Wave Four-Wave Mixing Efficiency-Bandwidth Tradeoff Study in Meter-Long Silicon Nitride Waveguides
	European Conference of Optical Communications 2021 September 2021
	Oral Presentation
	Polarization selective ultra-broadband wavelength conversion in silicon nitride waveguide
	Conference of Lasers and Electro-Optics Europe 2021 June 2021
	Oral Presentation
	Design and Analysis of Depolarized Four-Wave Mixing in Chalcogenide Photonic Crystal Fibers
	European Material Research Society 2018 Spring Meeting June 2018
	Oral Presentation
	Design of the Strained-Ge Microbidges for the Development of Ge Laser on Si
	13th NANOTR Nanoscience and Nanotech Conference October 2017
	Poster Presentation
	Fabrication of Germanium-on-Silicon by Rapid-Melting-Growth

HONORS & AWARDS	**Granted Tübitak Domestic Graduate Scholarship** 2017; Ankara, Turkey
	2015-2016 METU Graduate Courses Performance Award June 2017
	For achieving the highest CGPA in M.S. Program
	in the department of Electrical-Electronics Engineering

COMPUTER SKILLS	*Software:* COMSOL, Cadence, MATLAB, LTSpice, Origin Pro
LANGUAGES	Turkish (Native), English (Fluent), French (Advanced), Italian (Intermediate)

NON-ACADEMIC INTERESTS	Member of METU Cinema Society 2016-2017
	Bass Guitar Player
	Photonics Doctoral School Student Representative October 2022 - Present

2